

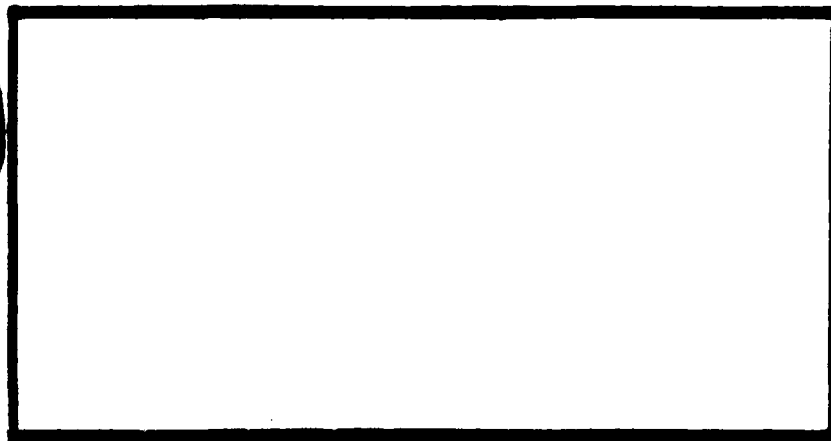
AD-A243 902



1



DTIC
ELECTE
JAN 03 1992
S D



92-00173



This document has been approved
for public release and sale; its
distribution is unlimited.

DEPARTMENT OF THE AIR FORCE
AIR UNIVERSITY
AIR FORCE INSTITUTE OF TECHNOLOGY

Wright-Patterson Air Force Base, Ohio

92 1 2 139

AFIT/GAE/ENY/91D-1

B

DTIC
ELECTE
JAN 03 1992
S D

EXPERIMENTAL INVESTIGATION OF TRAILING EDGE
CRENULATION EFFECTS ON LOSSES IN A
COMPRESSOR CASCADE

THESIS

STEVEN J. DECOOK

AFIT/GAE/ENY/91D-1

ADDITIONAL	
DTIC GRAVITY	<i>J</i>
DATE	<i>1</i>
ORGANIZATION	
DESCRIPTION	
By	
Signature	
Approved	
Out	
<i>A-1</i>	

Approved for public release: distribution unlimited.

AFIT/GAE/ENY/91D-1

**EXPERIMENTAL INVESTIGATION OF TRAILING EDGE CRENUATION EFFECTS ON
LOSSES IN A COMPRESSOR CASCADE**

THESIS

**Presented to the Faculty of the School of Engineering
of the Air Force Institute of Technology
Air University
In Partial Fulfillment of the
Requirements for the Degree of
Master of Science in Aeronautical Engineering**

STEVEN J. DECOOK

December 1991

Approved for public release: distribution unlimited.

Acknowledgments

After many long months this project is coming to an end. It would not have been possible without the help and expertise of many individuals. I would like to thank my advisor, Dr. Paul King, whose guidance helped me to navigate what was for me the uncharted waters of experimental aerodynamics research. I would also like to thank the other members on my thesis committee, Dr. William Elrod and Lt. Col. Gerald Hasen, for their contribution to this thesis. Dr. Elrod's door was always open for impromptu consultation, and I visited him frequently to draw upon his years of experience with the AFIT Cascade Test Facility.

Mr. Nick Yardich, the laboratory supervisor, and his staff, Mr. Jay Anderson, Mr. Andy Pitts, Mr. Dan Rioux, and Mr. Mark Derriso have each contributed in a variety of ways, from helping to assemble data acquisition hardware and trouble shooting noisy signals to upgrading the computer facilities and maintaining older equipment. My thanks to you all. Mr. John Brohas, Mr. Dave Driscoll, and several other individuals from the AFIT model job also made significant contributions to this project, modifying cascade blades and the test section, and building some special equipment for hotwire calibration and repair. My thanks to you as well.

I would also like to thank Mr. Bob McCall, Lt. Jim Rothenflue, Capt. Dino Ishikura, Capt. Neal Mosbarger, Maj. Randy Smith, Ms. Mary McMillian, and other friends at AFIT whose interest and encouragement helped keep my spirits up during this research. Your friendship warms my heart.

Finally, I thank God for His faithfulness. Faith in God brings a sense of peace, stability, and purpose to my life, and I value that above all else. Praise be to God and the Lord Jesus Christ.

Steven J. Decook

Table of Contents

	Page
Acknowledgments	ii
List of Figures	v
List of Tables	vii
List of Symbols	viii
Abstract	xii
I. Introduction	1
II. Theory	4
Cascade Geometry	4
Cascade Performance and Wake Dissipation Measurements	5
Cascade Flow Condition	9
III. Experimental Apparatus and Procedure	12
Airflow Source	12
Test Section and Blades	12
Instrumentation	14
Thermocouples and Pressure Transducers	14
Total Pressure Rake and Stepper Motors	14
Hot Wire Anemometry	15
Digitizers	16
Computer	16
Assumptions and Procedure	17
Turbulence Injection Effects on Total Pressure	18
Periodicity and Blade Surface Pressures	20
Downstream Velocity and Pressure Losses	20
Turning Angle and Turbulence Intensity	21
IV. Discussion of Results	22
Periodicity	22
Secondary Flow Effects	24
Flow Visualization	24
Axial Velocity Density Ratio	25
Blade Surface Pressures	27
Static Pressure Rise	29
Turning Angle	34
Total Pressure Loss Contours	38
Total Pressure Losses	40
Wake Velocity Deficit	42
Outlet Velocity Variance	43
V. Conclusions and Recommendations	46
Conclusions	46
Recommendations	47

References	48
Appendix A. Airfoil Geometry and Performance Estimates.	75
Section Data	75
Blade Angles	78
Momentum Analysis of Flow Through a Cascade	78
Estimates of Turning Angle and Pressure Loss	81
Appendix B. Hotwire Calibration	86
Appendix C. Hotwire Data Reduction	93
Appendix D. Turbulence Calculations	96
Calculation of Velocity Fluctuation Root Mean Squares	97
Scaling and Transformation of Coordinates	99
Calculation of Turbulence	100
Vita	102

List of Figures

Figure	Page
1. Development of blade wakes, Lieblein (1:201)	50
2. Crenulated compressor blade	50
3. Cascade geometry, Cohen (4:188)	51
4. Secondary flow pattern in a cascade	51
5. Cascade Test Facility	52
6. Test section	52
7. Crenulation dimensions	53
8. Instrumentation setup	53
9. Total pressure rake	54
10. Hot wire sensor with "X" configuration	54
11. Turbulence intensity downstream of injection	55
12. Velocity about 5 in. downstream of turbulence injection	55
13. Pitchwise distribution of static pressures at cascade inlet, "Suction off, Turb on" . . .	56
14. Pitchwise distribution of velocity at cascade outlet, "Suction on"	56
15. Sidewall boundary layer flow patterns	57
16. Suction surface boundary layer flow patterns	58
17. Axial velocity density ratio: flow comparison	59
18. Axial velocity density ratio: blade comparison	60
19. Blade surface pressures: flow comparison	61
20. Blade surface pressures: blade comparison	62
21. Static pressure rise across cascade	63
22. Flow turning angle	63
23. Pressure loss coefficient contours with unmodified blades	64
24. Pressure loss coefficient contours with large crenulations	65
25. Pressure loss coefficient contours with small crenulations	66

26. Total pressure loss coefficient: flow comparison	67
27. Total pressure loss coefficient: blade comparison	68
28. Wake velocity deficit: flow comparison	69
29. Wake velocity deficit: blade comparison	70
30. Mass averaged outlet velocity variance: flow comparison	71
31. Mass averaged outlet velocity variance: blade comparison	72
32. Outlet velocity variance: flow comparison	73
33. Outlet velocity variance: blade comparison	74
34. Control surface around blade in cascade, Horlock (5:33)	79
35. X-wire sensor geometry	93

List of Tables

Table	Page
1. Tailboard Angles, degrees, in "Suction on, Turb off" flow	23
2. Cascade Pressure Data	30
3. Static Pressure Rise Comparisons	30
4. Measured Turning Angles	35
5. Calculated Turning Angles	35
6. Decrease in Total Pressure Loss with Crenulated Blades	42
7. Decrease in Wake Velocity Deficit with Crenulated Blades	43
8. Decrease in Outlet Velocity Variance with Crenulated Blades	44

List of Symbols

Symbol

2D	two-dimensional
3D	three-dimensional
AFIT	Air Force Institute of Technology
AOA	angle of attack, degrees
AVR	axial velocity ratio
AVDR	axial velocity density ratio
CTA	constant temperature anemometer
HP	Hewlett Packard
LE	leading edge
SSE	sum squared error
TE	trailing edge
TSI	ThermoSystems, Inc.
WVD	wake velocity deficit
a	distance from leading edge to point of maximum camber (in)
A	representative exit flow quantity, hot wire sensor area (in ²), hot wire calibration coefficient
$\overline{A_M}$	representative mass averaged exit flow quantity
b	temperature loading factor exponent, x-wire sensor bisector angle (degrees)
B	hot wire calibration coefficient
c	chord (in)
c_p	constant pressure specific heat (0.240 Btu/(lbm·°R))
C	hot wire calibration coefficient
C_D	coefficient of drag
C_p	cascade static pressure coefficient, blade surface pressure coefficient
d_s	hotwire sensor diameter (in)
D	drag force on blade (lb), diffusion factor
h_f	fluid convective heat transfer coefficient
H_2	form factor = displacement thickness/momentum thickness
i	incidence angle (degrees)
i^*	nominal incidence angle (degrees)
i_r	reference incidence angle (degrees)

i_0	zero camber incidence angle (degrees)
$(i_0)_{10}$	zero camber incidence angle for 10% thick, 65 series airfoil (degrees)
I_s	current through hot wire sensor (amps)
k	cooling ratio of hotwire sensor
k_1	cooling ratio of x-wire sensor #1
k_2	cooling ratio of x-wire sensor #2
k_0	reference fluid thermal conductivity
k_f	fluid thermal conductivity
$(K_\theta)_{sh}$	shape factor for incidence angle
$(K_\theta)_t$	thickness factor for incidence angle
$(K_\delta)_{sh}$	shape factor for deviation angle
$(K_\delta)_t$	thickness factor for deviation angle
l	chord (in)
l_s	hotwire sensor length (in)
L	lift force on blade (lb)
m	change in reference deviation angle with camber angle
M	Mach number
n	change in reference incidence angle with camber angle
Nu	Nusselt number
P	static pressure (lb/in ²)
P_1	inlet static pressure (lb/in ²)
P_2	outlet static pressure (lb/in ²)
P_0	total pressure (lb/in ²)
P_{01}	inlet total pressure (lb/in ²)
P_{02}	outlet total pressure (lb/in ²)
P_s	blade surface pressure (lb/in ²)
Q_1	inlet dynamic pressure (lb/in ²)
Q_2	outlet dynamic pressure (lb/in ²)
r_c	recovery factor
R	gas constant (53.36 ft·lb _f /(°R·lb _m for air))
R_c	cable resistance (ohms)
R_{pi}	probe internal resistance (ohms)
R_{ps}	probe support resistance (ohms)
R_s	hot wire sensor resistance (ohms)
R_u	bridge upper arm resistance (ohms)

Re	Reynolds number
s	blade spacing (in)
S_1	constant used in calculation of viscosity
T_{AW}	adiabatic wall temperature (degrees)
T_f	fluid static temperature (degrees)
T_r	Eckert reference temperature (degrees)
T_s	hotwire sensor temperature (degrees)
Tu	turbulence intensity (%)
Tu_x	axial turbulence intensity (%)
Tu_y	tangential turbulence intensity (%)
T_1	inlet static temperature (degrees)
T_{01}	inlet total temperature (degrees)
V_1	inlet velocity (ft/s)
V_2	outlet velocity (ft/s)
\bar{V}_2	average outlet velocity (ft/s)
V_{ϕ}	effective velocity across hotwire sensor (ft/s)
$V_{1\phi}$	effective velocity across sensor #1 (ft/s)
$V_{2\phi}$	effective velocity across sensor #2 (ft/s)
V_{FS}	outlet freestream velocity (ft/s)
V_m	mean velocity through passage (ft/s)
V_P	velocity perpendicular to hotwire sensor (ft/s)
V_s	voltage across hot wire sensor (volts)
\bar{v}_x	root mean square of fluctuating axial velocity (ft/s)
V_x	axial velocity (ft/s)
V_{x1}	inlet axial velocity (ft/s)
V_{x2}	outlet axial velocity (ft/s)
\bar{V}_{x2}	mass averaged outlet axial velocity (ft/s)
V_{y1}	inlet tangential velocity (ft/s)
V_{y2}	outlet tangential velocity (ft/s)
\bar{v}_y	root mean square of fluctuating tangential velocity (ft/s)
V_θ	tangential velocity (ft/s)
X	axial force on blades (lb)
Y	tangential force on blades (lb)
z	span dimension encompassing measurements (in)

Greek symbols

α	angle between hotwire sensor and velocity vector (degrees)
α_1	air inlet angle, angle between sensor #1 and velocity (degrees)
α_2	air outlet angle, angle between sensor #2 and velocity (degrees)
α'_1	blade inlet angle (degrees)
α'_2	blade outlet angle (degrees)
α_m	mean angle through the passage (degrees)
α_1^*	nominal air inlet angle (degrees)
α_2^*	nominal air outlet angle (degrees)
β	angle between x-wire bisector and the velocity vector (degrees)
γ	ratio of specific heats
δ	deviation angle (degrees)
δ^*	nominal deviation angle (degrees)
δ°	deviation angle (degrees)
δ_r°	reference deviation angle (degrees)
δ_0°	zero camber deviation angle (degrees)
$(\delta_0^\circ)_{10}$	zero camber deviation angle for 10% thick, 65 series airfoil (degrees)
ϵ	deflection angle (degrees)
ϵ^*	nominal deflection angle (degrees)
ζ	stagger angle (degrees)
θ	camber angle in Howell's correlation (degrees)
θ^*	wake momentum thickness (in)
μ	viscosity ($\text{lb}_m/(\text{ft s})$)
μ_0	reference viscosity ($1.173 \cdot 10^{-5} \text{ lb}_m/(\text{ft s})$ at $T_o = 492^\circ \text{R}$)
ρ	density (lb_m/ft^3)
ρ_1	inlet density (lb_m/ft^3)
ρ_2	outlet density (lb_m/ft^3)
σ^2	variance
$\bar{\sigma}^2$	mass averaged (weighted) variance
ϕ	constant used in Howell's correlation
ψ	constant used in Howell's correlation
φ	camber angle in Lieblein's correlation (degrees)
$\bar{\omega}$	total pressure loss coefficient
$\bar{\omega}_1$	total pressure loss coefficient from inlet dynamic pressure

Abstract

The effects of blade trailing edge crenulations on wake losses in a compressor cascade were investigated at the Air Force Institute of Technology. The cascade used NACA 64-A905 blades with a turning angle of about 30 degrees to model last row stators of an axial flow compressor. Three blade configurations were used: unmodified blades, blades with large crenulations, and blades with small crenulations. Wake losses and mixing were evaluated in four flow conditions, generated by combinations of increased freestream turbulence and sidewall boundary layer removal. Injection of air perpendicular to the inlet flow increased freestream turbulence from about 0.15% to about 4%. The sidewall boundary layers could be removed by suction through sidewall slots immediately ahead of the cascade. A total pressure rake measured the difference between upstream and downstream total pressure, yielding pressure loss and velocity data, and hot wire anemometry was used downstream from the cascade to measure flow angle, relative turbulence, and velocity. For each test condition, the crenulated blades decreased total pressure loss, the wake velocity deficit, and wake velocity variance by about 10% to 20%, while slightly decreasing turning angle and increasing the turbulence level. The size of the crenulations had a small effect on these parameters.

EXPERIMENTAL INVESTIGATION OF TRAILING EDGE CRENUATION EFFECTS ON LOSSES IN A COMPRESSOR CASCADE

I. Introduction

A cascade is composed of a set of airfoils and is usually used to change the direction and pressure of a fluid flow. Cascades may be used to model flow through blade rows of axial flow compressors and axial flow turbines, two components of gas turbine engines. Consequently, the development of gas turbine engines has given great impetus to cascade testing. Cascade geometry, blade shapes, and their correlations to performance have been solidly established, yet the potential for higher performance and greater efficiency continues to stimulate research. Cascade parameters are often varied to optimize particular aspects of performance for specific applications. This is one such effort.

Blade wakes, illustrated in Figure 1, are characteristic features of cascade outlet flow. These wakes are regions of low momentum air that form at the trailing edge of each airfoil where the boundary layers from the suction surface and pressure surface come together. Viscous forces cause the wakes to mix into the surrounding flow until the outlet flow velocity becomes uniform at some distance downstream from the cascade. In axial flow compressors, the non-uniform velocities and pressures caused by blade wakes degrade the performance of downstream blade rows. In gas turbines, compressor outlet flow enters the combustor which is also sensitive to non-uniform flow. A duct of an appropriate length is used to ensure adequate flow uniformity at the combustor inlet. Minimizing the blade wakes would be beneficial to both compressors and gas turbines.

In 1982 Wennerstrom (2) suggested that crenulated trailing edges on airfoils would increase the rate of wake dissipation. The crenulations, shown in Figure 2, are small notches that

are intended to generate counterrotating vortices, driven by the pressure difference between the suction and pressure surfaces of the airfoil. These vortices would actively mix the wake into the freestream flow. At the time it was unclear to what extent crenulations would improve wake mixing, if they would degrade performance, and if they had an optimal geometry.

In 1989, Veasart, et. al. (3) found that in a subsonic compressor cascade ($M = 0.4$) with low freestream turbulence both large and small crenulations improved wake mixing, decreased total pressure loss, and slightly increased turning angle. These positive results warranted further investigation. In particular, the influence of higher free stream turbulence on the action of crenulated trailing edges needed to be quantified. It was possible that higher free stream turbulence would negate the improvements demonstrated by crenulated blades in low turbulence flow. There was also the possibility that the effects of the crenulations were due in part to interaction with secondary flows in the passage, especially the corner vortices which form where blade suction surfaces intersect the cascade sidewall. Finally, the influence of crenulations on static pressure rise through the cascade needed further clarification.

In this study, four flow conditions were used to examine the influence of freestream turbulence and corner vortices on the effects of trailing edge crenulations. For comparison to the low turbulence flow (about 0.15%), a moderate level of freestream turbulence (about 4%) was generated by air injection perpendicular to the inlet flow upstream from the cascade. Also, the secondary flows and corner vortices in the cascade are developed in the sidewall boundary layers, which could be reduced by suction through a sidewall slot upstream from the cascade. Two levels of secondary flow were obtained by either obstructing or applying suction to the slot. Combining the two levels of freestream turbulence and the two levels of corner vortex strength resulted in four flow conditions.

The cascade, airfoil, and crenulation geometry used in this study were the same as used by Veasart, et. al. (3). These and the parameters used to evaluate wake losses and mixing are discussed in Chapter II. The experimental apparatus and procedure are described in Chapter III. The results are presented in Chapter IV, followed by conclusions and recommendations in

Chapter V. Figures and graphs pertinent to the text follow the list of references. Appendix A contains information on the cascade, blade geometry, and performance estimates. Appendices B, C, and D contain the procedure for hotwire calibration, the reduction of hotwire data to the local velocity and direction, and the reduction of hotwire data to the local turbulence intensity, respectively.

II. Theory

Cascade Geometry

A linear cascade is composed of a set of airfoils spaced equally in a line called the blade row. It is usually used to change the direction and static pressure of a fluid flow. The airfoils may be called blades or vanes. Span, chord, pitch, and axial are terms used to describe orientation in cascades. Span refers to the width direction of a cascade. Chord refers to the line between the leading edge and the trailing edge of an airfoil cross section, but it may also refer to the direction of that line. Pitch refers to the direction of the blade row, and axial refers to the direction perpendicular to the blade row. Cascade geometry is illustrated in Figure 3.

Four parameters are needed to describe a linear cascade. The first is solidity, which is the ratio of blade chord to blade spacing. The second is the stagger angle, which specifies the blade setting in the cascade and is measured between the blade chord line and the axial direction. The third parameter is the shape of the blade cross section, and the fourth is the aspect ratio, the ratio of blade span to blade chord. The first three parameters are sufficient to describe a two dimensional cascade.

In addition to these parameters, a number of other angles may be defined in a cascade. The camber angle describes the curvature of the blade mean line and is measured between the tangents to the blade mean line at the leading and trailing edges. The blade inlet angle is measured between the tangent to the blade mean line at the leading edge and the axial direction, and the blade outlet angle is measured between the tangent to the blade mean line at the trailing edge and the axial direction. The air inlet and air outlet angles are measured between the direction of the inlet or outlet flow and the axial direction. The cascade turning angle (also called the deflection angle) is the change in flow direction caused by the cascade and is measured between the air inlet and air outlet angles. The angle of attack is measured between the blade chord line and the air inlet angle. It may be calculated by subtracting the stagger angle from the

air inlet angle. Using the notation in Figure 3, $AOA = \alpha_1 - \zeta$. The incidence angle is measured between the blade inlet and the air inlet angles, and it directly influences cascade performance and losses. For a given stagger angle, the blade angle of attack and the incidence angle differ by a constant, $AOA = (\alpha_1' - \zeta) + i$. Finally, the deviation angle is measured between the blade outlet angle and the air outlet angle. Empirical deviation angle data is often used to estimate the air outlet angle for a given cascade configuration.

Cascade Performance and Wake Dissipation Measurements

Cascade performance can be evaluated by the changes in flow direction and static pressure caused by the cascade. Assuming two dimensional (2D) and incompressible flow, the change in static pressure across the cascade may be related to the inlet and outlet flow angles by combining continuity with the Bernoulli equation. Using the definitions in Figure 3

$$V_1 \cos \alpha_1 = V_{x_1} = V_2 \cos \alpha_2 = V_{x_2} = V_x \quad (1)$$

$$P_2 - P_1 = \frac{1}{2} \rho (V_1^2 - V_2^2) + (P_{02} - P_{01}) \quad (2)$$

$$P_2 - P_1 = \frac{1}{2} \rho V_1^2 \left(1 - \frac{\cos^2 \alpha_1}{\cos^2 \alpha_2} \right) - (P_{01} - P_{02}) \quad (3)$$

$$(P_2 - P_1) / \left(\frac{1}{2} \rho V_1^2 \right) = C_p = \left(1 - \frac{\cos^2 \alpha_1}{\cos^2 \alpha_2} \right) - \bar{\omega}_1 \quad (4)$$

where C_p is the cascade static pressure coefficient, P_1 and P_2 are the inlet and outlet static pressures, P_{01} and P_{02} are the inlet and outlet total pressures, and $\bar{\omega}_1$ is the total pressure loss coefficient. Equation (4) must be regarded as an estimate if the flow through the cascade is compressible or is not two dimensional.

The inlet and outlet flow angles are also related to the static pressure on the blade surfaces. The blade surface pressures may be integrated to produce values for lift and drag.

Assuming two dimensional and incompressible flow, as above, continuity and the Bernoulli equation may be combined with the momentum equation to produce expressions for lift and drag. From the development in Appendix A, lift and drag are calculated by

$$L = \rho V_x^2 (\tan \alpha_1 - \tan \alpha_2) s \sec \alpha_m - (P_{01} - P_{02}) s \sin \alpha_m \quad (5)$$

$$D = (P_{01} - P_{02}) s \cos \alpha_m \quad (6)$$

where

$$\tan \alpha_m = \frac{1}{2}(\tan \alpha_1 + \tan \alpha_2) \quad (7)$$

An increase in lift should correspond to an increase in the cascade turning angle.

Another part of cascade performance is the loss in total (stagnation) pressure through the cascade. It is non-dimensionalized by the inlet dynamic pressure to form a total pressure loss coefficient:

$$\bar{\omega} = (P_{01} - P_{02}) / \left(\frac{1}{2} \rho_1 V_1^2 \right) \quad (8)$$

Empirical cascade data provide benchmark values of turning angle and total pressure loss for a variety of cascade configurations. Horlock (5:55-62) and Lieblein (1) present correlations of cascade data for circular arc airfoils and NACA 6-series airfoils respectively.

Data from the outlet flow are generally acquired in an area perpendicular to the flow direction at a given location downstream from the cascade. For the sake of comparison, it is convenient to summarize the data as a single point, perhaps by an average. However, the variations of velocity in the outlet flow, particularly within the blade wakes, are variations of mass flow. This suggests that averages of the data should be weighted by mass flow. A mass average is calculated by

$$\bar{A} = \frac{\int_{-s/2}^{s/2} \int_{-z}^z A \rho_2 V_{x_2} dz dy}{\int_{-s/2}^{s/2} \int_{-z}^z \rho_2 V_{x_2} dz dy} \quad (9)$$

where A is the quantity being mass averaged, dz is in the span direction, dy is in the pitch direction, and s is one blade spacing. Total pressure, velocity, velocity variance, turning angle, and turbulence are mass averaged when so indicated.

Wake dissipation in the outlet flow is evaluated by the velocity deficit and by the variance of velocities. The wake velocity deficit (WVD) is calculated by

$$WVD = \frac{(V_{FS} - \bar{V}_{x_2})}{V_{FS}} = 1 - \frac{\bar{V}_{x_2}}{V_{FS}} \quad (10)$$

where \bar{V}_{x_2} is the outlet mass averaged axial velocity and V_{FS} is the outlet freestream velocity. The latter is the velocity outside the wake, and it should be nearly uniform. Its calculation begins with a set of velocities from an area perpendicular to the outlet flow which includes one blade spacing in the pitch direction. The velocities are averaged in the span direction producing a single set of velocities in the pitch direction. It was assumed that velocities in the blade wake would be included in the lower 75% of this averaged set, and that the mean of the top 25% of the set would adequately represent the freestream velocity. If the top 25% of the set is not uniform then the calculation may misrepresent the freestream velocity. In that case the wake velocity deficit is not well defined.

The variance of outlet velocities in an area perpendicular to the outlet flow may also be used to evaluate the wake dissipation. Variance is the square of standard deviation, and it is sensitive to differences from the mean. In this study the variance of outlet velocity is non-dimensionalized by the mean outlet velocity and is defined by

$$\sigma^2 = \frac{1}{\bar{V}_2^2} \cdot \frac{\sum_{i=1}^n (V_{2,i} - \bar{V}_2)^2}{(n - 1)} \quad (11)$$

where n is the number of points sampled in the outlet flow at a given distance downstream.

A velocity ratio variance weighted by mass flow is also reported, as defined by

$$\bar{\sigma}^2 = \frac{1}{\bar{V}_2^2} \cdot \frac{\sum_{i=1}^n \rho_{2,i} V_{2,i} (V_{2,i} - \bar{V}_2)^2}{\bar{\rho}_2 \bar{V}_2 (n - 1)} \quad (12)$$

$$\bar{\sigma}^2 = \frac{1}{\bar{V}_2^2} \cdot \frac{\sum_{i=1}^n \rho_{2,i} V_{2,i} (V_{2,i} - \bar{V}_2)^2}{\left(\frac{\sum_{i=1}^n \rho_{2,i} V_{2,i}}{n - 1} \right) (n - 1)} \quad (13)$$

$$\bar{\sigma}^2 = \frac{1}{\bar{V}_2^2} \cdot \frac{\sum_{i=1}^n \rho_{2,i} V_{2,i} (V_{2,i} - \bar{V}_2)^2}{\sum_{i=1}^n \rho_{2,i} V_{2,i}} \quad (14)$$

This is simply the mass average of $\sum_{i=1}^n (V_{2,i}/\bar{V}_2 - 1)^2$. The velocity ratio variance is well defined regardless of the quality of the outlet flow.

Data in the outlet flow should be examined for characteristics associated with three regions downstream from the cascade. The first region is at the outlet of the cascade, where the data primarily reflect the influence of the cascade. Immediately downstream of the cascade, the blade wakes begin to dissipate. Lieblein and Roudebush (6) state that changes in the data due to wake dissipation occur mostly in the first half chord length downstream. This region will be called the region of wake mixing, and is considered to include locations through one chord length downstream. The third region includes locations beyond one chord length downstream, where changes in the data are mostly due to the influence of the outlet duct, if one is used.

Cascade Flow Condition

Cascade sidewalls generate secondary flows that can significantly degrade flow quality and cascade performance. The general pattern of secondary flow in a cascade is illustrated in Figures 4, 15, and 16. The specific details of Figures 15 and 16 will be discussed in the "Results" section. As illustrated in Figure 4, air in the low energy sidewall boundary layer migrates from the pressure surface of one blade to the suction surface of the next blade as it moves through the blade passage. This can be seen in the trace of oil dots on the cascade sidewall, shown in Figure 15. The air then moves onto the suction surface of the blade, forming "corner" vortices and causing a local separation of the blade boundary layer as shown in Figure 16. High total pressure losses are observed in that area, causing some blockage and accelerating the flow through the rest of the passage, both of which degrade the quality and two-dimensionality of the flow.

The axial velocity ratio can be used to measure the influence of the corner vortices on the two-dimensionality of the flow. The axial velocity density ratio, used for compressible flows, is defined by

$$AVDR = \frac{\int_{-y/2}^{y/2} (\rho_2 V_{x_2})_{midspan} dy}{\int_{-y/2}^{y/2} (\rho_1 V_{x_1})_{midspan} dy} \quad (15)$$

The midspan location of the measurement is crucial to the calculation of AVDR because it reflects the influence of both corner vortices while excluding their losses. Two dimensional flow produces an AVDR of 1.0, but strong secondary flows could drive the AVDR up to 1.2 or higher. Values above 1.0 represent mass moving from edges toward the middle of the passage, a result of the blockage caused by the corner vortices. Values less than 1.0 represent mass moving from the center toward the edges of the passage, a situation that is not expected in cascade flow. It should be noted that although flow over the center of the blade may not have a spanwise component it may have been influenced (accelerated) by the corner vortices, as in Figure 16, and in that case flow through the passage is not fully two dimensional flow.

Erwin and Emory (7) investigated the relation between flow condition and cascade performance because data from solid wall cascades did not agree with the 2D relationships given above. They established the following criteria for 2D flow.

1. Equal pressures, velocities, and directions exist at different spanwise locations.
2. The static pressure rise across the cascade equals the value associated with the measured turning angle and wake.
3. No regions of low-energy flow other than blade wakes exist. The blade wakes are constant in the spanwise direction.
4. The measured force on the blade equals that associated with the measured momentum and pressure change across the cascade.
5. The various performance values do not change with aspect ratio, number of blades, or other physical factors of the tunnel configuration.

They were able to obtain 2D flow in a porous sidewall cascade, using sidewall and endwall suction to control boundary layers, but could not obtain 2D flow with solid sidewall cascades, even with sidewall suction upstream from the blade row. They concluded that aspect ratios much larger than four would be needed for solid sidewall cascades to approach 2D flow.

Erwin and Emory also measured the performance of a two stage axial flow compressor and found that in regard to turning angle, normal force coefficients, and pressure rise relations the results most closely matched measurements from the porous sidewall cascade with 2D flow. They concluded that data taken from cascades with 2D flow would be the most useful in designing axial flow compressors.

Two dimensional flow may not be attainable, and the lack of 2D flow does not invalidate cascade data. Lieblein (1:187) identifies turning angle and blade surface pressures as the data most affected by non 2D flow, while pressure loss data is largely unaffected. Gostelow (8:40-43) presents methods to correct deviation angle and blade surface pressures using the axial velocity ratio. AVDR results, then, may be used both to indicate the two-dimensionality of cascade flow and to provide a basis for comparison with other data.

Finally, pit wise flow effects need to be considered. The flow velocity, direction, and static pressure should each be periodic near the inlet and outlet of the cascade. Far upstream and far downstream, where the cascade has little influence on the flow, these quantities should be constant. Gostelow (8:31) identifies periodicity of flow between passages as essential for cascade testing. In this study upstream static pressure and downstream velocity were examined to evaluate periodicity.

III. Experimental Apparatus and Procedure

Airflow Source

Airflow for the cascade is provided by a 40 hp centrifugal blower that is rated at 3000 ft³/min (3.35 lbm/sec) at 26 oz. of total head (1.6 psig). The layout of the test facility is shown in Figure 5. Either laboratory air or outside air is pulled through an electrostatic filter and passed through the blower into a nine foot long diffuser. The flow slows to about 20 ft/sec at the stilling chamber entrance. A center body plug in the stilling chamber continues diffusing the flow down to about 10 ft/sec and obstructs the acoustic path between the blower and the test section. The flow then passes through a 40 mesh wire screen, a cloth filter, and a four inch thick aluminum honeycomb for filtering and straightening. A 2D long radius bell mouth nozzle accelerates the flow for entrance into the test section. With the test section attached, the stilling chamber pressure is about 1.4 psig and the static pressure at the test section inlet is about -0.5 psig, giving an inlet velocity of about 500 ft/sec, an inlet Reynolds number of about 2.5 million per foot, and a mass flow of about 3.2 lbm/sec. The test section turns the flow about 30 degrees and exhausts it into the laboratory. The blower warms the air about 25°F above the temperature of its inlet flow, and during some runs the stilling chamber temperature approached a maximum of 120°F. Further information on the cascade test facility and its design is provided by Allison (9).

Test Section and Blades

The test section, shown in Figure 6, has three parts: an inlet duct, the cascade, and an outlet duct. All three sections are 2 in. wide. The inlet duct is about 4 in. long at the top of the cascade and about 8 in. long at the bottom. Ports for turbulence injection are located 3/8 in. into the inlet. They are 1/16 in. diameter and there are seven on each sidewall and one on each endwall. A set of static pressure taps is located about 1.25 in. further downstream, and the middle three of these were joined in a manifold to give the inlet static pressure. A slot for sidewall

boundary layer removal is located $3/8$ in. ahead of and parallel to the blade row. Another set of static pressure taps, used to check flow periodicity, is located $1/8$ in. ahead of and parallel to the blade row.

The outlet duct is about 12.5 in. long. Its endwalls, also called tailboards, are adjustable in angle, and each has four static pressure taps along its length. They were adjusted to minimize their influence on the outlet flow. This was accomplished when there was no gradient in pressure along the length of either tailboard, and pressures on the tailboards were equivalent.

The cascade has seven blades, two used as endwalls, which are positioned to have a solidity (chord/space ratio) of 1.5. The blade is a NACA 64-A905 section with a 2.0 in. span and a 2.0 in. chord for an aspect ratio of 1. Because of its mean line definition, the section's camber angle must be estimated, as described in Appendix A. Using an equivalent circular arc meanline the camber angle is 34.08 degrees, and the blade inlet and outlet angles are 32.56 degrees and -1.52 degrees. With the cascade airflow inlet angle of 34 degrees and the blades set at a stagger angle of 7.75 degrees the incidence angle is -1.56 degrees. The deviation angle can be estimated by correlations of cascade data. The calculations and intermediate values are given in Appendix A. The deviation angle by Howell's correlation (5:58) is 5.36 degrees, and by Lieblein's correlation (1), the deviation angle is 4.77 degrees. These result in an air outlet angle of 3.84 degrees (or 3.25 degrees) and a turning angle of 27.16 degrees (or 27.75 degrees). As will be shown later these are within 1 degree of the angles measured in flow without sidewall suction and within 3 degrees of the angles measured in flow with sidewall suction. Again, the angles are illustrated in Figure 3. This geometry approximates last row stators in an axial flow compressor.

Three blade configurations were investigated, each using a specific blade type for the middle three blades in the cascade. Each configuration will be referenced by the blade type used. Blade 1 was unmodified. Blade 2 had three large crenulations in its trailing edge, each 0.5 in. deep and 0.4 in. wide. Blade 3 had four small crenulations in its trailing edge, each 0.25 in. deep and 0.25 in. wide. Crenulation geometry is illustrated in Figure 7. Measurements in the outlet flow were generally made around the middle blade. A blade of each type was equipped with

suction surface pressure ports, and an unmodified blade (Blade 1) was equipped with pressure surface pressure ports. All surface pressure ports were located within 1/16 in. of the blade centerlines.

Instrumentation

Instrumentation consisted of thermocouples, pressure transducers, a total pressure rake, and an x-hot-film sensor. Two digitizers recorded voltages, and two stepper motors positioned the hot wire sensor or the pressure rake in the exit flow. A Zenith Z-248 computer was used to automate data acquisition and reduction. Figure 8 illustrates the instrumentation setup.

Thermocouples and Pressure Transducers. Four copper-constantan thermocouples (T-type) were used to monitor the stilling chamber temperature, the ambient temperature in the laboratory, and two locations in the hotwire calibrator flow path. An Endevco 8510B pressure transducer (0-5 psid) was used to monitor the stilling tank pressure, another was used in the hotwire calibrator, and a third (0-100 psid) was used to monitor the turbulence injector pressure. Ambient pressure was monitored by a CEC 4-326 (0-15 psia) transducer. Satham P6TC (± 2.0 psid) transducers measured the inlet and outlet static pressures. A set of eleven Satham PM96TC (± 0.5 psid) transducers were used with a total pressure rake to measure the difference between the stilling chamber pressure and the total pressure downstream from the cascade blade row. A Scanivalve model 48S9-3003 pressure channel scanner with a PDCR 23D transducer (0-2.5 psid) was used to measure static pressures at the sidewall ports immediately upstream of the cascade and at the blade surface ports. All of the pressure transducers were powered by Endevco 4423 signal conditioners, which were adjusted to provide full scale output of about 1.5 volts.

The pressure transducers were calibrated by measuring eleven points over the working range of the transducer and using linear regression to obtain a slope. The correlations were all greater than 0.99999. The output at zero pressure was recorded before each run as a reference.

Total Pressure Rake and Stepper Motors. A total pressure rake was the primary instrument for collecting pressure loss and velocity data. The rake, shown in Figure 9, has eleven

tubes of 0.028 in. outer diameter spaced at 0.15 in. for a width of 1.5 in. It spans 75% of the test section width.

Stepper motors were used to position the pressure rake and the hot film sensor in the outlet flow. The stepper motor controllers were New England Affiliated Technologies model 310. These communicate with the computer through the serial port, using RS232 protocol. The stepper motors have 400 steps per revolution. Attached to the traversing mechanism, this translated to less than 0.0005 in. per step.

Hot Wire Anemometry. The hot wire anemometer used was an IFA100 constant temperature anemometer from ThermoSystems, Inc (TSI). The sensor was a TSI model 1241-10 which has two film sensors, 0.001 in. diameter, in an "X" configuration, allowing it to measure two dimensions of velocity and two dimensions of turbulence. The sensor configuration is illustrated in Figure 10. The calibration includes temperature effects, and is based on the equation

$$Nu \left(\frac{T_r}{T_f} \right)^b = A + B \sqrt{Re} + C Re \quad (16)$$

where Nu is the Nusselt number of the sensor, Re is the Reynolds number of flow across the sensor, T_r and T_f are the reference (defined below) and static temperatures of the flow, and A, B, and C are the calibration coefficients. Calculation of the Nusselt number requires the voltage across the sensor, and the velocity term in the Reynolds number is calculated by

$$V_{eff} = V \sqrt{\sin^2 \alpha + k \cos^2 \alpha} \quad (17)$$

where V_{eff} is the effective velocity across the sensor, V is the flow velocity, and k is a calibration constant of about 0.15 which is used to include the influence of flow parallel to the sensor. Temperature dependant fluid parameters included density, thermal conductivity, and viscosity. These were calculated at the Eckert reference temperature (12:304), given by

$$T_r = \frac{1}{2} (T_s + T) + 0.22 (T_{AW} - T) \quad (18)$$

where T_s is the surface temperature, T is the fluid static temperature, and T_{AW} is the adiabatic wall temperature. The calibration is described in detail in Appendix B; the reduction of hotfilm voltages to velocity and direction is given in Appendix C; and the reduction of voltages to components of turbulence intensity is given in Appendix D.

The hot film sensor was calibrated between 225 ft/sec and 600 ft/sec at temperatures between 75°F and 135°F. It was also calibrated for flow direction in a range of ± 20 degrees at 415 ft/sec. Performance of the sensor was evaluated by calculating a velocity percent error and an angle error for the calibration data set. For the velocity calibration the standard deviation of velocity error was 0.29% and the standard deviation of angle error was 0.12 degrees. For the angle calibration the standard deviations were 0.83% and 0.66 degrees, respectively.

Digitizers. The two digitizers used were a Hewlett Packard 3455A digital voltmeter and a ThermoSystems, Inc IFA200. The HP 3455A has six digit resolution and was used in conjunction with an HP 3495A Scanner to acquire primarily pressure and temperature data, including data from the pressure rake and the Scanivalve. The IFA200 has 3½ digit resolution but can sample six channels simultaneously at a rate of 50 KHz. It was used for hot film anemometry because of its simultaneous capability. Despite its coarse resolution the IFA200 provided 0.12% full scale resolution for the hotfilm sensor and 0.2% full scale resolution for the pressure transducers, and these values were thought to be acceptable for testing.

Computer. Much of the instrumentation of the Cascade Test Facility was upgraded for this test. The IFA100, IFA200, NEAT310 stepper motors and controllers, Endevco signal conditioners, Endevco pressure transducers and the ± 0.5 psid Statham pressure transducers are all new to the Cascade Test Facility. In addition, a Zenith Z-248 personal computer was installed to control the instrumentation and to automate data acquisition and reduction.

Originally the data acquisition system was built around a Hewlett Packard 9845B computer, and software was developed to drive the equipment during the past ten years of research with the Cascade Test Facility. The computer had to be replaced due to recent reliability problems, and the software was transferred from HP Basic to MS-QuickBasic 4.5. Most of the software was rewritten, but the data acquisition and reduction schemes were preserved.

As shown in Figure 8, the computer communicates with the IFA100 and IFA200 through the COM1 serial port, and it communicates with the NEAT310 stepper motor controllers through the COM2 serial port. The IFA200 has a card inserted into the computer to provide Direct Memory Access, a technique that has a high rate of data transfer. A National Instruments GPIB interface provides IEEE-488 communication with the HP 3455A DVM and the HP 3495A Scanner. The computer controls the Scanivalve through a block of relays in the HP 3495A Scanner, providing HOME and STEP commands.

Assumptions and Procedure

The stilling chamber static pressure and static temperature, both measured upstream from the 2D bell mouth nozzle, were assumed to be the total pressure and total temperature of the flow entering the test section. The total pressure assumption is based on the following analysis. The area of the test section inlet is 2 in. by 6.85 in., and the diameter inside the stilling chamber is 44 in. (9:5). Given an inlet velocity of 500 ft/sec, an area ratio of 1/111, and assuming no losses in total pressure through the bell mouth nozzle, the velocity in the stilling chamber would be about 4.5 ft/sec. Assuming isentropic flow, temperature and pressure can be related to velocity by

$$\frac{T_0}{T} = \left(\frac{P_0}{P} \right)^{\frac{\gamma-1}{\gamma}} = 1 + \frac{\gamma-1}{2} M^2 \quad (19)$$

For a static temperature of about 110°F (about 570°R) the speed of sound is about 1170 ft/s, making the stilling chamber Mach number about 0.00385. With a static pressure of about 15.8

psia, the difference between static and total pressure in the stilling chamber is about 0.00016 psi. This is about 0.03% full scale of the most sensitive pressure transducers (± 0.5 psid) and is considered to be less than the transducers can resolve. Therefore, the stilling tank static pressure may be taken as the flow total pressure. Likewise, with the static temperature of about 110°F the difference between static and total temperature in the stilling chamber (at 4.5 ft/sec) is 0.001686°F, which is beyond the resolution of the thermocouples and small enough to not affect the ensuing calculations.

Total temperature was assumed to be conserved in the flow through the test section. Assuming isentropic flow and given the total and static pressure at a location downstream, the velocity at that point can then be calculated by

$$V = \sqrt{\left(\frac{2 \gamma R T_0}{\gamma - 1}\right) \left(1 - \left(\frac{P}{P_0}\right)^{\frac{\gamma-1}{\gamma}}\right)} \quad (20)$$

which may be derived from equation (19). The ratio of specific heats, γ , was assumed constant because the range of temperatures encountered was relatively small (80°F to 120°F). Velocities from the pressure rake data were calculated in this way.

Turbulence Injection Effects on Total Pressure. The total pressure cannot be assumed constant when air is injected into the inlet for turbulence generation. The air is injected in a region of developing flow, and significant pressure losses occur. The pressure loss could not be evaluated with the cascade in place because the test section inlet duct did not facilitate a total tube for measuring total pressure. To measure the total pressure downstream from the point of injection, the test section was modified by removing the cascade and adding sidewalls to form a straight duct. Evaluating this straight test section with the pressure rake and the hot film provided information on the pressure loss, turbulence level, and pressure and velocity distribution in the flow downstream from the point of turbulence injection. This flow represents the inlet flow to the cascade.

The total pressure loss was measured between 6 in. and 12 in. downstream from the point of injection. In this region, a loss of about 0.6% (0.1 psi) in absolute pressure was consistently observed with the air injection. No losses were observed in the flow without air injection. The loss due to air injection could be expected to increase slightly with the cascade in place because of its higher inlet velocity. The straight test section inlet velocity was about 440 ft/sec, about 10% less than the 500 ft/sec inlet velocity present with the cascade in the test section. However, the value 0.6% was used to correct total pressure for cascade data taken with the turbulence injection on.

The straight test section was also used to measure freestream turbulence levels. With no air injection, about 0.15% turbulence intensity was measured. With the air injection, the turbulence intensity decayed from 3.5% at 4 in. behind the injection to 1.9% at 12 in. behind the injection, as shown in Figure 11. This suggests that turbulence in the flow entering the cascade should vary from about 3.5% near the top of the cascade (about 4 in. downstream of the injection) to about 2.5% near the bottom of the cascade (about 8 in. downstream of the injection).

Although 3.5% turbulence is less than what is present in rotating turbomachinery, its effect on cascade performance and losses gives an indication of the trends for higher turbulence levels. Also, Gostelow (8:31) indicates that the initial increase in turbulence above a low, cutoff level usually has the strongest effect on performance and losses, whereas further increases have less of an effect, and possibly have little or no effect. According to Roudebush (10:159), freestream turbulence greater than 0.2% has a strong influence on the location of boundary layer transition. Because of the differences between laminar and turbulent boundary layers, the point of transition directly effects the performance and losses of an airfoil.

The air injection used for turbulence generation had a noticeable effect on the pressure and velocity distributions downstream. Velocities from about 5 in. downstream of the injection are averaged and shown in Figure 12. The air injection reduces the velocity by about 2%. Figure 12.a. shows span averaged velocities at different pitch positions. The low velocities are in the wake of injection port jets and are not of great concern because they are relatively small

and periodic nature. When the cascade is placed in the flow, its influence causes much larger velocity variations in the pitch direction at the cascade inlet. Figure 12.b. shows pitch averaged velocities at different span positions. The scale of variation is similar to that in the pitch direction, but the single peak in the middle of the span is of some concern. The peak is about 2.1% greater than the average velocity. This will affect the calculation of the axial velocity density ratio, which uses the average upstream velocity as the centerline upstream velocity. Other centerline data that references the average upstream velocity may also be affected.

The variations in the flow due to the air injection may not invalidate cascade data. However, an understanding of the quality of the inlet flow is necessary for evaluation of these data. Also, the effects of the air injection suggest that a different method of turbulence generation may be more appropriate.

Periodicity and Blade Surface Pressures. Periodicity was evaluated by measuring upstream static pressures and downstream velocities. The static pressures were measured using the Scanivalve and the sidewall ports just ahead of the blade row. Centerline velocities downstream of the cascade were measured over three blade spaces with the hot wire. Blade surface pressures were measured with the Scanivalve, and upstream and downstream pressures were recorded to obtain pressure rise values.

The Scanivalve, the blades with surface ports, and the total pressure rake were checked thoroughly for air leaks, with a number found and corrected. During operation with the pressure rake, measurements downstream from blade passages (out of the blade wakes) provided a convenient check point for pressure rake measurements because virtually no total pressure was lost there. In this way the pressure rake and its transducers were monitored for leaks throughout the data acquisition process.

Downstream Velocity and Pressure Losses. Velocity and pressure loss data were measured with the pressure rake at several distances behind the cascade. In the span direction, the tubes of the pressure rake were located at -0.75, -0.6, -0.45, -0.3, -0.15, 0, 0.15, 0.3, 0.45, 0.6, and 0.75 in. with respect to the centerline. In the pitch direction the data were taken between 0.665 and

-0.665 in. with respect to the trailing edge of the center blade, covering one blade spacing. The data planes were at 0.25c, 0.5c, 0.75c, 1c, 1.25c, 1.75c, 2.25c, 3c, and 4c behind the cascade, with one of three pitch direction spacings. For 0.25c and 0.5c downstream, 134 points spaced at 0.01 in. were used. For 0.75c and 1c downstream, 67 points spaced at 0.02 in. were used, and for 1.25c and back, 28 points spaced at 0.05 in. were used. Due to the size of the wake at 0.25c (wake thickness \approx 0.15 in.) and the steep gradient in its velocity and pressure profiles, it is questionable whether a spacing of 0.01 in. adequately represents it. There is also a possibility that at 0.75c downstream the 0.02 in. spacing was not adequate to accurately represent the wake. This is addressed later in the discussion of results. Finally, at 0.25c and 0.5c downstream the pressure losses from the corner vortex regions passed the limits of some of the 0.5 psi transducers. However, no over-ranged measurements were observed in data further downstream.

Turning Angle and Turbulence Intensity. This data was acquired with the hot wire anemometer. Data for the baseline blade was acquired at 0.25c, 0.5c, 0.75c, 1.25c, 1.75c, and 2.25c downstream. Turning angle variation was less than 0.15 degrees over this range, so one location, 0.5c, was chosen to test the three blades in the different flows. In the pitch direction 68 points spaced at 0.02 in. were taken. In the span direction 5 locations were chosen to represent one crenulation space on each blade. For Blade 1 (unmodified) and Blade 3 (small crenulations) the positions -0.25, -0.125, 0, 0.125, and 0.25 in. were sampled. For Blade 2 (large crenulations) the positions -0.3, -0.15, 0, 0.15, and 0.3 in. were sampled.

Finally, each blade configuration was tested in four flow conditions generated by turning turbulence injection on and off and by turning sidewall suction on and off. The higher freestream turbulence was used to investigate the relationship between turbulence effects and crenulation effects. Removing sidewall suction was used to investigate the possibility of interaction between the crenulation effects and the corner vortices generated by the secondary flow. In the suction off condition, the suction ports were blocked to prevent air from entering the cascade through the suction slots.

IV. Discussion of Results

Three blade configurations were tested in four flow conditions. The configurations are identified by the type of blade used, and are called Blade 1 or "Unmodified", Blade 2 or "Large Cren", and Blade 3 or "Small Cren." The flow conditions are identified by combinations of "Suction on/off" and "Turb on/off." The results are presented in the following order. First, the test flow conditions are evaluated for periodicity and secondary flow effects, as shown by oil dot flow visualization and axial velocity density ratios. Next, the cascade performance is evaluated by blade surface pressures, the static pressure rise across the cascade, and the flow turning angle through the cascade. Finally, losses and wake dissipation are evaluated by the total pressure loss, the wake velocity deficit, and the variance of outlet flow velocities.

Periodicity

In this test periodicity was evaluated by measuring static pressure over four passages at 0.0625c ahead of the cascade row and by measuring velocity over three passages at 2.25c downstream from the cascade.

The test section was first "balanced" by adjusting the tailboards until each had nearly constant (no gradient) and minimal pressures along its length, and the average pressures on the tailboards were nearly equal. The adjustments were made with sidewall suction on and turbulence injection off. The adjustments brought the pressures on each tailboard to about ± 0.02 psig, and the difference between the average pressures on the tailboards was about ± 0.002 psi. These pressures exert little influence on the outlet flow. The angles of the tailboards were measured with respect to the axial direction of the cascade, and are listed in Table 1. The air inlet angle is 31 degrees, so these values suggest that the unmodified blade and the blade with small crenulations turn the flow about 29.5 degrees, and the blade with large crenulations turns the flow about 28.5 degrees. The values are close to those measured by the hot wire anemometer, which are discussed later, and suggest that the tailboard settings are acceptable. For each blade type,

Table 1. Tailboard Angles, degrees, in "Suction on, Turb off" flow

Blade type	Upper Tailboard	Lower Tailboard
Unmodified	1.1	1.7
Large Cren	2.0	2.8
Small Cren	1.1	2.0

balancing the test section resulted in a slight divergence (about 0.75 degrees) of the tailboards.

The upstream static pressures are shown in Figure 13, and are non-dimensionalized by inlet total pressure. These measurements were also taken with sidewall suction on and turbulence injection off. The high pressures occur ahead of the blades, and the low pressures occur ahead of the passages. For comparison, the pressure ratio measured at the test section inlet was 0.8744 for all three blades in "flow condition. The data from the three blade configurations match quite well. Small differences in pressure are present near the ends of the cascade and are likely caused by the tailboard settings which were slightly different for each configuration. These results indicate that the crenulations do not significantly influence the upstream static pressures, and that flow around the center blade is suitable for testing.

There is a trend seen in Figure 13 for higher pressures near the bottom of the cascade (-3 in. with respect to the center blade) and lower pressures near the top of the cascade, indicating that ideal periodicity was not achieved at the cascade inlet. The tailboards were adjusted to try to improve this trend, but it was only degraded. Boundary layer growth near the bottom of the inlet duct may contribute to the upward movement of mass by decelerating the flow near the bottom of the inlet duct. Also, the pressure distribution in a turning flow would have lower pressures near the center of the turn (near the top of the cascade) and higher pressures away from the center of the turn (near the bottom of the cascade). While these suggestions are speculative, the data indicate that better boundary layer control on the inlet sidewalls and endwalls would be necessary to obtain good inlet periodicity.

The velocity measurements used to evaluate periodicity were made with an x-hotfilm sensor at the span centerline, 2.25c downstream of the cascade. The results, shown in Figure 14, are for Blade 1 in flow with sidewall suction on and turbulence injection off and on. In the low turbulence flow, in Figure 14.a., the freestream velocities were $430 \text{ ft/sec} \pm 1 \text{ ft/sec}$ in the four passages, indicating that the flow was essentially periodic in the outlet duct. In the case with turbulent flow, in Figure 14.b., velocities in the wake are similar, but outside of the wake, in the freestream, they are not uniform. This may be due to the higher inlet velocity at the span centerline, discussed earlier and shown in Figure 12. In that case it may be that averaging a set of outlet velocities in the span direction would result in more uniform velocities in the freestream region and would improve the evaluation of periodicity in turbulent flow. In retrospect, measurements closer to the cascade would reflect less influence from the outlet duct, and might have given a better indication of outlet flow periodicity, although the pressures on the tailboards suggest that influence of the outlet duct on the flow was minimal.

The main observations from the evaluation of periodicity are that the upstream static pressures were not ideally periodic, but the downstream velocities were essentially periodic. This gave confidence that the flow quality was suitable for testing, particularly around the center blade.

Secondary Flow Effects

Flow Visualization. The flow visualization results are shown in Figures 15 and 16. In comparing Figures 15.a to 15.b and 15.c to 15.d, it can be seen that with sidewall suction the secondary flow does not move as rapidly down the sidewall. Comparing Figures 15.a to 15.c and 15.b to 15.d shows that increased freestream turbulence also reduces the secondary flow along the sidewall, although to a lesser degree than does the sidewall suction.

The influence of secondary flows on the blade suction surface boundary layers can be clearly seen in Figure 16. There is some separation, shown by the stationary oil dots, and the size of the corner vortex regions corresponds with the strength of the secondary flows on the sidewalls.

A comparison of Figures 16.a. to 16.b. and 16.c to 16.d shows that sidewall suction reduces the size of the corner vortices, but the reduction is not as dramatic in the presence of higher freestream turbulence. Comparing Figures 16.a to 16.c and 16.b to 16.d shows that increasing the freestream turbulence also reduces the corner vortices, although again to a lesser degree than does the sidewall suction.

It is apparent from both Figures 15 and 16 that the secondary flows and corner vortices are strongest in "Suction off, Turb Off" flows, that they are reduced by either suction or increased turbulence, and that the "Suction on, Turb on" flow resulted in the weakest secondary flows. The influence of sidewall suction and freestream turbulence on secondary flows through the cascade is the basis for an understanding of much of the following results.

Axial Velocity Density Ratio. The axial velocity density ratio (AVDR) data is shown in Figures 17 and 18. These data represent the three blade configurations in four flow conditions at nine locations downstream. Each data set is presented in two ways, with both approaches plotting the AVDR values against distance downstream. The first method, shown in Figure 17, has a graph for each blade configuration, allowing comparison of the flow conditions for each blade. The second method, shown in Figure 18, has a graph for each flow condition, allowing comparison of the blades in each flow condition. The data for total pressure loss, wake velocity deficit, and velocity ratio variance are also presented in this format.

In Figure 17, the influence of the different flows on AVDR may be compared, but the trends for each flow condition are more clearly seen in Figure 18. The values are all over 1.0 near the cascade, and they drop toward 1.0 with distance downstream. The "Suction on" cases (Figures 18.a and 18.c) produced lower values than the "Suction off" cases (Figures 18.b and 18.d). This indicates less blockage from the corner vortices and better quality flow, as would be expected from the flow visualization data. In the low turbulence flow (Figures 18.a and 18.b) the AVDR decreases in the first chord length downstream, and then remains nearly constant with distance downstream. This would suggest that changes in the outlet flow due to the corner vortices dissipate quickly, generally within the so called region of wake mixing.

For the higher turbulence flow, shown in Figures 18.c and 18.d, the AVDR may not be trustworthy because of the inlet velocity profile with upstream turbulence injection, described in the previous chapter under "Turbulence Injection Effects on Total Pressure." With turbulence injection, the inlet velocity at the mid-span location was shown to be about 2.7% higher than the average inlet velocity. This peak would likely diminish with distance downstream. Because the calculation of AVDR is referenced to the average inlet velocity (the midspan inlet velocity was not available), the resulting AVDR may be over valued by as much as 2.7%. If AVDR in flows with higher turbulence were decreased by about 2.5% near the cascade and by lesser amounts at locations downstream, the results would be close to the AVDR for the low turbulence flows.

In Figure 18, values of AVDR for the three blade configurations may be compared. In all four flow conditions, the three blades have almost equal values near the cascade, but after one chord length downstream the crenulated blades have higher values, and the increment is almost constant with distance downstream. This indicates that the crenulations have little influence on the flow in the cascade, that they do affect the flow in the region of wake mixing, and they do not affect the flow further downstream. The higher values of AVDR for the crenulated blades indicate higher velocities in the center of the outlet duct and may imply a reduction wake mixing losses. The data in Figure 18 also show that the increment in AVDR for the crenulated blades is about the same for both the "Suction on" and "Suction off" flows, which indicates that the effect of the crenulations on AVDR is not related to the strength of the secondary flows.

Another feature of the data in Figure 18 is that values at the third data point downstream (the $x/c = 0.75$ location) do not follow the trend evident in the rest of the data. (As shown later, the wake velocity deficit data and the velocity ratio variance data also have uncharacteristic values for the third data point, although the pressure loss coefficient data does not.) The uncharacteristic values could indicate a peculiar behavior of the flow, but their regularity would favor a problem in the data acquisition or the calculation of velocities, mass averages, or some other calculation. All of these were investigated. The most likely cause of the irregular data is in the data acquisition procedure and is discussed below.

Data for the first two locations downstream, 0.25c and 0.5c, were acquired by sampling 134 points in the pitch direction, spaced at 0.01 in. to cover one blade space (1.33 in.). Data for the next two locations were acquired by sampling 68 points in the pitch direction, spaced at 0.02 inches. It is likely that at 0.75c downstream the 0.02 in. spacing was not sufficiently dense to adequately represent the wake. If too few points were acquired in the wake (where velocities are low), averaged velocity values would be too high. The value of AVDR at the third data point is higher than the surrounding data. The higher velocity at that point would also cause low values of wake velocity deficit and velocity ratio variance, and both are evident in the data for these parameters.

The main observations from the AVDR and flow visualization results are that flow without sidewall boundary layer removal has strong secondary flows and corner vortices. Both applying sidewall suction and increasing freestream turbulence improve the quality of the flow by reducing the secondary flow and the corner vortices. The crenulations appear to have little influence on flow through the cascade or beyond 1c downstream of the cascade.

Blade Surface Pressures

Blade surface pressures were measured through ports near the centerline of the blades. The location of each port is identified by "S/S₀", where "S" is the distance from the leading edge to the port measured along the surface of the blade, and "S₀" is the length of the blade surface containing the pressure port, either the pressure or suction surface. This format is used because measurements of the port locations in terms of x/c were difficult to obtain due to the camber of the blade. Blade surface pressures are reported as pressure coefficients, calculated by $C_p = (P_s - P_1) / (\frac{1}{2} \rho_1 V_1^2)$ where P_s is the blade surface pressure and P_1 is the static pressure measured at the test section inlet.

Data for the three blades are shown in Figures 19 and 20. Suction surface measurements were obtained for each blade type, but crenulated blades with pressure surface ports were not available, so pressure surface measurements were made only with the unmodified blade.

The regions $S/S_0 = 0.25$ and $S/S_0 = 0.65$ contain the blade mounting pins and therefore lack pressure ports. Also, Blade 2 has only two data points near the leading edge because of leaks in the other ports in that area.

The removal of sidewall suction and the addition of turbulence have similar effects for each blade type, as seen in Figure 19. The removal of the suction decreases pressure on both the suction and pressure surfaces of Blade 1. This is most likely caused by the increase in axial velocity ratio (AVR) when the suction is removed; the increase of velocity causes the pressure to drop. Gostelow (8:43) indicates that an increase in AVR will cause a slight decrease in pressure on both the suction and pressure surfaces. He also states that the decrease on the pressure surface should be uniform. This is evident in Figure 19.a where the decrease in pressure with the removal of suction is uniform along the pressure surface and along most of the suction surface of Blade 1. However, near the leading edge on the suction surface, the change in pressure with the removal of suction goes to zero. The reduction in pressures Figure 19.a indicates an increase in velocity through the passage, except near the suction surface leading edge.

Given the near uniform decrease in pressure on both surfaces, seen in Figure 19.a, the lack of a decrease near the leading edge on the suction surface indicates a decrease in the area between the suction and pressure surface pressures for Blade 1. This would cause a slight decrease in the lift force on the blade, which in turn would cause a slight decrease in the turning angle of the flow. The turning angle results, reported later in Table 4, do show a decrease in turning angle of about 0.3 degrees with the removal of suction for each blade type.

In the case of increased turbulence, shown again in Figure 19.a, the pressures on both surfaces of Blade 1 were marginally increased. The change in pressure is uniform over the back half of the blade on both surfaces. However, near the leading edge of the pressure surface the change goes to zero, and near the leading edge of the suction surface the change increases. The increase in pressure with increased freestream turbulence corresponds best with the influence of the turbulence to decrease secondary flows in the passage. A reduction of the corner vortices would reduce the velocity and increase the static pressure in the passage.

In Figure 19.a, the changes in surface pressure with the addition of turbulence, particularly near the leading edge, appear to cause a slight decrease in area between suction and pressure surface pressures. This would cause a slight decrease in the lift force, and would result in lower turning angles. Again, the turning angle data in Table 4 do show a decrease in turning of about 1 degree with the higher freestream turbulence.

In Figures 20.a, 20.b, and 20.c, the data are plotted to compare the three different blades. The first observation is that the pressures on the blades are nearly equal over the latter 2/3 of the blade in each flow condition. This would suggest that the crenulations have little influence on the blade surface pressures. Near the leading edge, however, the pressures differ in a pattern that is consistent in each flow, suggesting that the crenulations have some influence on the blade surface pressures. Blade 2 has the lowest pressures at the first data point in all of the flows, indicating that velocity over the suction surface near the leading edge is highest for Blade 2 in all of the flows. This implies that the leading edge stagnation point on Blade 2 may have moved slightly aft. Also, Blade 2 had a crenulation at the span centerline (and Blade 3 did not), a feature which would tend to move the trailing edge stagnation point forward. These observations suggest that the crenulations cause the stagnation points to move closer together at the span location of the crenulation. Measurements of surface pressures at several span locations on a crenulated blade would be needed to evaluate this possibility.

The main observations from the surface pressure data are that the changes in pressure at the different flow conditions are associated with the influence of the sidewall suction and increased freestream turbulence on the secondary flows. The changes in pressure also correspond to the changes in flow turning angle. The crenulations had almost no influence on the blade surface pressures, except near the leading edges.

Static Pressure Rise

Pressure rise through the cascade is reported as a coefficient of static pressure, also designated C_p , and is calculated in equation (4) by $C_p = (P_2 - P_1)/(\frac{1}{2}\rho_1 V_1^2)$. Values of C_p have

an estimated accuracy of 0.002. The inlet and outlet static pressures, P_1 and P_2 , were measured by sidewall taps at the test section inlet and 0.25c downstream, respectively. Table 2 lists the cascade pressure data for the three blade configurations. In the cases with the turbulence injection, the inlet total pressure is corrected downward by a factor of 0.994 to account for loss due to the turbulence injection. In Table 2 it is evident that the turbulence injection reduces the inlet total pressure, decreasing the inlet velocity by about 2%. Removing sidewall suction increases the inlet static pressure, decreasing the inlet velocity by about 4%.

Comparisons of C_p data for the three blade configurations and the four flow conditions are shown in Table 3 and in Figure 21. Table 3.a lists the values of C_p . Table 3.b lists the percent change from the "Suction on, Turb off" flow condition, allowing evaluation of the effect of the flow conditions on C_p . Table 3.c lists the percent change from the unmodified blade, allowing evaluation of the effect of the crenulated blades on C_p .

Table 2. Cascade Pressure Data

Blade 1 Unmodified				
$T_0 = 107^\circ\text{F}$, $P_{\text{ambient}} \approx 14.165$ psia				
	Suction on Turb off	Suction on Turb on	Suction off Turb off	Suction off Turb on
P_{01} , psia	15.621	15.576	15.643	15.588
P_1 , psia	13.659	13.683	13.805	13.808
V_1 , ft/sec	506	497	488.9	481.5
$\rho_1 V_1^2/2$, psi	1.872	1.812	1.757	1.708
P_2 , psia	14.160	14.173	14.167	14.176
$P_2 - P_1$, psi	.501	.490	.362	.368
C_p	.2676	.2704	.2060	.2155

Table 2, continued. Cascade Pressure Data

Blade 2 Large Crenulations				
$T_0 = 109^\circ\text{F}$, $P_{\text{ambient}} \approx 14.191$ psia				
	Suction on Turb off	Suction on Turb on	Suction off Turb off	Suction off Turb on
P_{01} , psia	15.646	15.596	15.666	15.610
P_1 , psia	13.682	13.702	13.826	13.831
V_1 , ft/sec	506.7	498.1	489.6	481.9
$\rho_1 V_1^2/2$, psi	1.871	1.814	1.759	1.707
P_2 , psia	14.176	14.192	14.184	14.194
$P_2 - P_1$, psi	.494	.488	.358	.363
C_p	.2640	.2690	.2035	.2126
Blade 3 Small Crenulations				
$T_0 = 110.5^\circ\text{F}$, $P_{\text{ambient}} \approx 14.194$ psia				
	Suction on Turb off	Suction on Turb on	Suction off Turb off	Suction off Turb on
P_{01} , psia	15.645	15.594	15.667	15.609
P_1 , psia	13.682	13.701	13.831	13.830
V_1 , ft/sec	507.3	498.7	489.7	482.5
$\rho_1 V_1^2/2$, psi	1.871	1.812	1.756	1.707
P_2 , psia	14.179	14.195	14.190	14.197
$P_2 - P_1$, psi	.497	.494	.364	.367
C_p	.2656	.2726	.2073	.2149

Table 3. Static Pressure Rise Comparisons

3.a. Pressure Rise, C_p , ± 0.002				
Blade type	Suction on Turb off	Suction on Turb on	Suction off Turb off	Suction off Turb on
Unmodified	.2676	.2704	.2060	.2155
Large Cren	.2640	.2690	.2035	.2126
Small Cren	.2656	.2726	.2073	.2149
3.b. Comparison of C_p with "Suction on, Turb off" Flow, %				
Blade type	Suction on Turb off	Suction on Turb on	Suction off Turb off	Suction off Turb on
Unmodified	0	1.05	-23.02	-19.47
Large Cren	0	1.89	-22.92	-19.47
Small Cren	0	2.64	-21.95	-19.09
3.c. Comparison of C_p with Unmodified Blade, %				
Blade type	Suction on Turb off	Suction on Turb on	Suction off Turb off	Suction off Turb on
Unmodified	0	0	0	0
Large Cren	-1.35	-0.52	-1.21	-1.35
Small Cren	-0.75	0.81	0.63	-0.28

In examining the effect of the different flow conditions on C_p (Table 3.b and Figure 21), it is evident that increasing the turbulence increases the pressure rise by as much as 2.5% and removing sidewall suction decreases the pressure rise by as much as 23%. Both of these results are related to the secondary flows. Increasing turbulence decreases the effects of the corner vortices, improving the flow quality and in turn the pressure rise. Removing sidewall suction increases the corner vortices, degrading the flow quality and the pressure rise. The reduction in

C_p with the removal of sidewall suction is rather large, but Erwin and Emory (7) reported similar measurements.

Erwin and Emory (7) investigated both a solid wall cascade and a porous wall cascade with 2D flow, both having an aspect ratio of one. Their data, reported as the ratio of outlet to inlet dynamic head, shows an increase from about 0.46 with the porous wall cascade to about 0.61 with the solid wall cascade, at a turning angle of 21 degrees.

These values can be converted to C_p in the following manner for comparison with the values in Table 3:

$$P_0 = P + Q \quad (21)$$

$$\frac{P_{02} - P_{01}}{Q_1} = \frac{P_2 - P_1}{Q_1} + \frac{Q_2}{Q_1} - 1 \quad (22)$$

$$C_p = (1 - Q_2/Q_1) - \bar{\omega} \quad (23)$$

If the total pressure loss is small, changes in $1 - Q_2/Q_1$ can be associated with changes of similar magnitude in C_p . With their data, C_p is 0.54 for the porous wall cascade and 0.39 for the solid wall cascade, a decrease of 27% for the latter and comparable to the 23% loss with the removal of sidewall suction shown in Table 3.b.

Table 3.b also shows that the crenulated blades accommodate different flows a little better than does the unmodified blade. Increasing the turbulence in the "Suction on" cases increases the pressure rise by 2.6% for the small crenulations, by 1.9% for the large crenulations, and by 1% for the unmodified blade. In the "Suction off" cases the crenulated blades had the smallest decrease in pressure rise as compared to the "Suction on, Turbulence off" case.

Table 3.c and Figure 21 both allow a comparison of C_p for the different blades. The large crenulations diminished the pressure rise by as much as 1.35% in the different flows. The small

crenulations diminish the pressure rise less, and in the "Suction on, Turbulence on" and "Suction off, Turbulence off" cases they actually increase the pressure rise by as much as 0.8%.

The main observation from the pressure rise data is that removing the sidewall suction seriously degraded the cascade performance, while increasing the freestream turbulence slightly improved the performance. The crenulations have little influence on the pressure rise in the flow conditions tested, but the small crenulations are favored by a slight margin.

Turning Angle

Measurements of flow turning angle were made downstream of the cascade with an x-hotfilm which had an estimated accuracy of ± 0.35 degrees. The measured turning angles are shown in Table 4.a and Figure 22, and comparisons between the flow conditions and the blades are shown in Tables 4.b and 4.c, respectively. In Table 4.b it can be seen that increasing the turbulence reduced the turning angle by an average of 0.93 degrees, and removing the sidewall suction reduced the turning angle by an average of 0.32 degrees. The changes with turbulence and suction appear to be independent of each other, and in combination they are additive, as seen in Table 4.b and in Figure 22. The large crenulations decreased the turning angle by an average of 0.84 degrees, and the small crenulations decreased the turning angle by an average of 0.35 degrees. These values also suggest that the crenulations do not significantly influence the turning angle, though the smaller crenulations are again slightly favored.

The changes for different flows are in accord with the blade surface pressure results, but the reduction of turning with higher turbulence is counter to the increase in static pressure rise with higher turbulence, discussed in the previous section. Values of turning angle may be calculated from the static pressure rise, providing a more convenient comparison with turning angle results.

Turning angles were calculated from the static pressure rise using equation (4) with the assumption of no losses, and are shown in Table 5.a. Their differences from the measured turning angles are listed in Table 5.b. With the assumptions of 2D flow and no losses, equation (4)

Table 4. Measured Turning Angles

4.a. Measured Turning Angles, ± 0.35 degrees				
Blade type	Suction on Turb off	Suction on Turb on	Suction off Turb off	Suction off Turb on
Unmodified	30.29	29.41	29.87	29.04
Large Cren	29.43	28.47	29.17	28.19
Small Cren	29.93	28.99	29.65	28.65

4.b. Difference from "Suction off, Turb on" Flow, degrees				
Blade type	Suction on Turb off	Suction on Turb on	Suction off Turb off	Suction off Turb on
Unmodified	0	-0.88	-0.42	-1.25
Large Cren	0	-0.96	-0.26	-1.24
Small Cren	0	-0.94	-0.28	-1.26

4.c. Difference from Unmodified Blade, degrees				
Blade type	Suction on Turb off	Suction on Turb on	Suction off Turb off	Suction off Turb on
Unmodified	0	0	0	0
Large Cren	-0.86	-0.94	-0.70	-0.85
Small Cren	-0.36	-0.42	-0.22	-0.39

becomes $C_p = 1 - \cos^2 \alpha_1 / \cos^2 \alpha_2$, and may only be regarded as a rough estimate of the relationship. In the "Suction on" cases in Table 5.b, the measured values are as much as 2.8 degrees less than the calculated values, and in the "Suction Off" cases in Table 5.b the measured values are as much as 2.9 degrees greater than the calculated values. These contrasting effects are disconcerting but not unexpected. Erwin and Emory (7:12) indicate that counteracting effects influence the turning in a solid wall cascade. Secondary flows in the passage, and corner vortices

Table 5. Calculated Turning Angles

5.a. Turning Angles Calculated from Static Pressure Rise,degrees				
Blade type	Suction on Turb off	Suction on Turb on	Suction off Turb off	Suction off Turb on
Unmodified	31.15	31.33	26.99	27.65
Large Cren	30.92	31.24	26.81	27.46
Small Cren	31.02	31.47	27.08	27.62
5.b. Difference from Measured Turning Angles, degrees				
Blade type	Suction on Turb off	Suction on Turb on	Suction off Turb off	Suction off Turb on
Unmodified	-0.86	-1.92	2.88	1.39
Large Cren	-1.49	-2.77	2.36	0.73
Small Cren	-1.09	-2.48	2.57	1.03

in particular, tend to decrease blade lift and consequently the cascade turning angle. However, increases in axial velocity tend to increase the turning. Depending on which effect predominates, the measured turning angle may be greater than or less than the turning angle associated with the static pressure rise. Their solid wall cascade of aspect ratio one produced turning angles comparable to those of a similarly configured axial flow test compressor (which had nearly 2D flow), but did not produce the pressure rise associated with that turning angle. This corresponds to the results of the "Suction off" flow cases which had a low static pressure rise in comparison to the flow turning angle, and suggests that influence of axial velocity predominated in this case.

In the "Suction on" flow cases, however, the influence of the secondary flows may have predominated, so that the reduction of secondary flows with suction may have decreased total pressure losses and increased static pressure rise. In that case the turning angle would depend on the magnitude of the changes to pressure loss and pressure rise, and may increase or decrease

slightly. In Table 4.b it is evident that applying suction increased the turning angle by about 0.3 degrees, but the calculated turning angles in Table 5.a are still higher. This suggests that applying suction reduced total pressure losses, allowing an increase in static pressure without a corresponding increase in turning angle. The decrease in turning angle with turbulence in the "Suction on" flow despite the increase in static pressure rise with turbulence may be explained in the same way. The effect of turbulence to reduce secondary flows and consequently reduce the total pressure loss may allow the increase in static pressure rise (seen in the higher calculated turning angles) in spite of the slight decrease in turning (about 0.9 degrees). It is evident that the relationship between flow turning angle and static pressure rise is influenced by secondary flows in the passage, and in the case of a solid wall cascade with an aspect ratio of one the results are difficult to predict. A further point to consider in regard to the calculation of turning angles is the sensitivity of turning angle to changes in static pressure, which is discussed below.

Estimates for the turning angle were given in Chapter III. The deviation angle by Howell's correlation (5:58) is 5.36 degrees, and by Lieblein's correlation (1) the angle is 4.77 degrees, resulting in a turning angle of 27.16 or 27.75 degrees, respectively. Both estimates are lower than the measured turning angles. However, they are close to the calculated values of turning angle in the "Suction off" cases. This may suggest that the correlations are based on solid sidewall cascades without boundary layer control, but Lieblein states that turning angle data from cascades with questionable two-dimensionality of flow were rejected (1:187). The discrepancies between the correlation estimates and the measured values are not easily accounted for. An explanation may be based in part on the nature of equation (4) which relates the static pressure rise to the flow turning angle. As α_2 approaches zero the turning angle becomes very sensitive to changes in pressure. With an air inlet angle of 31 degrees, an air outlet angle of 0 degrees yields a pressure rise coefficient of 0.2653 while an air outlet angle of 5 degree yields a pressure rise coefficient of 0.2596.

The main observations from the turning angle data are that the results correspond to the blade surface pressures but not to the static pressure rise, and that the crenulations have a small

effect on the turning angle. The large crenulations decrease the turning angle by about 0.8 degrees and the small crenulations decrease the turning angle by about 0.3 degrees in each of the flow conditions tested.

Total Pressure Loss Contours

The total pressure loss results come from several sets of measurements, each of which represents an area normal to the axial direction at a given distance downstream from the cascade. In this section, the total pressure loss coefficient is shown as contour levels at a specified downstream location. In the following section, called "Total Pressure Losses", mass averages of the total pressure loss coefficient are shown at each downstream locations. As explained earlier, in the flows with turbulence injection the measured inlet total pressures were reduced by about 0.6% to accommodate losses incurred by injection into the developing flow immediately downstream of the stilling tank's bell mouth nozzle. The correction was determined by measuring total pressures downstream of the injection in a straight duct. The inlet total pressure for flows with turbulence injection was calculated by applying a factor of 0.994 to the stilling tank total pressure.

Pressure loss contours at 1c downstream for Blades 1, 2, and 3 are shown in Figures 23, 24, and 25, respectively. The edge dimensions are given in inches, and show that data was taken in one blade space ($\pm s/2$ with respect to the center blade) over a width of 1.5 in. The large areas of pressure loss near the sides are due to the corner vortices. The large areas with no contours, near the top and near the bottom of the measurement window, have almost no pressure loss. The following discussion pertains to all three blade configurations, as the different flows cause similar effects on each.

Removing the sidewall suction caused higher losses and greater passage blockage, as can be seen in comparing Figure 23.a to 23.b and 23.c to 23.d. This was expected from the flow visualization data. The increased blockage in the corners accelerates the flow through the rest of the passage, increasing the AVDR and decreasing the blade surface pressures in the "Suction off"

cases. Results discussed earlier support both an increase in AVDR and a decrease in surface pressures with the removal of sidewall suction.

In the "Suction on" cases, shown in Figures 23.a and 23.c, increasing the freestream turbulence does not change the maximum level of pressure loss, but seems to spread the loss over a larger area, resulting in a larger overall pressure loss. The mass averaged pressure loss coefficient, discussed later, does show an increase in loss with higher turbulence. This is counter to the trends associated with increased freestream turbulence as described by Roudebush (10), and merits additional attention.

Normally, increased freestream turbulence decreases pressure loss, particularly in the range of Reynolds numbers where separation and stall begin to occur. The freestream turbulence causes an earlier transition to a turbulent boundary layer, which can withstand a greater adverse pressure gradient before separating (10:166). This results in lower pressure losses with higher freestream turbulence. However, at high Reynolds numbers, where turbulent separation is not present, forward movement of the point of transition could cause higher pressure losses (10:176). In the absence of separation, and with an earlier transition due to increased freestream turbulence, the rapid growth of the turbulent boundary layer would result in larger boundary layers at the trailing edge, and therefore a greater pressure loss.

A comparison of Figures 23.a and 23.c shows that increased freestream turbulence does produce a thicker wake. The flow visualization data presented earlier does not show separation over the suction surface of the blade, except in the corner vortex regions. Therefore, the flow may be in the range of Reynolds numbers where the forward movement of the point of transition would increase the pressure loss. The blade-chord Reynolds numbers during testing were about $4 \cdot 10^5$, somewhat above the value of $2.5 \cdot 10^5$ associated with large increases in pressure loss in similar cascades (1:206). This is a possible explanation for slightly increased pressure losses with increased freestream turbulence. However, Roudebush (10:180) concludes that losses are very sensitive to blade-chord Reynolds numbers and to freestream turbulence. Given these

uncertainties, no strong conclusions can be derived from the pressure loss being larger for the flows with increased turbulence.

In the "Suction off" cases, shown in Figures 23.b and 23.c, increasing freestream turbulence reduces the level of pressure loss in the region of the corner vortices, and seems to slightly increase the area of pressure loss, particularly near the midspan. This indicates that increased freestream turbulence tends to increase the thickness of the boundary layers at the trailing edge of the blades, as was seen in the "Suction on" cases discussed above. In the "Suction off" cases the influence of freestream turbulence on the overall pressure loss is not clear.

In Figures 24.a and 25.a, the influence of the crenulations on the pressure loss contours can be clearly seen. The areas where the wake seems to sag correspond to the locations of the crenulations. The large crenulations in Blade 2 are located at -0.45, 0, and 0.45 in. with respect to the midspan. The small crenulations in Blade 3 are located at 0.6, 0.3, 0, -0.3, and -0.6 in with respect to the midspan.

The main observation from the contours of the total pressure loss coefficient is that the removal of sidewall suction results in higher losses (especially in the suction surface corners) and in significant passage blockage. The influence of turbulence on total pressure losses was not clear.

Total Pressure Losses

Total pressure losses are composed of losses through the cascade, wake mixing losses, and outlet duct losses. According to Lieblein and Roudebush (6), the majority of wake mixing losses are assumed to occur by $0.5c$ downstream. The data are presented in Figures 26 and 27, and range from $0.25c$ to $4c$ downstream.

The data in Figures 26.a, 26.b, and 26.c show that changes in pressure loss with different flow conditions are similar for each of the blades. Applying sidewall suction decreases the pressure loss coefficient by 40% to 50%. This is mostly due to the reduction of the corner vortices and their associated loss of pressure. Increasing the freestream turbulence level in flow with sidewall suction resulted in losses near the cascade ($x/c = 0.25$) which were increased for

Blades 1 and 2, and equivalent for Blade 3. However, losses in the higher turbulence flow grew more rapidly with distance downstream than the losses in low turbulence flow. Increasing turbulence level in the flow without sidewall suction resulted in lower pressure losses near the cascade, but the losses again grew more rapidly with distance downstream, exceeding losses in the low turbulence flow for $x/c \geq 2.5$ downstream. The rapid growth of pressure losses with distance downstream is mostly due to turbulent flow through the outlet duct. The cascade losses, reflected in the data near the cascade, increased with higher turbulence in flow with suction and decreased with higher turbulence in flow without suction. The influence of turbulence and cascade losses was addressed in the discussion of pressure loss contours, and it was suggested that no strong conclusions could be drawn from small changes in pressure loss with variations in freestream turbulence.

The data are plotted in Figure 27 to compare the three blade configurations, and it is shown that the crenulated blades produce significantly lower pressure losses in all four flow conditions. In the low turbulence flows the losses are about equal near the cascade, but in the higher turbulence flows the losses are lower for the crenulated blades, indicating that the crenulations have some influence on losses through the cascade. Further downstream, the crenulated blades have significantly lower pressure losses, and the improvement is essentially constant beyond $1c$ downstream, indicating that the outlet duct losses do not degrade the improvements realized by the crenulation blades. The action of the crenulations to reduce pressure losses occurs mainly in the region of wake mixing.

The data in Figure 27 beyond one chord length downstream, where the differences between blades are nearly constant, were used to calculate the change in pressure loss coefficient from the unmodified blade. For each blade, values of percent change at locations further than one chord length downstream are averaged and then shown in Table 6. It can be seen in Table 6 that the large crenulations produce the largest decrease in pressure loss in low turbulence flow, while the small crenulations produce the largest decrease in pressure loss in higher turbulence flow, suggesting that the effects of larger crenulations are perhaps smeared out by higher freestream

Table 6. Decrease in Total Pressure Loss with Crenulated Blades

Decrease in Total Pressure Loss Coefficient, %				
Blade type	Suction on Turb off	Suction on Turb on	Suction off Turb off	Suction off Turb on
Unmodified	0	0	0	0
Large Cren	20	14	14	12
Small Cren	17	18	12	16

turbulence. It is not clear what causes this change, but it may involve crenulation geometry, interaction with freestream turbulence, and possibly interaction with the corner vortices. Part of the explanation could be that the span dimension of the area sampled (± 0.75 in.) covers a whole number of small crenulations but not a whole number of large crenulations.

Finally, the value of pressure loss coefficient estimated from Howell's correlation (5:59) is about 0.017, and from Lieblein's correlation (1) is 0.01986. The calculations are presented in Appendix A. The lowest measured value is about 0.025, seen in the "Suction on, Turb off" flow in Figure 27.a at 0.25c downstream. The agreement of these numbers gives confidence in the accuracy of the pressure loss measurements and in the quality of that flow condition.

The main observation from the pressure loss data is that the crenulations reduce pressure loss from 10% to 20%, depending on the size of the crenulation and the condition of the flow. Also, there appears to be some interaction between the freestream turbulence level and the crenulation size.

Wake Velocity Deficit

Wake velocity deficit data are presented in Figures 28 and 29. As described in the theory and by equation (10), the wake velocity deficit (WVD) will have a small value near the cascade where the wake is small. The WVD increases as the wake mixes into the flow, but will go to zero when the flow becomes uniform. These trends are evident in the data. Figure 28 shows that

applying sidewall suction reduces the WVD, while increasing the freestream turbulence increases the WVD. When combined, these effects appear to be additive.

In Figure 29, both crenulated blades show significant reductions in WVD in all four flow conditions. In the flow with low turbulence, the large crenulations have the lowest values, but in the flows with higher turbulence the two crenulated blades have nearly the same values. This observation further supports the possibility of interaction between the freestream turbulence and the crenulation size. Values for percent reduction from the unmodified blade are calculated as described for the pressure loss coefficient, and are listed in Table 7. The addition of turbulence with suction on has a dramatic effect on WVD, perhaps indicating that for very high levels of turbulence the effect of the crenulations may be significantly smaller.

Table 7. Decrease in Wake Velocity Deficit with Crenulated Blades

Decrease in Wake Velocity Deficit, %				
Blade type	Suction on Turb off	Suction on Turb on	Suction off Turb off	Suction off Turb on
Unmodified	0	0	0	0
Large Cren	23	9	16	11
Small Cren	18	8	13	9

Outlet Velocity Variance

The mass averaged outlet velocity variance is presented in Figures 30 and 31, and the unweighted velocity variance is presented in Figures 32 and 33. The overall trend is for the data to drop quickly toward zero from an initial value in the first chord length downstream, after which they slowly approach zero with distance downstream. This trend seems to provide a good representation of wake dissipation, most of which occurs by $0.5c$ downstream.

The data in Figure 30 show that applying sidewall suction reduces the variance at all downstream locations. The change is substantial near the cascade, but decreases with distance downstream. At 4c downstream the difference between the "Suction off" and "Suction on" cases is rather small. This suggests that the variance is sensitive to variations in outlet flow velocities caused by changes in the level of secondary flow in the cascade.

As seen in Figure 30, an increase in freestream turbulence affects the variance most through 2c downstream, after which it has little influence on the variance. In the flow without sidewall suction, increased turbulence decreases the variance near the cascade, but in the flow with suction on the increased turbulence increases the variance near the cascade. It is likely that in the flow without suction, the reduction of secondary flows and corner vortices with higher freestream turbulence may be causing the value of the variance to decrease. In the flow with sidewall suction on, the secondary flows have already been reduced and increased turbulence will not reduce them much further. However, the velocity fluctuation of the freestream turbulence may be causing the variance to increase. In either case, the contrasting effects with increased turbulence are eliminated by 2c downstream, indicating that the influence of the turbulence on the variance is primarily limited to the region of wake mixing.

The effects of the crenulations on the variance are compared in Figure 31. In all four flow conditions the variance with the crenulated blades is significantly lower than for the unmodified blades at every location downstream. The crenulations do not seem to affect the rate of variance decay, as estimated by the slope of the variance near the cascade.

As before, the difference in variance values from the unmodified blade are calculated at locations from 1c to 4c downstream, and the averages are listed in Table 8. The difference in values in that region appear to be related by a constant ratio. In three of the flow conditions, the blades with large crenulations have marginally lower values at every location downstream, but in the "Suction off, Turb off" flow the crenulated blades had nearly equivalent values.

The unweighted velocity variance is shown in Figures 32 and 33 for comparison. The mass averaged values are lower at every downstream location. The difference between the

Table 8. Decrease in Outlet Velocity Variance with Crenulated Blades

Decrease in Velocity Ratio Variance, %				
Blade type	Suction on Turb off	Suction on Turb on	Suction off Turb off	Suction off Turb on
Unmodified	0	0	0	0
Large Cren	37	25	23	24
Small Cren	26	20	21	21

two is larger near the cascade than at locations downstream, where the wake has mostly dissipated and there is little variation in mass flow.

The main observations from the velocity ratio data are that applying the sidewall suction causes a significant reduction in the variance while increasing the freestream turbulence causes a marginal increase in the variance with suction on and a marginal decrease in the variance with suction off. The crenulations reduce the variance by 15% to 30% in all four flows at all downstream location.

V. Conclusions and Recommendations

Conclusions

Removing the sidewall boundary layer through a slot upstream of the cascade and increasing the freestream turbulence level of the inlet flow both had strong effects to reduce the secondary flows in the blade passages and to reduce the formation of corner vortices on the blade suction surfaces. With sidewall suction, flow through the cascade may represent that of a larger aspect ratio cascade.

The influence of sidewall suction and freestream turbulence on cascade performance measurements were mostly due to the associated changes in secondary flows. Applying suction increased the rise in static pressure and reduced the total pressure losses through the cascade, both by substantial margins. Higher freestream turbulence also increased the static pressure rise (by a lesser margin), but its influence on total pressure losses was not clear. Changes in blade surface pressures corresponded to the changes in the flow turning angles. However, the changes in static pressure rise did not correspond to the changes in flow turning, as could be expected with solid sidewall cascades.

The crenulated trailing edge blades used in this study reduced total pressure losses, wake velocity deficit and outlet velocity variance by 10% - 20% in flow downstream from the cascade. They also reduced turning angle by about 1 degree and reduced pressure rise across the cascade by about 1%. These values show that crenulations can be used to improve wake dissipation characteristics without seriously compromising cascade performance. The crenulation effects appear to be independent of (and additive to) the effects of both freestream turbulence and secondary flows (with their associated corner vortices.)

The influence of the crenulations on cascade outlet flow is most evident in the first chord length downstream. It seems that the crenulations may reduce losses due to wake mixing as well

as enhancing the rate of wake mixing. Because of this, crenulations would seem to be well suited for use either between stages in an axial compressor or as outlet guide vanes.

Recommendations

1. In this study, the inlet flow velocity gave a blade-chord Reynolds number of about $4 \cdot 10^5$. It would be useful to investigate the effects of crenulations over a range of Reynolds numbers, particularly the lower Reynolds numbers, where separation and stall begin to occur.

2. This study used a highly cambered airfoil with a large turning angle, a configuration which models the last row stators of an axial flow compressor. It would be useful to investigate crenulation effects on a cascade that models a typical compressor stage, where the blades have less camber, lower turning angles, and are set at higher stagger angles.

3. In this study the blades were set at one incidence angle. It would be useful to investigate crenulation effects over a range of incidence angles. Would they delay the onset of stall at higher incidence angles, or would they cause premature separation and stall?

4. Crenulation geometry is defined by the depth, width, and space between crenulations. It would be useful to investigate the relationship between these three parameters.

5. In the case of total pressure loss, the large crenulations produced slightly lower values than the small crenulations in flow with low freestream turbulence. However, in the flow with higher turbulence the small crenulations produced values slightly lower than the large crenulations. This reversal could involve both the crenulation geometry and interactions between the crenulation effects, freestream turbulence, and the corner vortex effects. It would be useful to further investigate each of these quantities.

References

1. Lieblein, Seymour. "Experimental Flow in Two-dimensional Cascades," Aerodynamic Design of Axial Flow Compressors (Revised), edited by Irving A. Johnson and Robert O. Bullock. NASA SP-36. Washington: National Aeronautics and Space Administration, 1965.
2. Wennerstrom, Arthur J. "Vane Configuration for Fluid Wake Re-energization", United States Patent Number 4,318,669, 1982.
3. Veasart, J. L., King, P. I., Elrod, W.C., and Wennerstrom, A.J., "Wake Mixing Improvements in a Linear Compressor Cascade with Crenulated Trailing Edges," ASME Paper 90-GT-218, Brussels, Belgium, June 1990.
4. Cohen, H., G. F. C. Rogers, and H. I. H. Saravanamuttoo. Gas Turbine Theory (Third Edition). New York: John Wiley & Sons, 1987.
5. Horlock, J. H. Axial Flow Compressors. London: Butterworths, 1958.
6. Lieblein, Seymour, and William H. Roudebush. Low Speed Wake Characteristics of Two-Dimensional Cascade and Isolated Airfoil Sections. NACA TN-3771. Washington: National Advisory Committee for Aeronautics, 1956.
7. Erwin, John R., and James C. Emery. Effect of Tunnel Configuration and Testing Technique on Cascade Performance. NACA TN-2028. Washington: National Advisory Committee for Aeronautics, 1950.
8. Gostelow, J. P. Cascade Aerodynamics. New York: Pergamon Press, 1984.
9. Allison, Dennis M. Design and Evaluation of a Cascade Test Facility. MS Thesis GAE/AA/81D-2. School of Engineering, Air Force Institute of Technology (AU), Wright-Patterson AFB OH, June, 1982.
10. Roudebush, William H., and Seymour Lieblein. "Viscous Flow in Two-dimensional Cascades," Aerodynamic Design of Axial Flow Compressors (Revised), edited by Irving A. Johnson and Robert O. Bullock. NASA SP-36. Washington: National Aeronautics and Space Administration, 1965.
11. Abbot, Ira H., and Albert E. von Doenhoff. Theory of Wing Sections. New York: Dover Publications, Inc., 1959.
12. Kays, William Morrow and Michael E. Crawford. Convective Heat and Mass Transfer. New York: McGraw Hill, 1980.
13. Schlichting, H. Boundary Layer Theory (Seventh Edition). New York: McGraw Hill, 1979.
14. Bradshaw, P. An Introduction to Turbulence and its Measurement. New York: Pergamon Press, 1971.

15. Galassi, Lello. Turbulence Scale Effects on Heat Transfer in a Linear Turbine Cascade. MS Thesis GAE/AA/89D-11. School of Engineering, Air Force Institute of Technology (AU), Wright-Patterson AFB OH, December, 1989.
16. Ishikura, Capt. Dino, Brazilian Air Force. Personal communication. Air Force Institute of Technology, Wright-Patterson AFB OH, 1991.

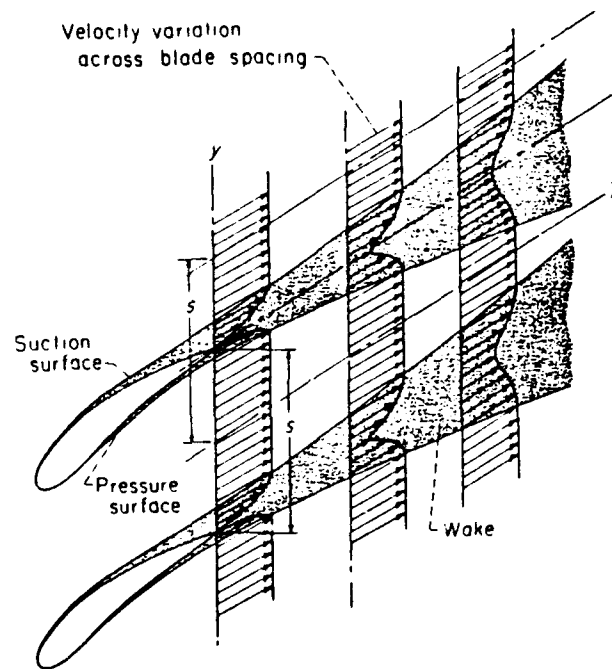


Figure 1. Development of blade wakes, Lieblein (1:201)

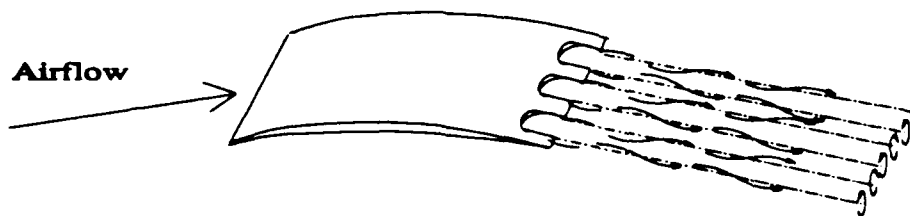


Figure 2. Crenulated compressor blade

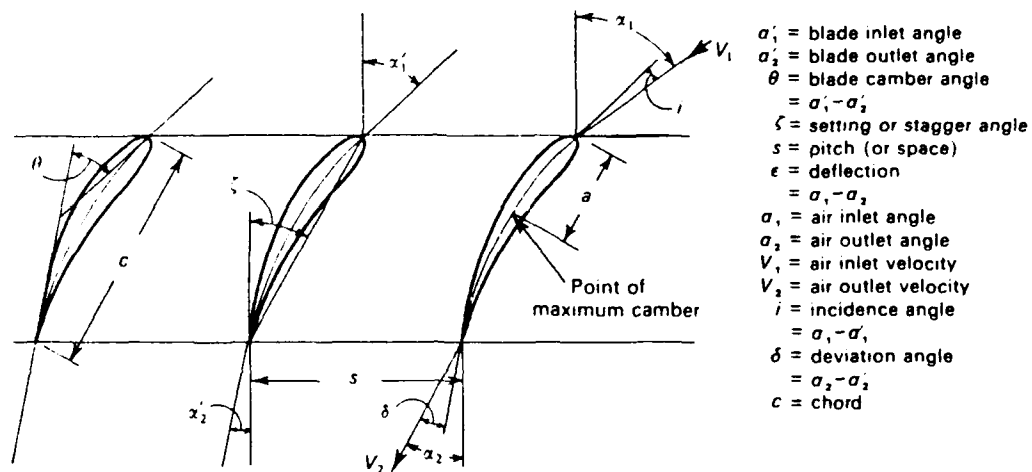


Figure 3. Cascade geometry, Cohen (4:188)

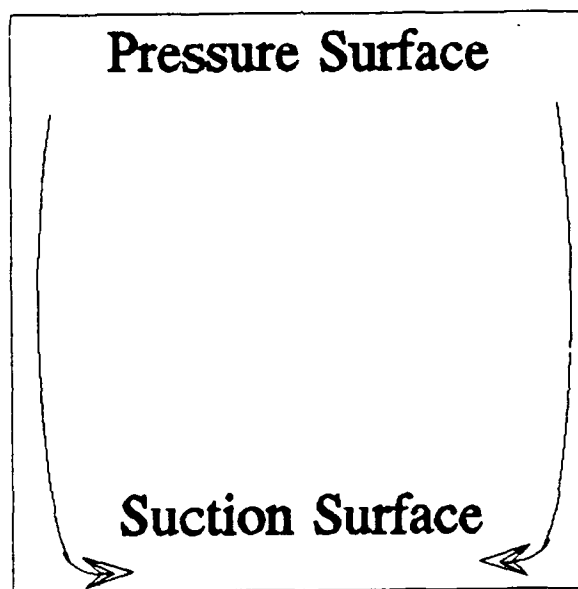


Figure 4. Secondary flow pattern in a cascade

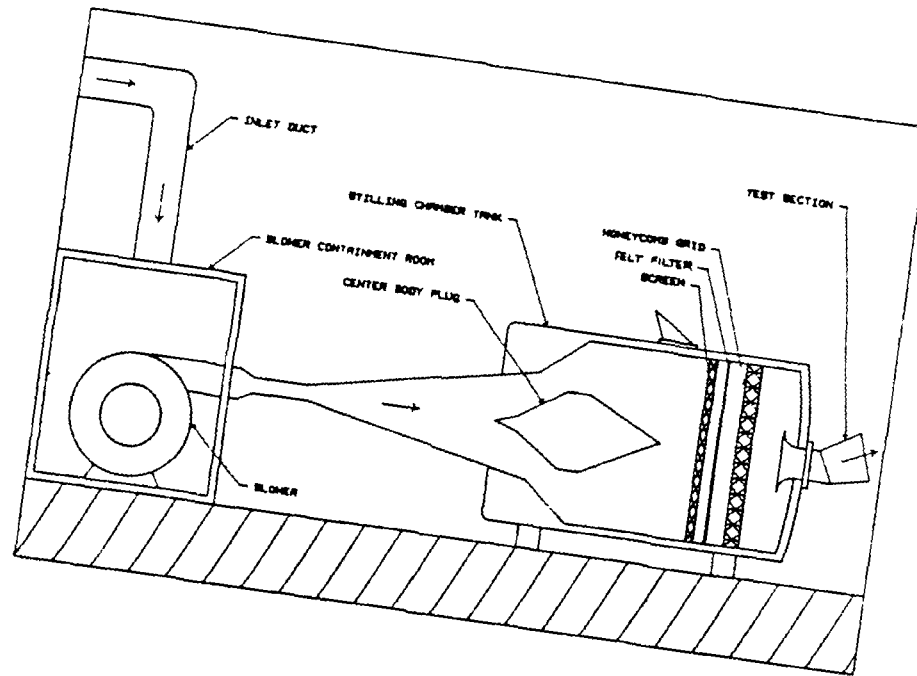


Figure 5. Cascade Test Facility

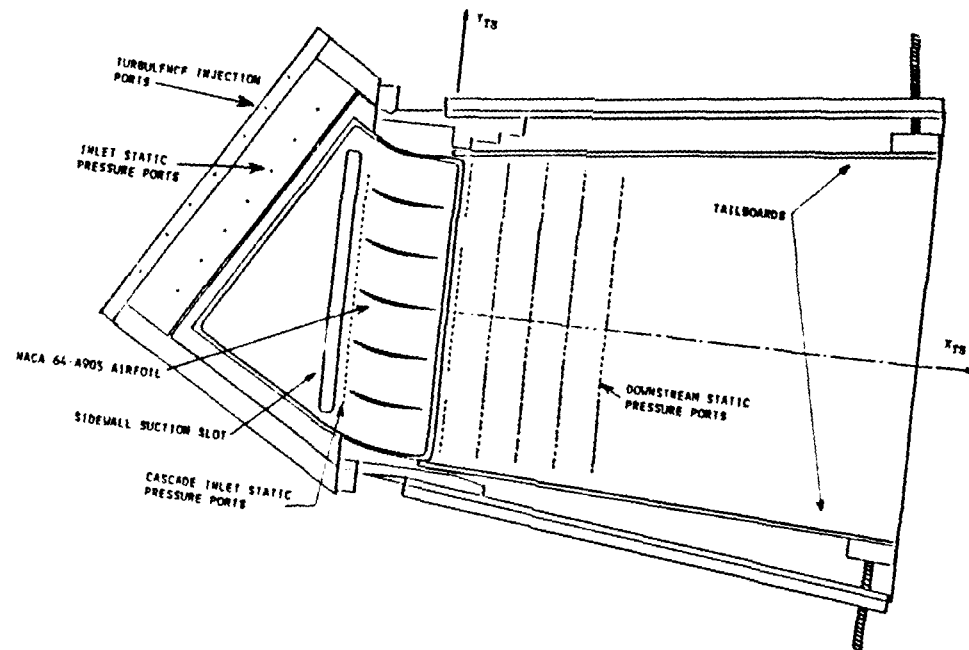


Figure 6. Test section

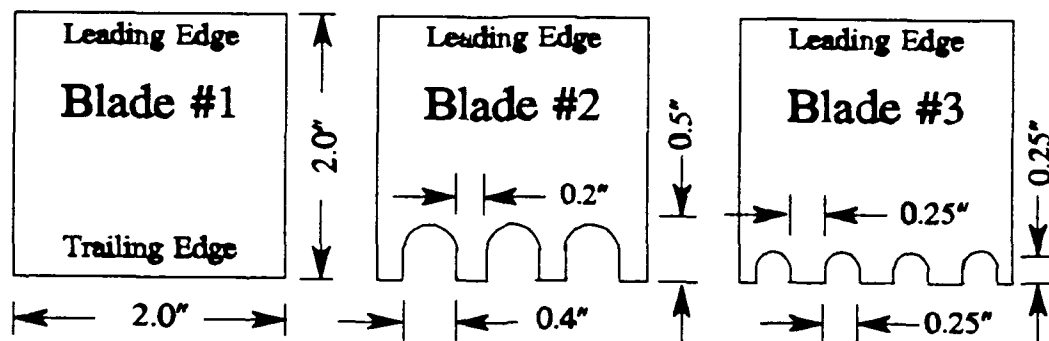


Figure 7. Crenulation dimensions

Instrumentation

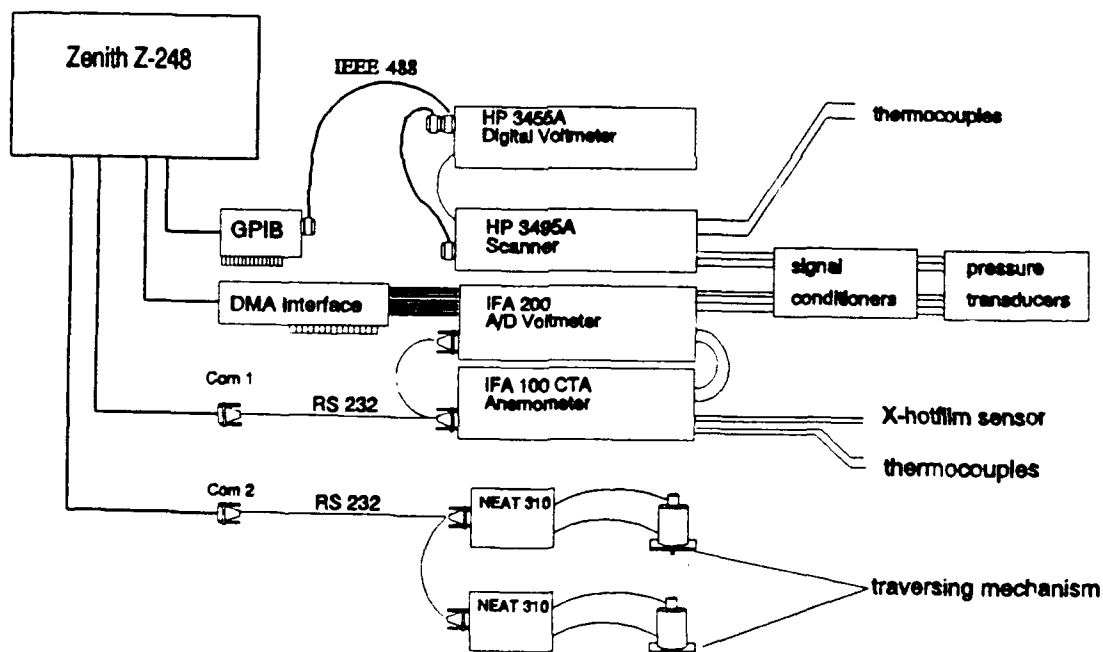


Figure 8. Instrumentation setup

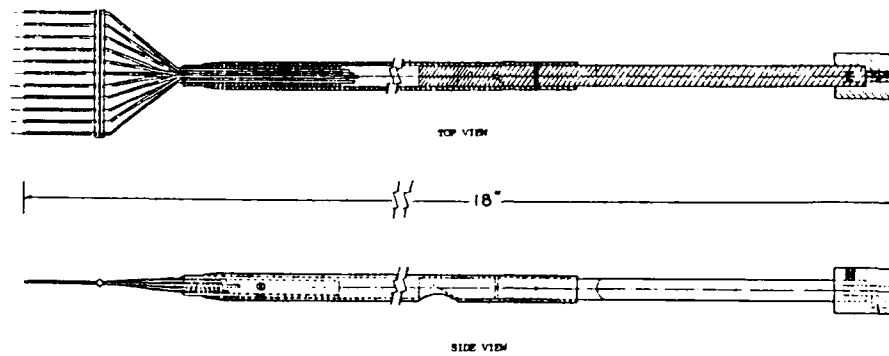


Figure 9. Total pressure rake

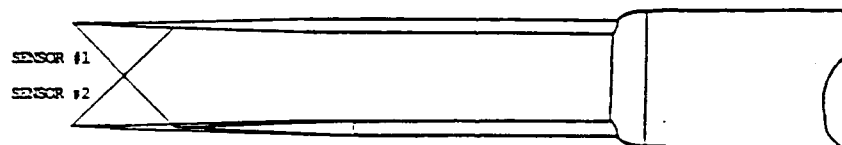


Figure 10. Hot wire sensor with "X" configuration

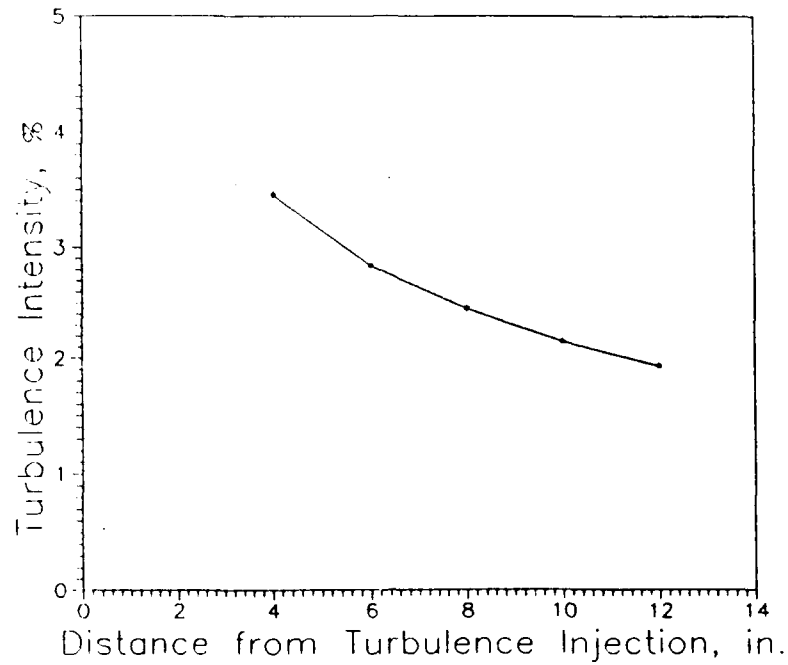


Figure 11. Turbulence intensity downstream of injection

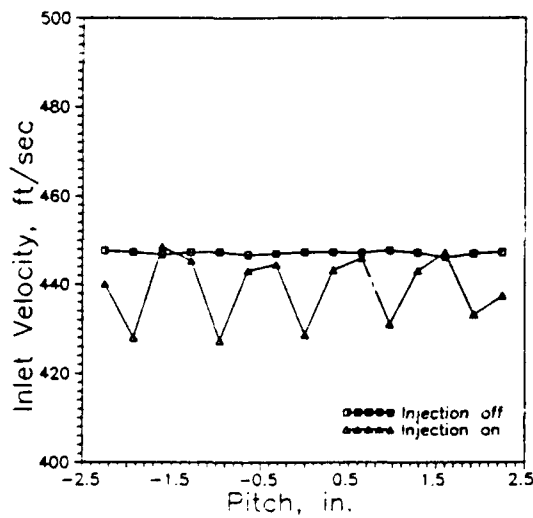


Figure 12.a. Span Averaged Velocities

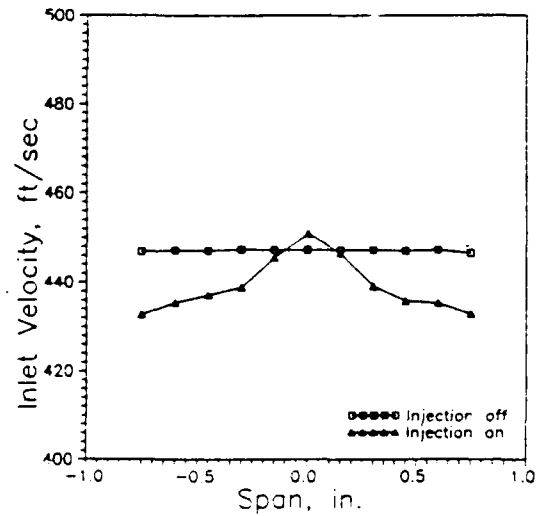


Figure 12.b. Pitch averaged velocities

Figure 12. Velocity about 5 in. downstream of turbulence injection

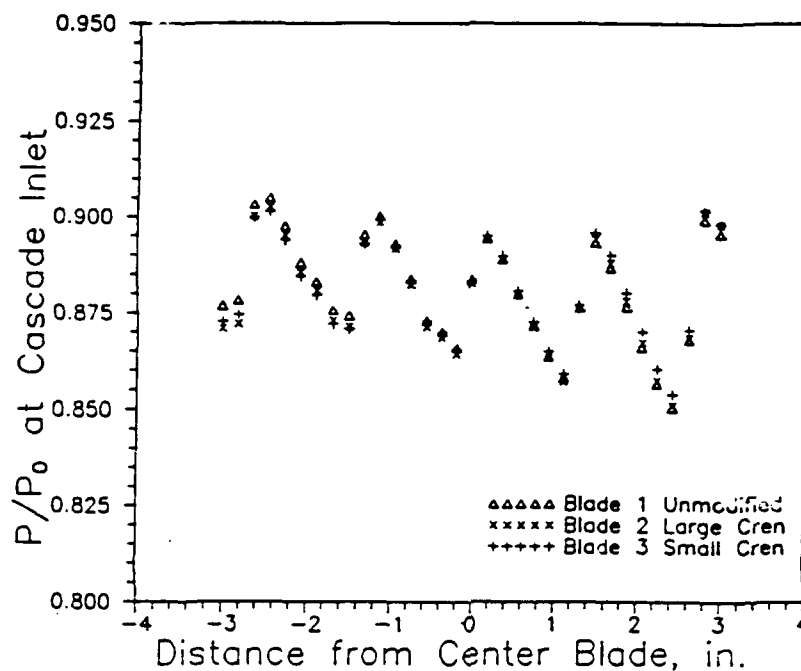


Figure 13. Pitchwise distribution of static pressures at cascade inlet, "Suction off, Turb on"

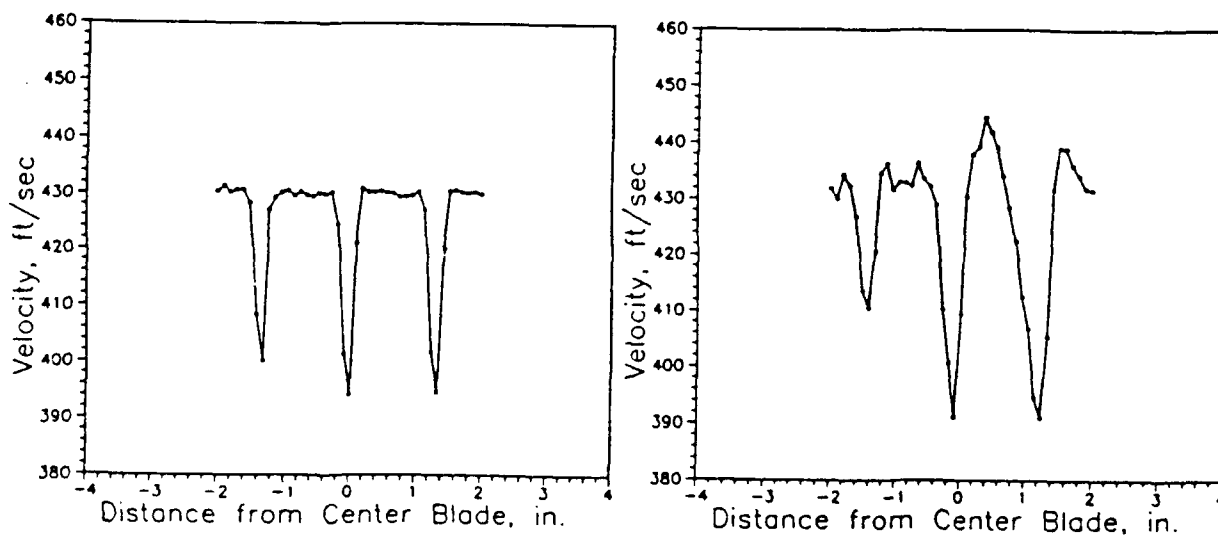


Figure 14.a. Blade 1, Turb off

Figure 14.b. Blade 1, Turb on

Figure 14. Pitchwise distribution of velocity at cascade outlet, "Suction on"

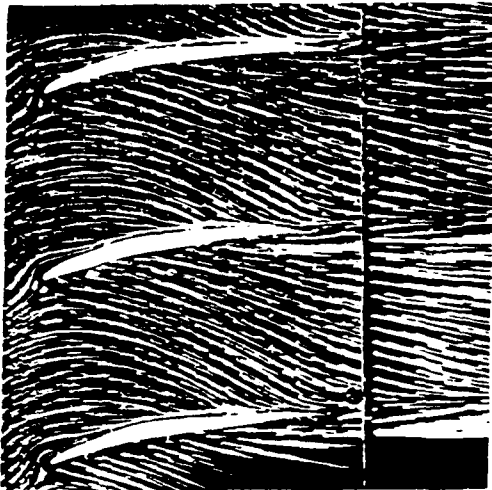


Figure 15.a. Suction on, Turb off

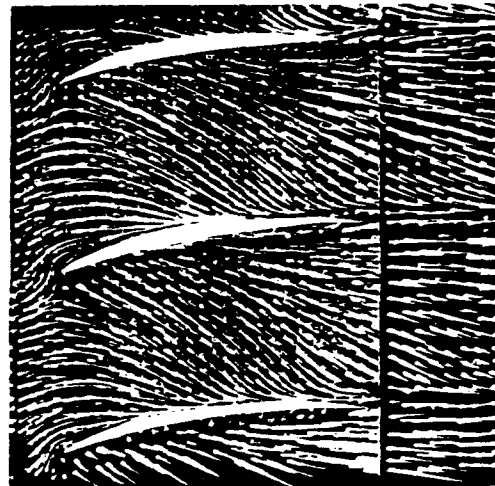


Figure 15.b. Suction off, Turb off

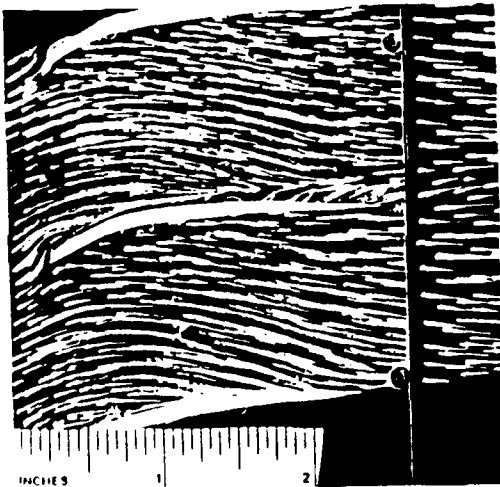


Figure 15.c. Suction on, Turb on

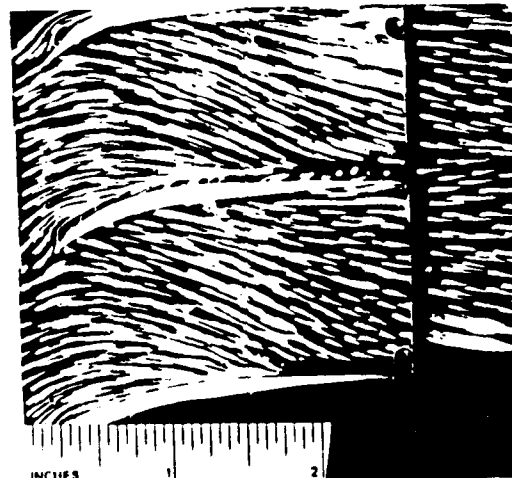


Figure 15.d. Suction off, Turb on

Figure 15. Sidewall boundary layer flow patterns

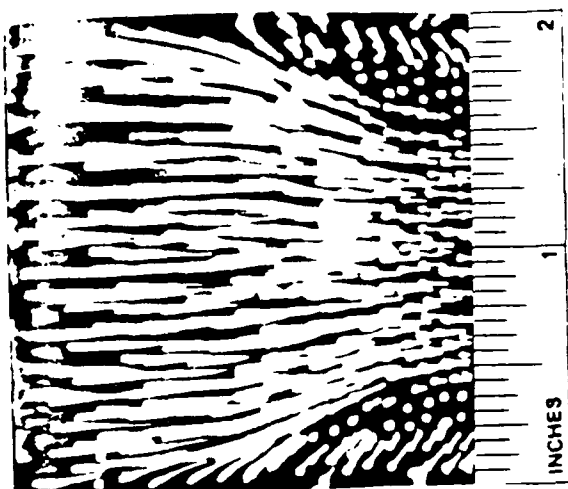


Figure 16.a. Suction on, Turb off

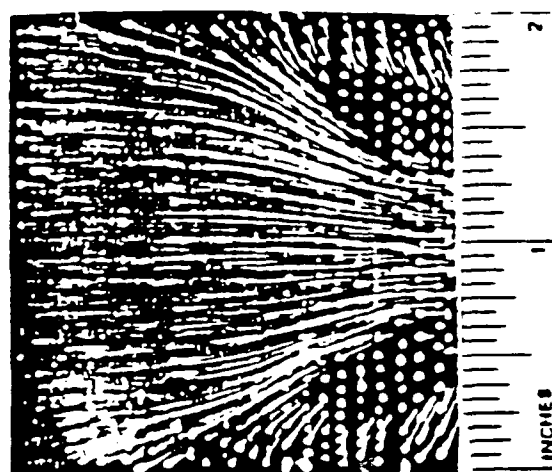


Figure 16.b. Suction off, Turb off

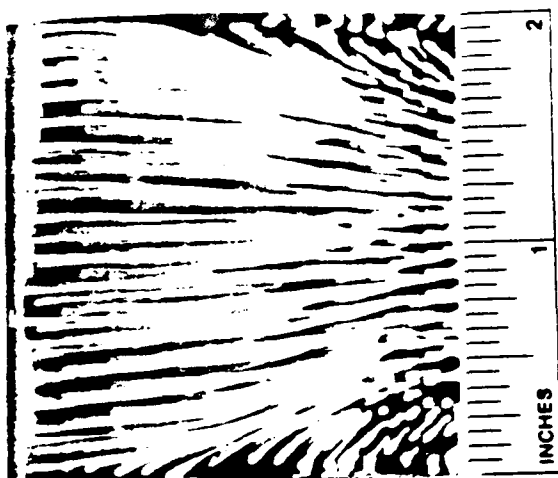


Figure 16.c. Suction on, Turb on

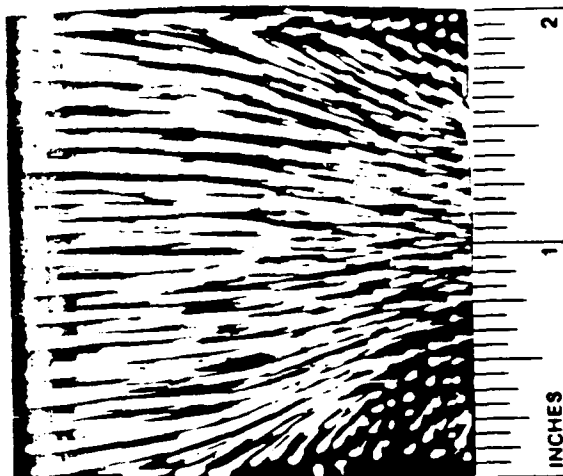


Figure 16.d. Suction off, Turb on

Figure 16. Suction surface boundary layer flow patterns

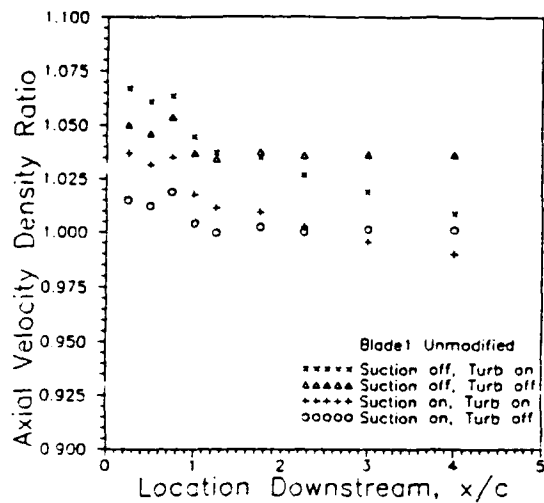


Figure 17.a.

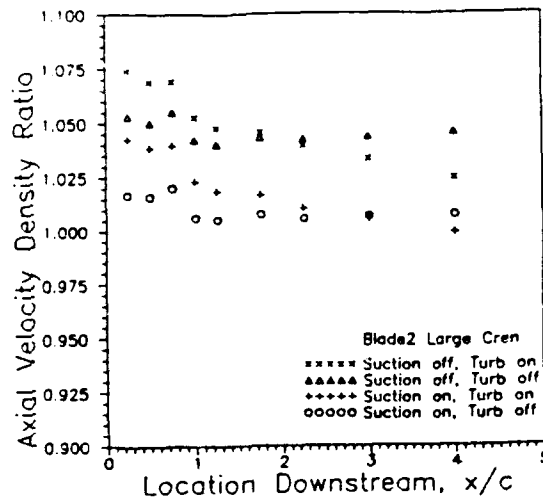


Figure 17.b.

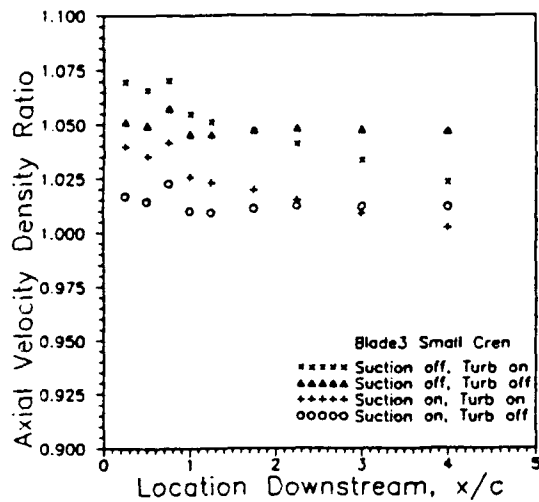


Figure 17.c.

Figure 17. Axial velocity density ratio: flow comparison

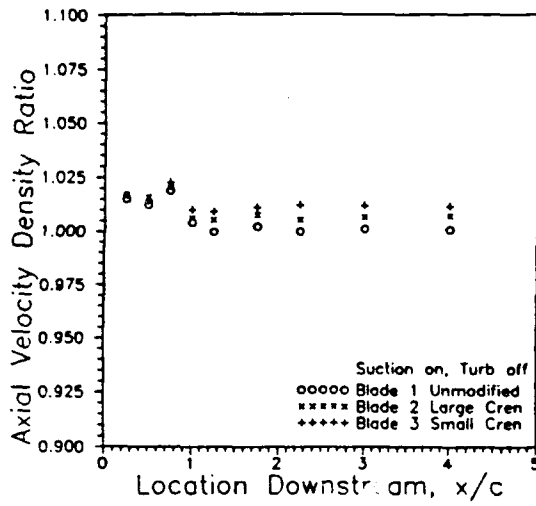


Figure 18.a.

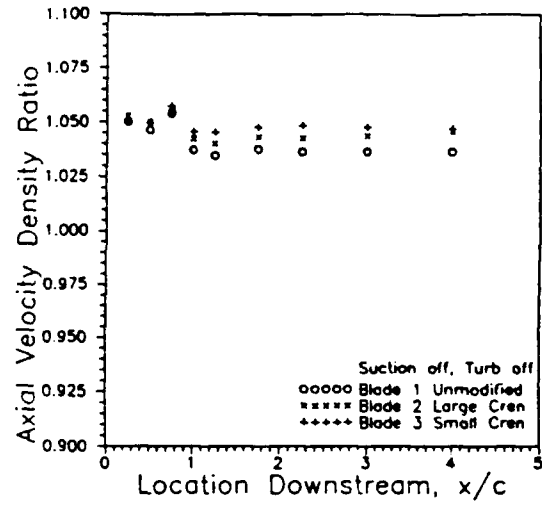


Figure 18.b.

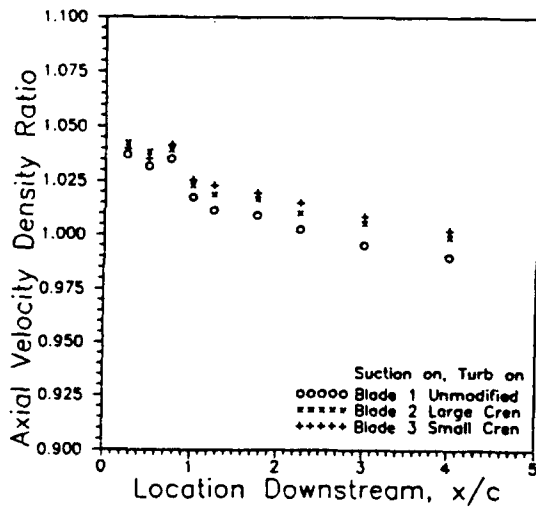


Figure 18.c.

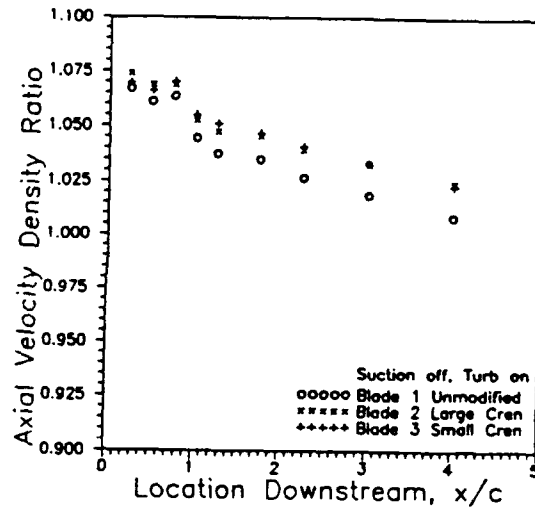


Figure 18.d.

Figure 18. Axial velocity density ratio: blade comparison

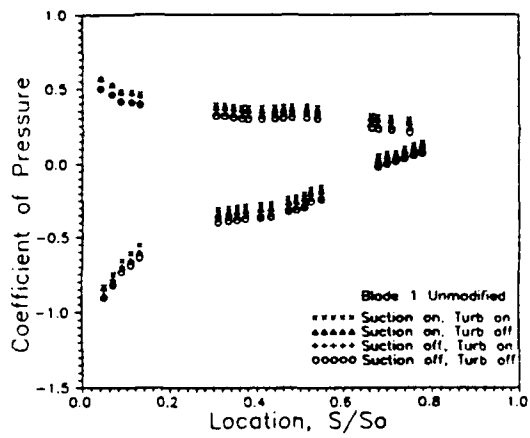


Figure 19.a.

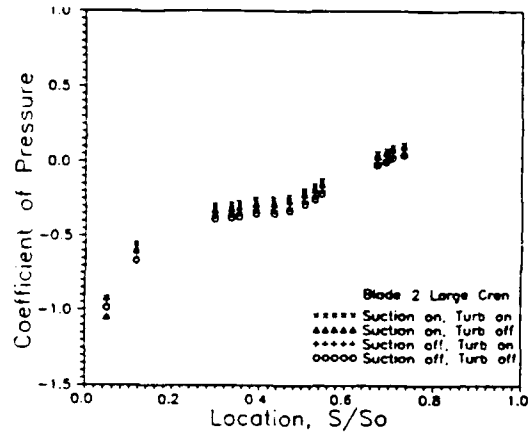


Figure 19.b.

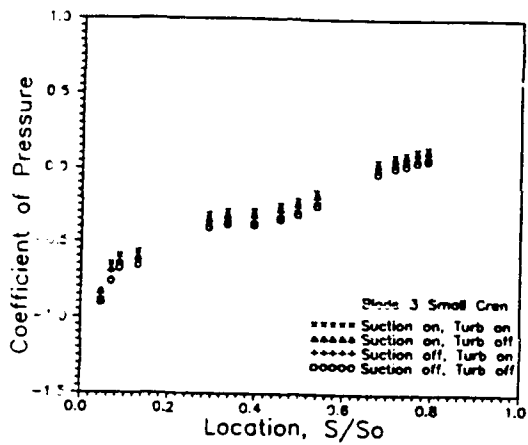


Figure 19.c.

Figure 19. Blade surface pressures: flow comparison

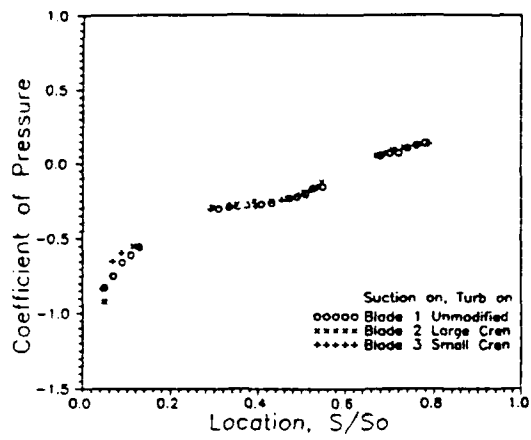


Figure 20.a.

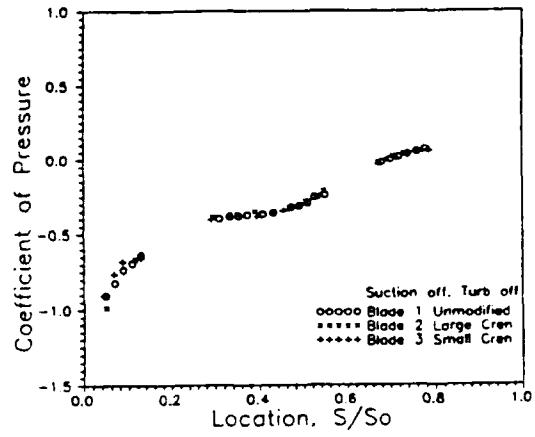


Figure 20.b.

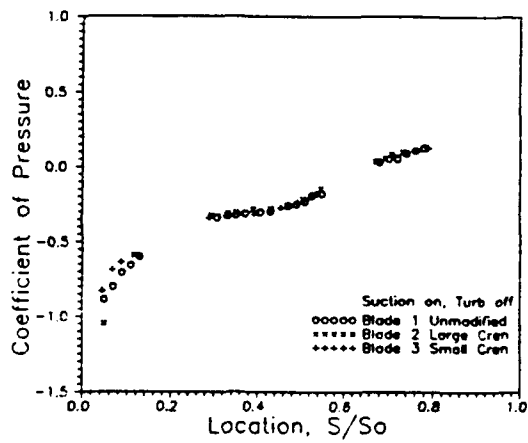


Figure 20.c.

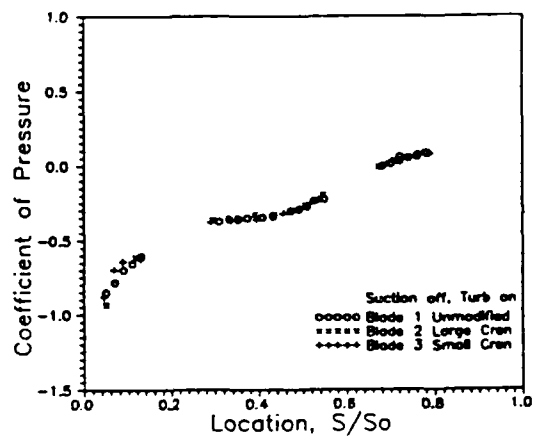


Figure 20.d.

Figure 20. Blade surface pressures: blade comparison

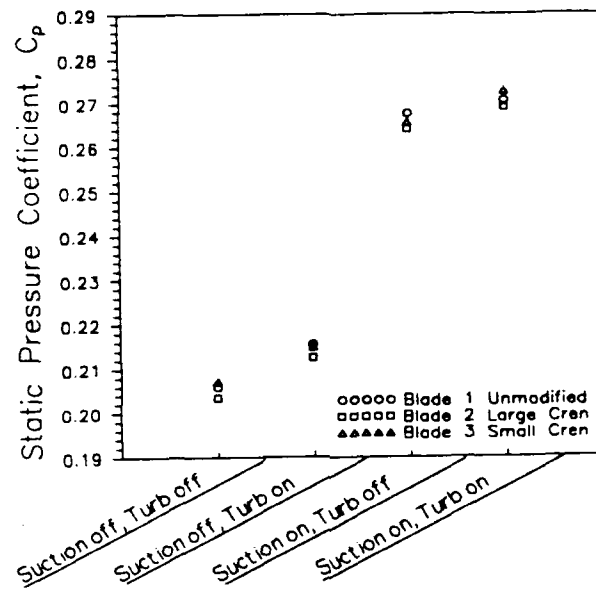


Figure 21. Static pressure rise across cascade

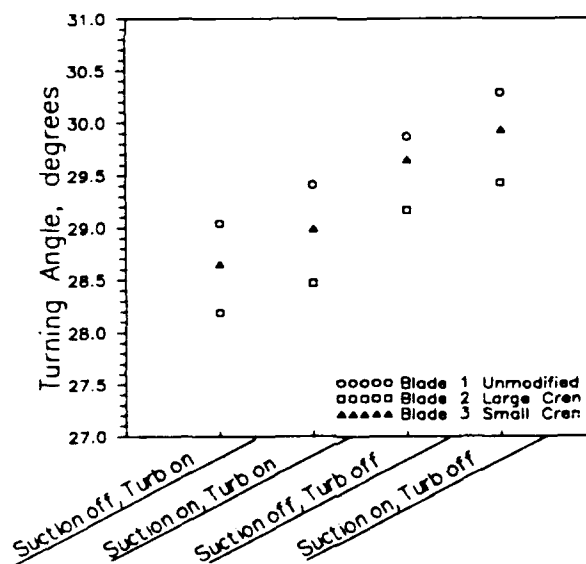


Figure 22. Flow turning angle

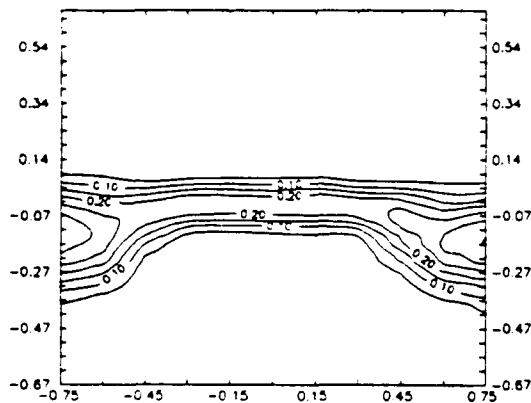


Figure 23.a. Suction on, Turb off
Blade 1, $x/c = 1$ downstream
Edge dimensions in inches

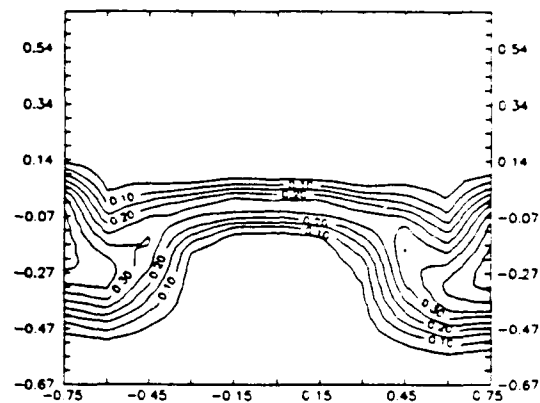


Figure 23.b. Suction off, Turb off
Blade 1, $x/c = 1$ downstream
Edge dimensions in inches

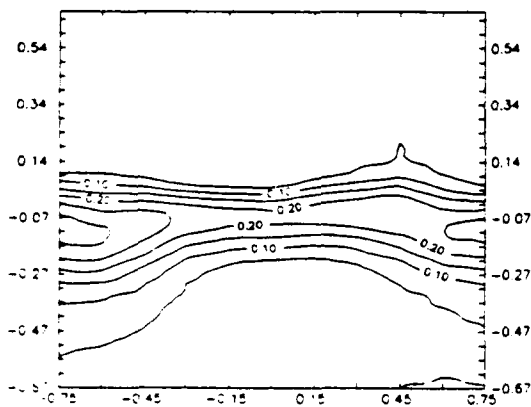


Figure 23.c. Suction on, Turb on
Blade 1, $x/c = 1$ downstream
Edge dimensions in inches

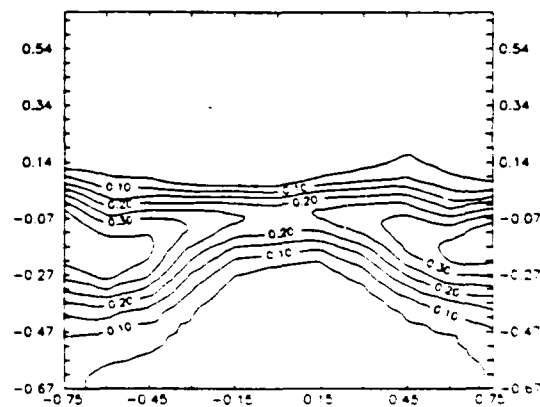


Figure 23.d. Suction off, Turb on
Blade 1, $x/c = 1$ downstream
Edge dimensions in inches

Figure 23. Pressure loss coefficient contours with unmodified blades

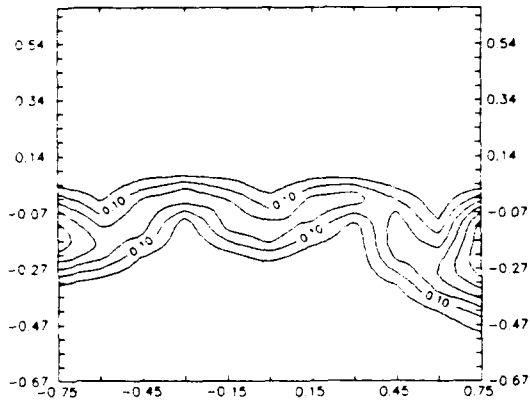


Figure 24.a. Suction on, Turb off
Blade 2, $x/c = 1$ downstream
Edge dimensions in inches

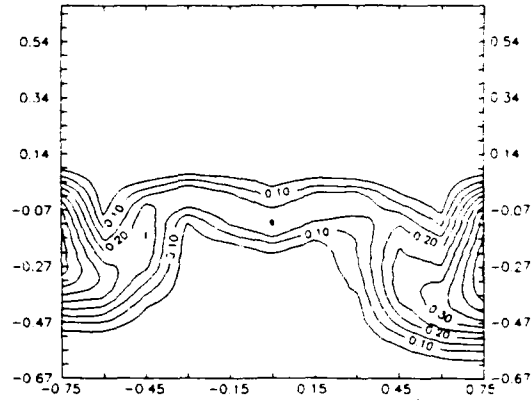


Figure 24.b. Suction off, Turb off
Blade 2, $x/c = 1$ downstream
Edge dimensions in inches

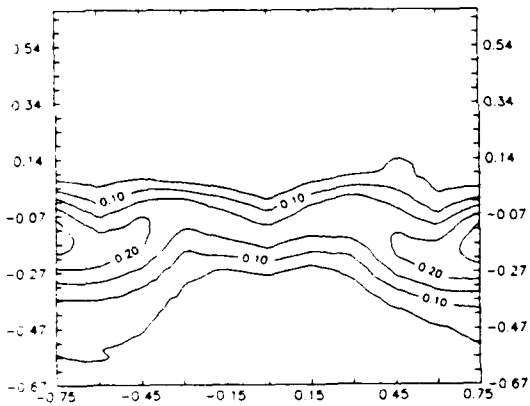


Figure 24.c. Suction on, Turb on
Blade 2, $x/c = 1$ downstream
Edge dimensions in inches

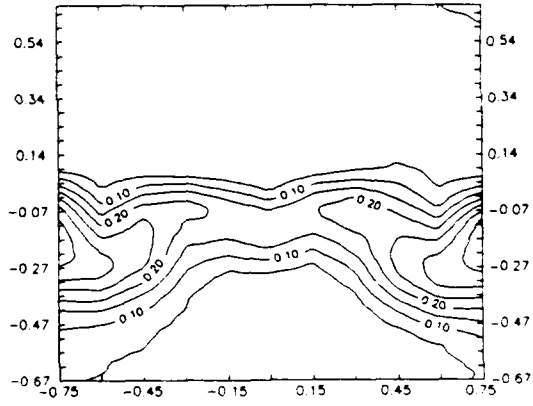
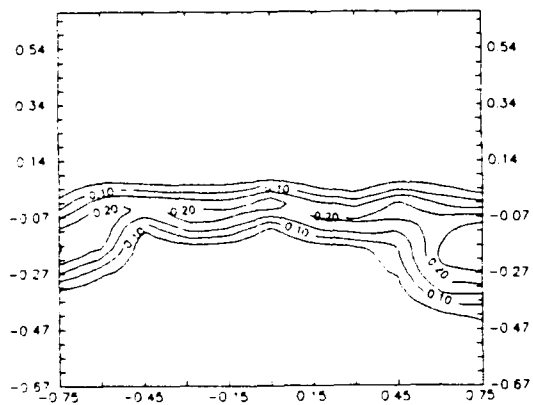
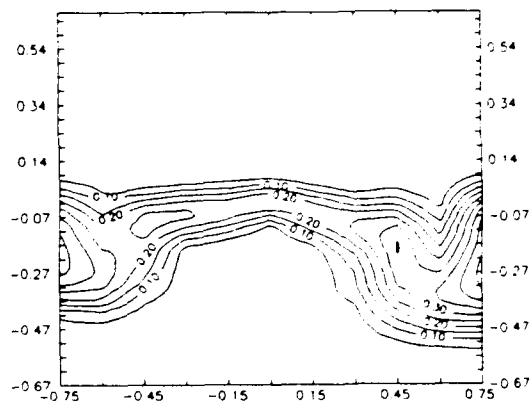


Figure 24.d. Suction off, Turb on
Blade 2, $x/c = 1$ downstream
Edge dimensions in inches

Figure 24. Pressure loss coefficient contours with large crenulations



**Figure 25.a. Suction on, Turb off
Blade 3, $x/c = 1$ downstream
Edge dimensions in inches**



**Figure 25.b. Suction off, Turb off
Blade 3, $x/c = 1$ downstream
Edge dimensions in inches**

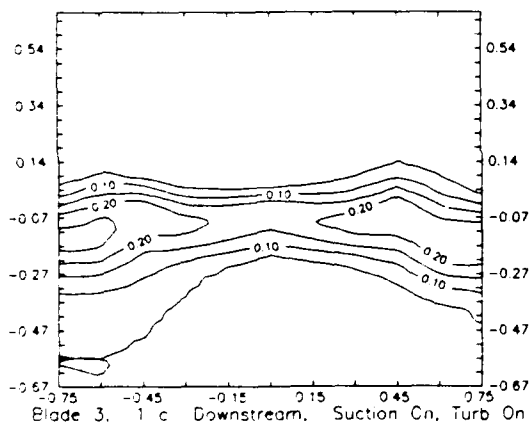


**Figure 25.c. Suction on, Turb on
Blade 3, $x/c = 1$ downstream
Edge dimensions in inches**

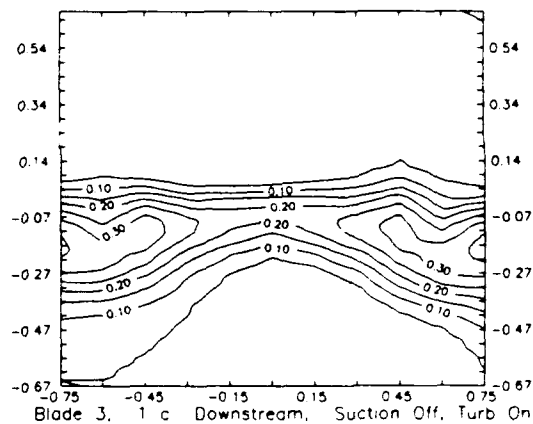


**Figure 25.d. Suction off, Turb on
Blade 3, $x/c = 1$ downstream
Edge dimensions in inches**

Figure 25. Pressure loss coefficient contours with small crenulations

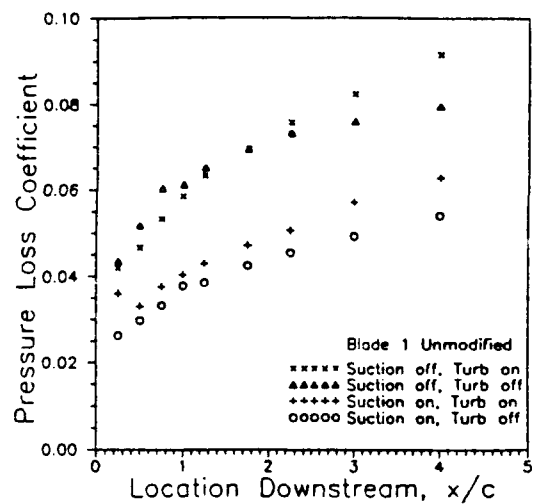


Figure 26.a.

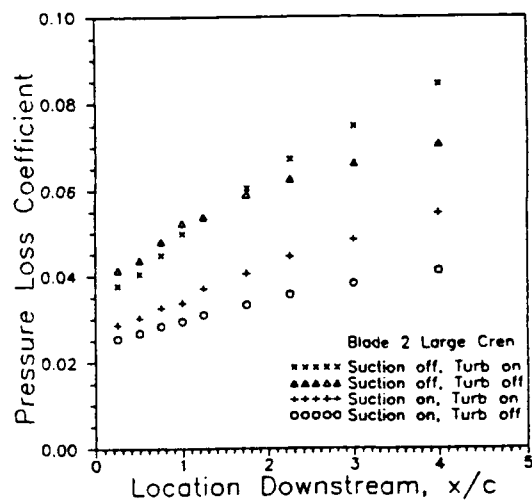


Figure 26.b.

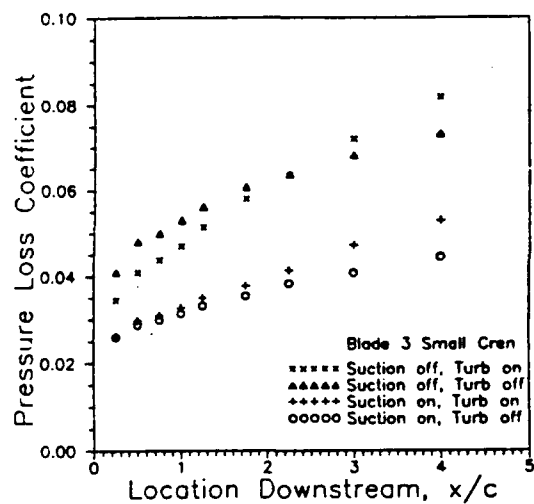


Figure 26.c.

Figure 26. Total pressure loss coefficient: flow comparison

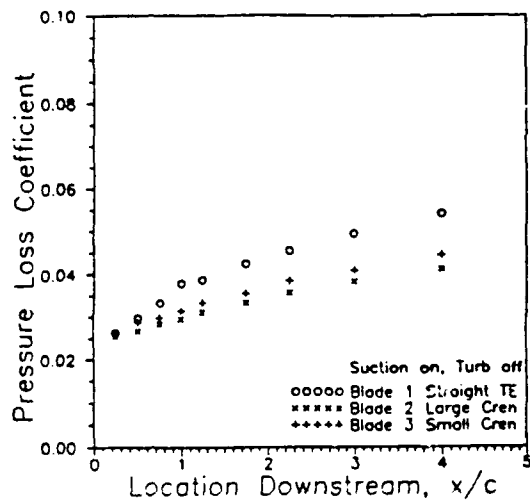


Figure 27.a.

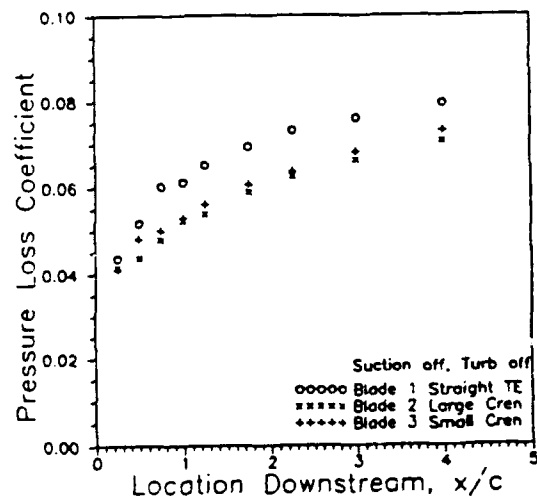


Figure 27.b.

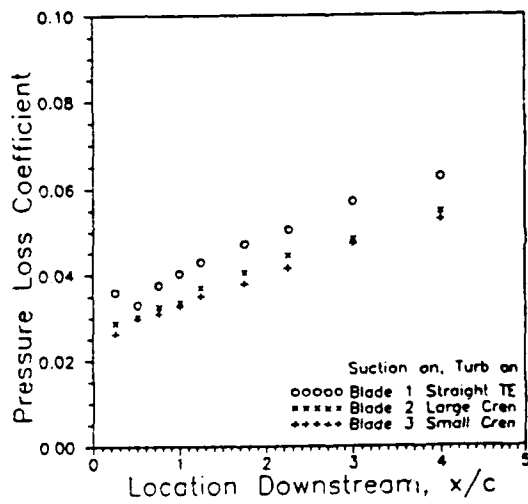


Figure 27.c.

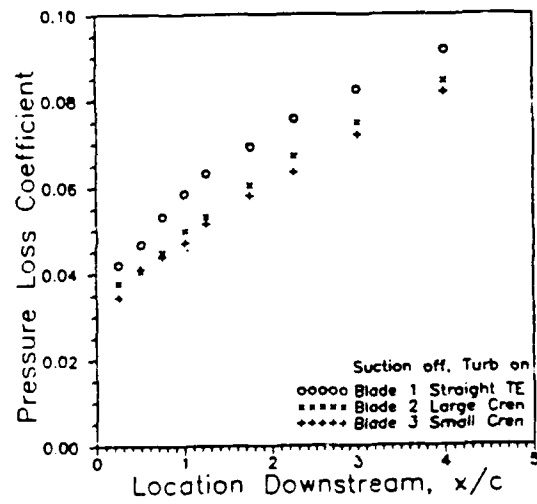


Figure 27.d.

Figure 27. Total pressure loss coefficient: blade comparison

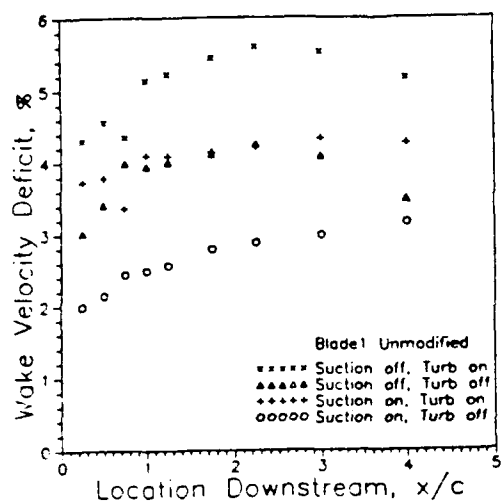


Figure 28.a.

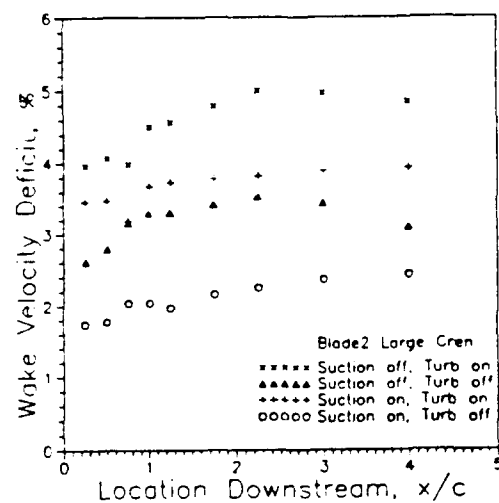


Figure 28.b.

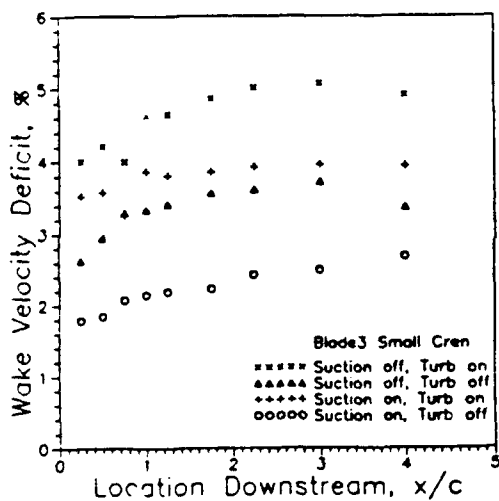


Figure 28.c.

Figure 28. Wake velocity deficit: flow comparison

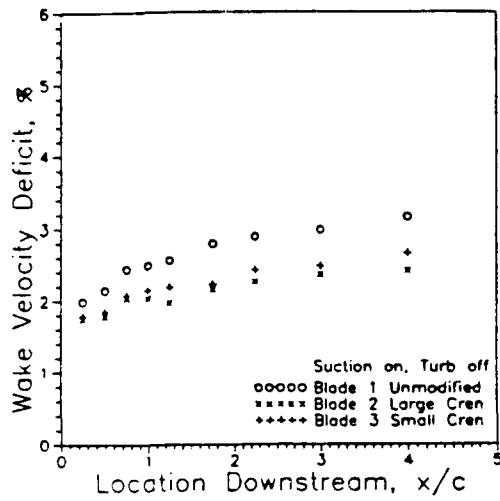


Figure 29.a.

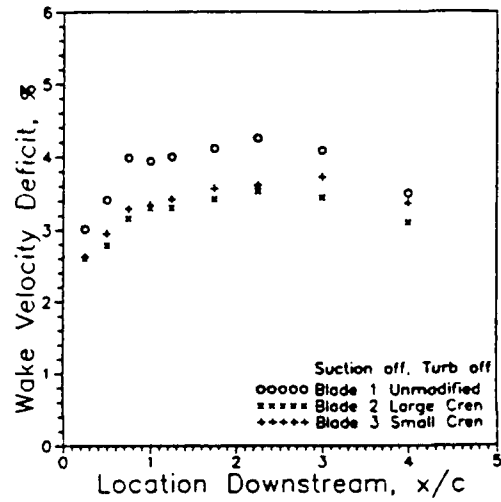


Figure 29.b.

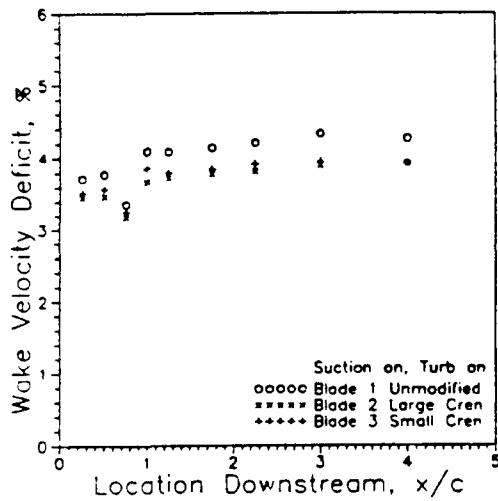


Figure 29.c.

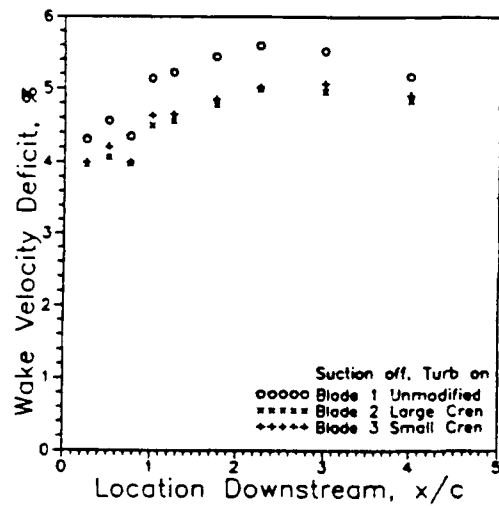


Figure 29.d.

Figure 29. Wake velocity deficit: blade comparison

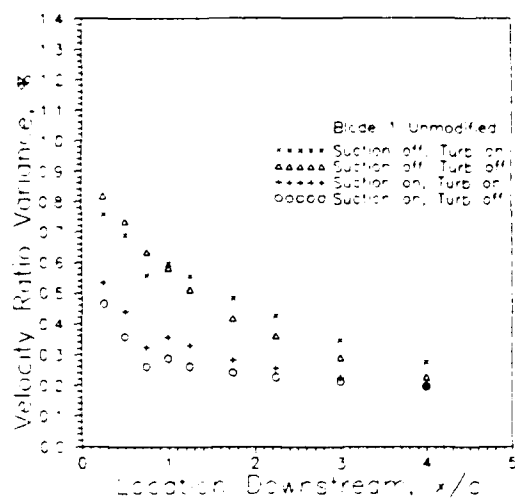


Figure 30.a.

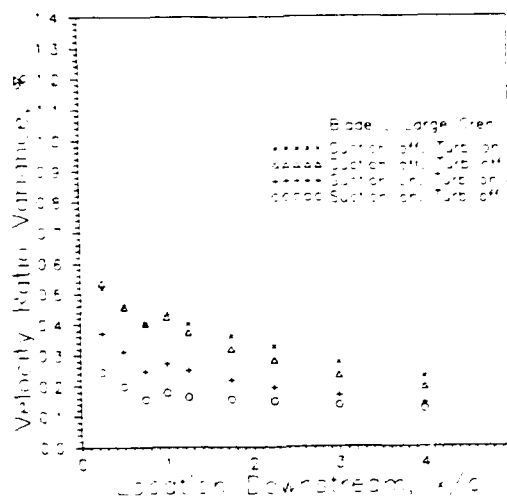


Figure 30.b.

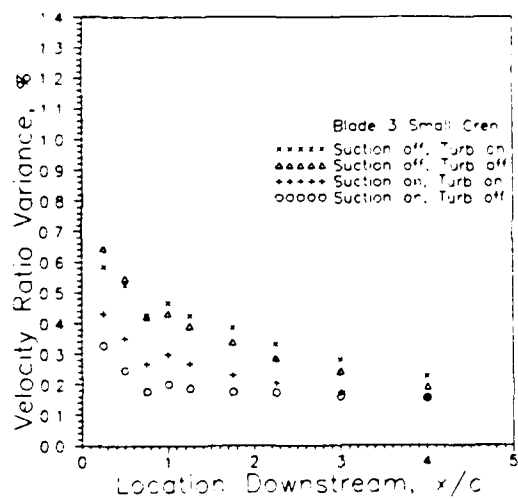


Figure 30.c.

Figure 30. Mass averaged outlet velocity variance: flow comparison

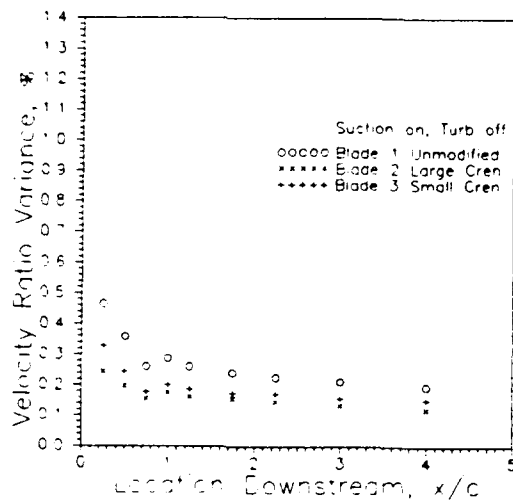


Figure 31.a.

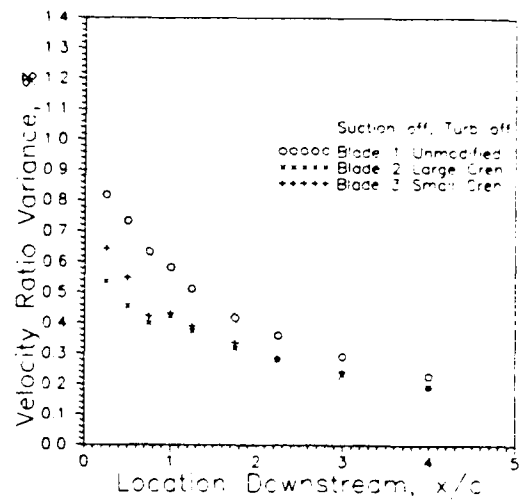


Figure 31.b.

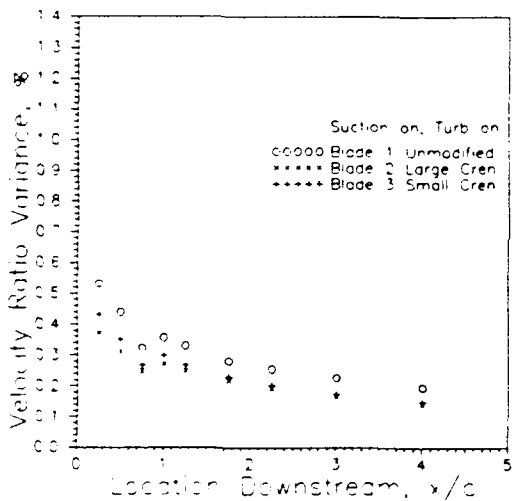


Figure 31.c.

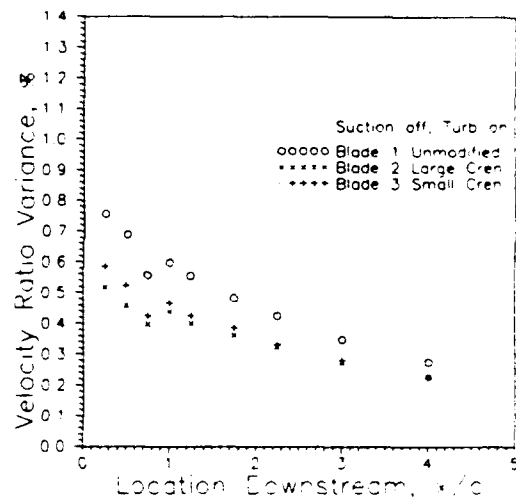


Figure 31.d.

Figure 31. Mass average outlet velocity variance: blade comparison

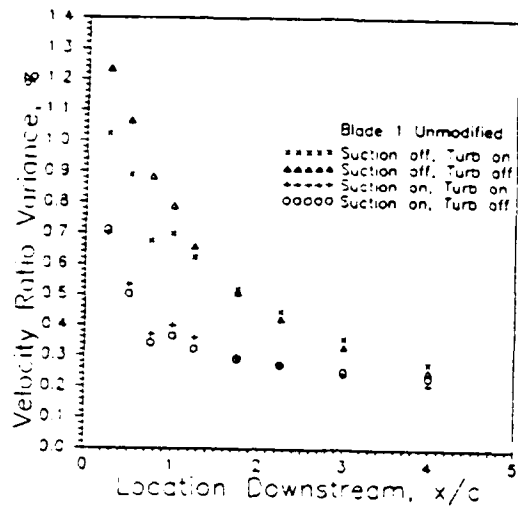


Figure 32.a.

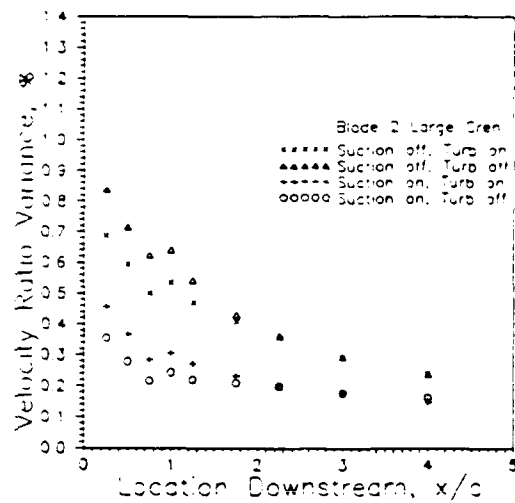


Figure 32.b.

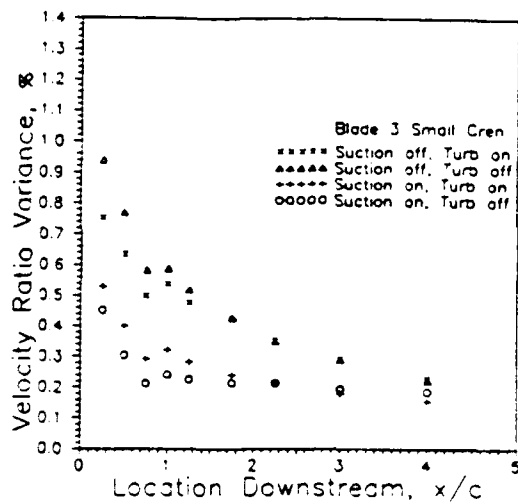


Figure 32.c.

Figure 32. Outlet velocity variance: flow comparison

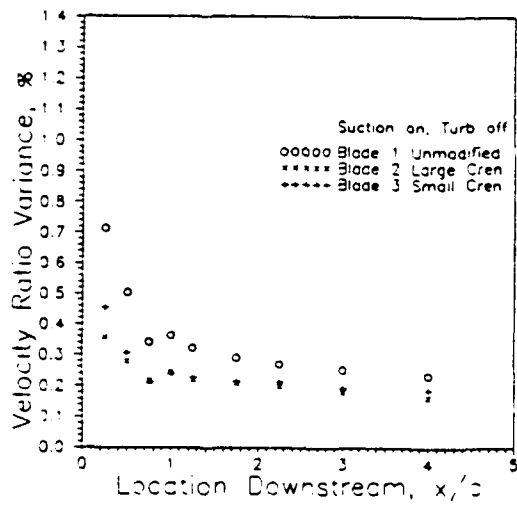


Figure 33.a.

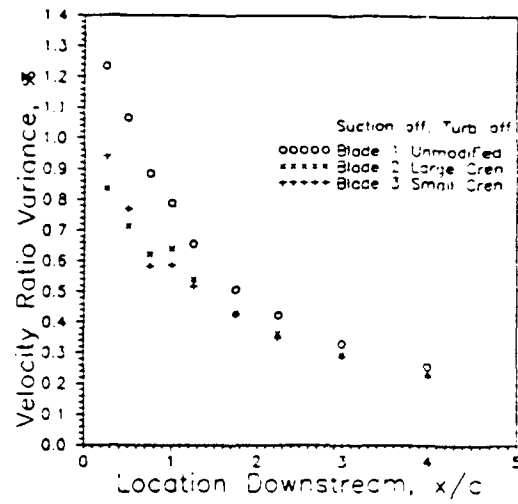


Figure 33.b.

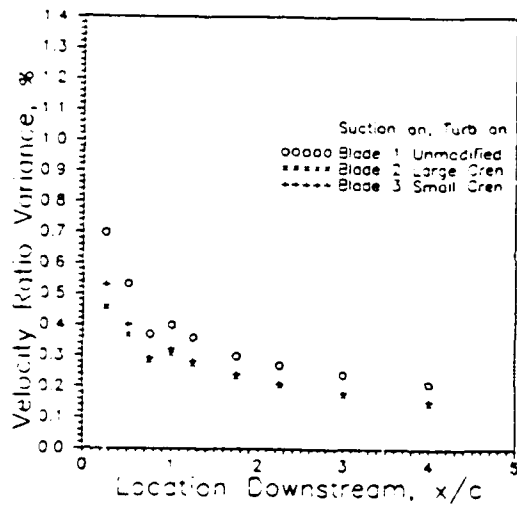


Figure 33.c.

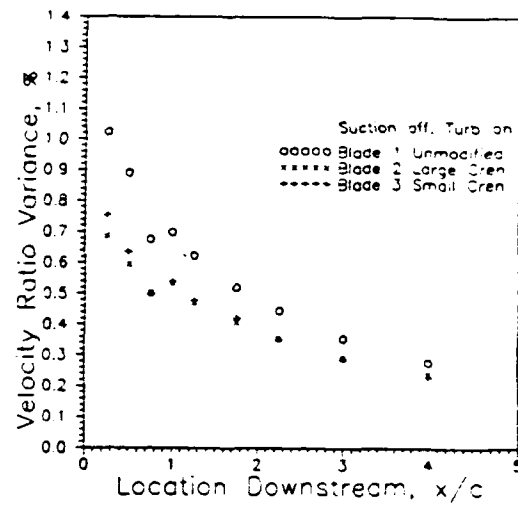


Figure 33.d.

Figure 33. Outlet velocity variance: blade comparison

Appendix A. Airfoil Geometry and Performance Estimates.

Section Data

A NACA 64-A905 $a=0.5$ airfoil was used for this study. The designator numbers, as defined in Theory of Wing Sections (11:120-121), are given below.

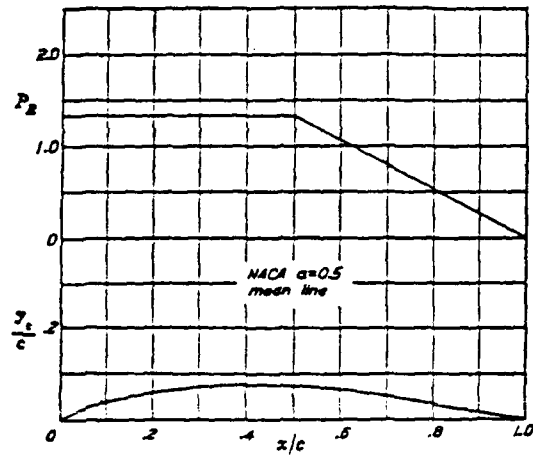
- 6 Series designator
- 4 Distance from leading edge to the point of minimum pressure for a symmetric section at zero lift, given in tenths of the chord
- A A modified thickness distribution where both surfaces are substantially straight from about $0.8c$ to the trailing edge.
- 9 Design lift coefficient, in tenths

05 Thickness in % of chord

$a=0.5$ Meanline designator. Section is designed for uniform load from the leading edge to this fraction of the chord.

The section is constructed by combining a mean line with a thickness distribution, and both are provided below. Although the thickness distribution is for a NACA 64A006 section, it may be scaled by $5/6$ to approximate the 64A005 section.

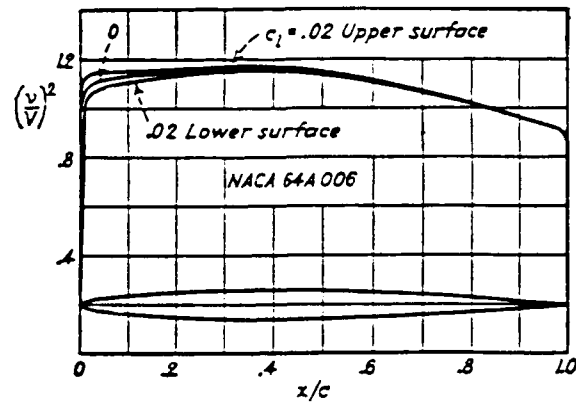
Table 7. NACA $a=0.5$ Meanline data, Abbot (11:399)



$c_h = 1.0 \quad \alpha_i = 3.04^\circ \quad c_{m,x/4} = -0.139$				
x (per cent c)	y_c (per cent c)	dy_c/dx	P_R	$\Delta p/V = P_R/4$
0	0			
0.5	0.345	0.58195		
0.75	0.485	0.53855		
1.25	0.735	0.48360		
2.5	1.295	0.40815		
5.0	2.205	0.33070		
7.5	2.970	0.28365		
10	3.630	0.24890		
15	4.740	0.19690		
20	5.620	0.15650		
25	6.310	0.12180		
30	6.840	0.09000		
35	7.215	0.05930		
40	7.430	0.02800		
45	7.490	-0.00630		
50	7.350	-0.05305		
55	6.965	-0.09785	1.200	0.300
60	6.405	-0.12550	1.067	0.267
65	5.725	-0.14570	0.933	0.233
70	4.955	-0.16015	0.800	0.200
75	4.130	-0.16980	0.667	0.167
80	3.265	-0.17435	0.533	0.133
85	2.395	-0.17415	0.400	0.100
90	1.535	-0.16850	0.267	0.067
95	0.720	-0.15565	0.133	0.033
100	0	-0.12660	0	0

Data for NACA Mean Line $a = 0.5$

Table 8. NACA 64A006 Thickness form, Abbot (11:354)



x (per cent c)	y (per cent c)	$(v/V)^2$	v/V	$\Delta u_a/V$
0	0	0	0	4.688
0.5	0.485	1.019	1.009	2.101
0.75	0.585	1.046	1.023	1.798
1.25	0.739	1.076	1.037	1.422
2.5	1.016	1.106	1.052	0.980
5.0	1.399	1.118	1.057	0.694
7.5	1.684	1.126	1.061	0.564
10	1.919	1.132	1.064	0.482
15	2.283	1.141	1.068	0.382
20	2.557	1.149	1.072	0.321
25	2.757	1.154	1.074	0.278
30	2.896	1.158	1.076	0.246
35	2.977	1.162	1.078	0.219
40	2.999	1.165	1.079	0.197
45	2.945	1.158	1.075	0.177
50	2.825	1.142	1.069	0.159
55	2.653	1.125	1.061	0.143
60	2.438	1.107	1.052	0.126
65	2.188	1.087	1.043	0.112
70	1.907	1.066	1.032	0.099
75	1.602	1.043	1.021	0.087
80	1.285	1.018	1.009	0.074
85	0.967	0.992	0.996	0.061
90	0.649	0.964	0.982	0.047
95	0.331	0.935	0.967	0.033
100	0.013	0	0	0

L.E. radius: 0.246 per cent c
T.E. radius: 0.014 per cent c

NACA 64A006 Basic Thickness Form

Blade Angles

The blade inlet angle, blade outlet angle, and camber angle of a section are defined by tangents to the mean line at the leading edge and at the trailing edge. However, for NACA sections with the $a=0.5$ meanline, the meanline has an infinite slope at the leading edge. For these blades the tangent to the meanline at the leading edge is usually measured at $x/c = 0.005$, but Lieblein (1) found an alternate method for determining the angles that gave better correlations with circular arc airfoils. A circular arc passed through the leading edge, trailing edge, and point of maximum camber (shifted to $0.5c$) is an equivalent circular arc meanline. From this meanline an equivalent camber angle and an equivalent blade inlet angle can be calculated.

For the NACA 64-A905 $a=0.5$ section the tangent to the meanline at the trailing edge also needs to be addressed. As specified earlier, the A in the designator specifies a blade modification where both surfaces of the airfoil are essentially straight from $0.8c$ to the trailing edge. The tangent to the meanline at the trailing edge can then be evaluated by the slope between the meanline coordinates at $0.8c$ and $1.0c$, given on the previous page. $\text{Atan}((3.265 - 0) / (80 - 100)) = -9.27^\circ$. Combined with the stagger angle of 7.75° the blade outlet angle becomes -1.52° .

Returning to the leading edge problem, the tangent to the mean line at $0.005c$ gives a camber angle of 39.4° , a blade inlet angle of 37.95° , and an incidence angle of -6.95° . The equivalent camber angle, from the equivalent circular arc meanline, is 34.08° . The equivalent blade inlet angle is 32.56° , and the equivalent incidence angle is -1.56° . The equivalent angles are used in this study.

Momentum Analysis of Flow Through a Cascade

Given two-dimensional, incompressible flow through a cascade, lift and drag can be calculated by application of continuity, the Bernoulli equation, and the momentum equation, as shown by Horlock (5:33,34). The development is based on the control volume illustrated in Figure 34.

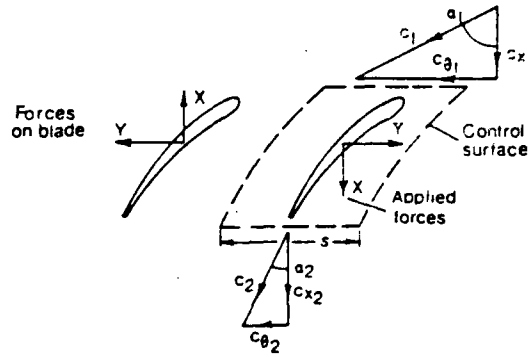


Figure 34. Control surface around blade in cascade, Horlock (5:33)

Continuity equates the inlet and outlet axial velocities, which are then identified as V_x . A mean angle and mean velocity through the passage can be defined by

$$\tan \alpha_m = \frac{1}{2}(\tan \alpha_1 + \tan \alpha_2) \quad (24)$$

$$V_m = V_x \sec \alpha_m \quad (25)$$

Lift is defined as the force perpendicular to the mean velocity and drag is defined as the force parallel to the mean velocity. They are calculated in terms of the axial and tangential forces, X and Y , and the mean flow angle α_m :

$$L = X \sin \alpha_m + Y \cos \alpha_m \quad (26)$$

$$D = Y \sin \alpha_m - X \cos \alpha_m \quad (27)$$

The axial and tangential forces are calculated by

$$X = (P_2 - P_1)s = \left((P_{02} - P_{01}) - \frac{1}{2} \rho (V_2^2 - V_1^2) \right) s \quad (28)$$

$$X = \frac{1}{2} \rho V_x^2 (\tan^2 \alpha_1 - \tan^2 \alpha_2) s - (P_{01} - P_{02}) s \quad (29)$$

$$X = \rho V_x^2 (\tan \alpha_1 - \tan \alpha_2) s \tan \alpha_m - (P_{01} - P_{02}) s \quad (30)$$

and

$$Y = \rho V_x (V_{y_1} - V_{y_2}) s \quad (31)$$

$$Y = \rho V_x^2 (\tan \alpha_1 - \tan \alpha_2) s \quad (32)$$

Lift and drag then become

$$\begin{aligned} L = & \rho V_x^2 (\tan \alpha_1 - \tan \alpha_2) s \tan \alpha_m \sin \alpha_m - (P_{01} - P_{02}) s \sin \alpha_m \\ & + \rho V_x^2 (\tan \alpha_1 - \tan \alpha_2) s \cos \alpha_m \end{aligned} \quad (33)$$

$$L = \rho V_x^2 (\tan \alpha_1 - \tan \alpha_2) s \left(\frac{1 - \cos^2 \alpha_m}{\cos \alpha_m} + \cos \alpha_m \right) - (P_{01} - P_{02}) s \sin \alpha_m \quad (34)$$

$$L = \rho V_x^2 (\tan \alpha_1 - \tan \alpha_2) s \sec \alpha_m - (P_{01} - P_{02}) s \sin \alpha_m \quad (35)$$

and

$$\begin{aligned} D = & \rho V_x^2 (\tan \alpha_1 - \tan \alpha_2) s \sin \alpha_m - \rho V_x^2 (\tan \alpha_1 - \tan \alpha_2) s \tan \alpha_m \cos \alpha_m \\ & + (P_{01} - P_{02}) s \cos \alpha_m \end{aligned} \quad (36)$$

$$D = \rho V_x^2 (\tan \alpha_1 - \tan \alpha_2) s (\sin \alpha_m - \sin \alpha_m) + (P_{01} - P_{02}) s \cos \alpha_m \quad (37)$$

$$D = (P_{01} - P_{02}) s \cos \alpha_m \quad (38)$$

Estimates of Turning Angle and Pressure Loss

Howell's correlation (5:56-60) and Lieblein's correlation (1) can be used to estimate turning angle and total pressure loss in low speed cascades. Values from intermediate calculations are given below. The referenced texts should be consulted for additional detail.

In Howell's correlation, "nominal" values are calculated which correspond to the cascade turning a flow 80% of its maximum "stalling" turning angle. Nominal values are identified by "**". Turning angle and pressure rise can then be calculated in a small range of incidence angles around the nominal incidence angle. The nominal deviation angle is calculated by Carter's rule

$$\alpha_2^* = \alpha_2' + \delta^* = \alpha_2' + m \theta \sqrt{s/l} \quad (39)$$

$$m = .23 \left(2 \cdot \frac{a}{l} \right)^2 + .1 \left(\frac{\alpha_2'}{50} \right) \quad (40)$$

$$\alpha_2^* = \frac{\alpha_2' + .23(2a/l)^2 \theta \sqrt{s/l}}{1 - .002 \theta \sqrt{s/l}} \quad (41)$$

where

$$\theta = \text{camber angle} = 34.08^\circ$$

$$s/l = 1/\text{solidity} = 1/1.5 = 0.667$$

$$a/l = \text{point of maximum camber on airfoil from leading edge / chord} \\ = 0.45$$

$$\alpha_2' = -1.52^\circ \Rightarrow \alpha_2^* = 3.88^\circ \Rightarrow \delta^* = 5.40^\circ$$

Given α_2^* and the Reynolds number ($4 \cdot 10^5$), the nominal deflection angle, ϵ^* , is derived from three graphs.

$$\epsilon^*/\phi\psi = 32.5^\circ \quad \phi = 1.03 \quad \psi = 1.15 \quad \Rightarrow \quad \epsilon^* = 27.43^\circ$$

The nominal incidence angle is calculated by

$$i^* = \alpha_1^* - \alpha_1' = \alpha_2^* + \epsilon^* - \alpha_1' \quad (42)$$

Estimates of turning angle and pressure loss are then obtained from a graph, based on the difference between the incidence angle and the nominal incidence angle.

$$i^* = 3.88^\circ + 27.43^\circ - 32.56^\circ = -1.25^\circ$$

$$i = -1.56^\circ$$

$$(i - i^*)/\epsilon^* = 0.01$$

$$\epsilon = 0.99\epsilon^* = 27.16^\circ$$

$$\delta = \alpha_2 - \alpha_2' = \alpha_1 - \epsilon - \alpha_2' = 31^\circ - 27.16^\circ - (-1.52^\circ)$$

$$\delta = 5.36^\circ$$

$$C_D = \text{coefficient of drag} = 0.017 \pm 0.001$$

In Lieblein's correlation, "reference" angles are calculated. The reference incidence angle is midway between the two incidence angles at which the loss in total pressure is twice its minimum. This is not necessarily the minimum pressure loss incidence angle, but it is in the middle of the pressure loss "bucket". Again, deviation angle and pressure loss can be calculated in a small range of incidence angles around the reference incidence angle.

$$i_r = i_0 + n\varphi = \text{reference incidence angle}$$

$$i_0 = (K_s)_s(K_t)_t(i_0)_{10} = \text{zero camber reference incidence angle}$$

$$(K_s)_s = \text{shape factor} = \text{adjustment for thickness distributions different than for 65 series sections}$$

$$= 1.0$$

$$(K_t)_t = \text{thickness factor} = \text{adjustment for maximum thickness other than 10\%, read from graph}$$

$$= 0.685$$

$(i_0)_{10}$ = incidence for zero camber, 10% thick, 65 series airfoil with a given air inlet angle and solidity, read from graph

$$= 3.65^\circ$$

$$i_0 = 2.50^\circ$$

n = variation of reference incidence angle with camber angle, read from graph

$$= -0.055$$

φ = camber angle = 34.08°

$$i_r = 0.63^\circ$$

$\delta_r = \delta_0 + m\varphi$ = reference deviation angle

$\delta_0 = (K_\delta)_s(K_\delta)_t(\delta_0)_{10}$ = zero camber reference deviation angle

$(K_\delta)_s$ = shape factor = adjustment for thickness distributions different than for 65 series sections

$$= 1.0$$

$(K_\delta)_t$ = thickness factor = adjustment for maximum thickness other than 10%, read from graph

$$= 0.425$$

$(\delta_0)_{10}$ = deviation for zero camber, 10% thick, 65 series airfoil with a given air inlet angle and solidity, read from graph

$$= 0.70^\circ$$

$$\delta_0 = 0.2975^\circ$$

m = variation of reference deviation angle with camber angle, read from graph

$$= 0.132$$

φ = camber angle = 34.08°

$$\delta_r = 4.79^\circ$$

$\delta^\circ = \delta_r + (i - i_r)(d\delta^\circ/di)_r$ = deviation angle

$(d\delta^\circ/di)r$ = deviation angle variation with incidence at the reference incidence angle, read from graph

$$= 0.01$$

$$(i - i_r) = -1.56^\circ - 0.63^\circ = -2.19^\circ$$

$$\delta^\circ = 4.77^\circ$$

The total pressure loss coefficient may be calculated in terms of the air inlet and outlet angles, the wake momentum thickness, and the wake form factor. The equation is

$$\bar{\omega}_1 = 2 \left(\frac{\theta^*}{c} \right) \left(\frac{\sigma}{\cos \alpha_2} \right) \left(\frac{\cos \alpha_1}{\cos \alpha_2} \right)^2 \left(\frac{2 H_2}{3 H_2 - 1} \right) \left(1 - \left(\frac{\theta^*}{c} \right) \left(\frac{\sigma H_2}{\cos \alpha_2} \right) \right)^{-3} = \frac{P_{02} - P_{01}}{\frac{1}{2} \rho_1 V_1^2} \quad (43)$$

where

α_1 = air inlet angle = 31°

α_2 = air outlet angle $\approx 1^\circ$ in the "Suction on, Turb off" flow

σ = solidity = 1.5

H_2 = wake form factor = displacement thickness / momentum thickness

$$= 1.1$$

θ^*/c = wake momentum thickness / chord; may be calculated as a function of the diffusion factor

The diffusion factor, D , is calculated by

$$D = \left(1 - \frac{V_2}{V_1} \right) + \frac{\Delta V_\theta}{2 \sigma V_1} \quad (44)$$

where

$$V_1 \approx 500 \text{ ft/sec}$$

$$V_2 \approx 425 \text{ ft/sec}$$

$$\Delta V_\theta = V_1 \sin(31) = 257.5 \text{ ft/sec}$$

$$D = 0.3217$$

$$\theta^*/c \approx 0.009 \quad \text{from a graph}$$

$$\overline{\omega}_1 = 0.01986$$

Appendix B. Hotwire Calibration

Hot wire anemometry is a method of measuring fluid velocity based on the rate of energy transfer from a heated element immersed in a flow. Heat transfer can occur by conduction, convection, and radiation, but in this application radiation is negligible, and conduction through the element supports is minimal. The general convection equation is $\dot{q} = hA (T_s - T_\infty)$. Assuming that the fluid temperature is known, the rate of energy entering the element and the temperature of the element can be related to velocity, which is embedded in the convection heat transfer coefficient, h .

For some metals, the rate of change of electrical resistance with change of temperature is constant, at least in the range of temperatures useful for hot wire anemometry. The temperature of these metals can be easily determined by measuring resistance. Metals can be heated by passing an electrical current through them, and the energy transferred to the metal is computed as the I^2R loss of the current. The availability of metal temperature and energy transfer rate make these metals useful as sensors for hot wire anemometry. Tungsten, platinum, and iridium are metals commonly used as sensors. The sensor usually takes the form of a wire (about 0.0005 in. diameter) or thin film overlaying a quartz rod (about 0.001 in. diameter), held at each end by support posts. The former is called a hot-wire sensor and the latter is called a hotfilm sensor. In this study a TSI model 1240-10 x-hotfilm was used and is illustrated in Figures 9 and 35.

Hot wire anemometers usually have a sensor placed across one arm of a Wheatstone bridge, and they can be operated in two modes. In the constant current mode, a constant voltage is applied across the bridge. Fluctuations of velocity over the heated sensor changes its temperature and resistance, which in turn affects the balance of the Wheatstone bridge. The bridge output is measured as the sensor signal. In the constant temperature mode, output from the bridge is applied to an amplifier which feeds back to the bridge input. As before, fluctuations in velocity

change the sensor temperature and resistance, unbalancing the bridge. The bridge output then causes the amplifier to adjust the bridge input voltage, either heating or cooling the sensor until the bridge is balanced. The input voltage that balances the bridge is measured as the sensor signal. In this study, a constant temperature anemometer (CTA) was used.

The Wheatstone bridge is set up with a fixed resistance and the sensor on one side, and an equal fixed resistance and a control resistor on the other side. Setting the control resistor equal to the resistance of the sensor balances the bridge. With a CTA, the control resistance is set slightly higher than the sensor resistance. The resulting imbalance causes the bridge input voltage to increase, heating the sensor until the increase in its resistance balances the bridge. The control resistance is used to set the sensor operating temperature in this way.

The development of a calibration law begins by equating the convection heat transfer rate equal with the rate of electrical energy loss, I^2R :

$$I_s^2 R_s = \left(\frac{V_s}{R_s} \right)^2 R_s = h_f A (T_s - T_f) \quad (45)$$

The subscript "s" refers to sensor values, and "f" refers to the fluid values. Equation (45) uses sensor voltage, but bridge voltage is the quantity measured. These voltages can be related by the current in the side of the bridge with the sensor:

$$I = \frac{V_s}{R_s} = \frac{V_{\text{bridge}}}{(R_{\text{upper arm}} + R_{\text{lower arm}})} \quad (46)$$

The bridge upper arm has a fixed resistance, R_u . The bridge lower arm resistance includes the sensor resistance, R_s , the internal resistance of the probe on which the sensor is mounted, R_p , the probe support resistance, R_{ps} , and the resistance of the cable between the probe and the bridge, R_c . The relationship between bridge voltage, V_b , and sensor voltage is then written

$$R_{\text{lower arm}} = R_s + R_{\mu} + R_{\mu} + R_c \quad (47)$$

$$\frac{V_s}{R_s} = \frac{V_b}{(R_s + R_s + R_{\mu} + R_{\mu} + R_c)} \quad (48)$$

In a constant temperature anemometer, the sensor temperature is held constant, effectively holding its resistance constant as well. In addition, the other resistances in equation (48) are also constant, so the ratio of bridge to sensor voltage in a CTA may be assumed constant. Inserting equation (48) into equation (45) yields

$$\left(\frac{V_b}{R_s + R_s + R_{\mu} + R_{\mu} + R_c} \right)^2 R_s = h_f A (T_s - T_f) \quad (49)$$

The sensor surface area, A, is calculated by $A = \pi d_s l_s$. The convection coefficient, h_f , is related to the Nusselt number by $Nu = (h_f d_s)/k_f$, where k_f is the fluid conductive heat transfer coefficient. Equation (49) is solved for the Nusselt number:

$$\left(\frac{V_b}{R_s + R_s + R_{\mu} + R_{\mu} + R_c} \right)^2 R_s = \left(\frac{Nu k_f}{d_s} \right) (\pi d_s l_s) (T_s - T_f) \quad (50)$$

$$Nu = V_b^2 \left(\frac{R_s}{(R_s + R_s + R_{\mu} + R_{\mu} + R_c)^2} \cdot \frac{1}{k_f \pi l_s (T_s - T_f)} \right) \quad (51)$$

To complete the relationship between measured voltage and fluid velocity the Nusselt number can be related to the Reynolds number, $Re = \rho V d_s / \mu$. In general, $Nu \sim Re^5$, but usually several

terms are used to define the relationship. The method of least squares can be used to determine the coefficients of the following equations, the first of which was used in this study:

$$Nu = A + B\sqrt{Re} + CRe \quad (52)$$

$$\sqrt{Re} = A + BNu + CNu^2 \quad (53)$$

The velocity in the Reynolds number is the "effective" velocity across the sensor. It is the vector sum of the perpendicular component of velocity and a fraction of the parallel component of velocity, and is calculated by

$$V_{eff} = V\sqrt{\sin^2 \alpha + k^2 \cos^2 \alpha} \quad (54)$$

where V is the fluid velocity, α is the angle between the sensor axis and the fluid velocity vector, and k is a constant, which may be termed the "cooling ratio". The term k^2 is a ratio which is used because flow parallel to the sensor does not convect away as much energy as does flow perpendicular to the sensor. It is related to the length to diameter ratio of the sensor, and the value of k is usually 0.2 or less. The term is squared to indicate that it is always positive. In this study the value of k for each sensor was determined by an angle calibration that is described later.

The values of k , ρ , and μ , from the Nusselt and Reynolds numbers, are dependant on temperature, so a reference temperature, T_r , must be defined to evaluate them. In the case of convective heat transfer, the surface temperature, T_s , is different from the flow static temperature, T , and a gradient of temperature exists in the fluid near the surface. The average of the surface and fluid temperatures is a rough approximation of the reference temperature. Eckert (12:304) proposed that the reference temperature is best represented by

$$T_r = \frac{1}{2}(T_s + T) + 0.22(T_{AW} - T) \quad (55)$$

$$T_{AW} = T + r_c(T_0 - T) \quad (56)$$

$$T_r = \frac{1}{2}(T_s + T) + 0.22r_c(T_0 - T) \quad (57)$$

where T_0 is the flow total temperature, T_{AW} is the adiabatic wall temperature, and r_c is the recovery factor. T_{AW} is the temperature of an unheated surface in a flow, and its value is between the flow static and total temperatures. It can be obtained by measuring the resistance of the unheated sensor in a flow of air. However, T_{AW} is not available while a sensor is in use (it is heated while in use), so an estimate of the recovery factor must be used to calculate T_r . The recovery factor may be obtained by measuring T_{AW} (with an unheated sensor), T , and T_0 of a flow. Its value should be relatively constant, and may be used to calculate the reference temperature in similar flows.

Unfortunately, r_c could not be obtained with much precision. In the measurement of T_{AW} , changes in sensor resistance were too small for the instrumentation to read accurately (on the order of thousandths of an ohm). Values for r_c between 0.8 and 0.9 with uncertainty of ± 0.03 were observed, and they were somewhat dependent on velocity. In theory, the recovery factor is the square root of the Prandtl number in laminar flows (13:335). Flow over the sensor is laminar ($Re_{sensor} < 400$), and $Pr_{air} = 0.71$, so the value 0.84 was used for recovery factor in this study.

With the reference temperature determined, k_f , ρ , and μ may be evaluated. The value of k_f is

$$k_f = k_0 \left(\frac{T_r}{T_0} \right)^{0.8} \quad (58)$$

where k_0 and T_0 are reference points; $k_0 = 0.242 \text{ J/(m s K)}$ at $T_0 = 273.15 \text{ K}$ (13:269). Density is determined by the state equation, $\rho = P/(R \cdot T_r)$, where P is the static pressure of the flow. Viscosity, like conductivity, is related to a reference point, and is calculated by

$$\mu = \mu_0 \left(\frac{T_r}{T_0} \right)^{\frac{3}{2}} \left(\frac{T_0 + S_1}{T_r + S_1} \right) \quad (59)$$

where $S_1 = 110 \text{ K}$ for air, and $\mu_0 = 1.7456 \cdot 10^{-5} \text{ kg/(m s)}$ at $T_0 = 273.15 \text{ K}$ (13:328).

One additional factor is applied to the calibration to accommodate the effects of fluid temperature variation. Based on the work of Collis and Williams, as described by Bradshaw (14:115), the Nusselt number is multiplied by a temperature loading factor, $(T_r/T)^b$, resulting in a calibration equation of the form

$$Nu \left(\frac{T_r}{T} \right)^b = A + B \sqrt{Re} + C Re \quad (60)$$

The temperature loading factor exponent, b , is given the value -0.17 by Collis and Williams. In this study it was determined by the velocity calibration, which included several fluid temperatures.

Calibration of a sensor is accomplished in four steps. First, the change of sensor resistance with temperature must be obtained. This is an optional step because the information is generally provided by the manufacturer. Secondly, the value of recovery factor must be determined. This is also an optional step because the value recovery factor is defined in the literature. Third, the value of the cooling ratio, k , used in the calculation of effective velocity, must be obtained by an angle calibration. Fourth, values of the coefficients A , B , C , and b must be determined by a velocity calibration that includes variations in the fluid temperature, T .

The angle calibration, adapted from Galassi (15), required a set of velocity data and a set of angle data. The velocity data consists of sensor voltages at several velocities. The angle data consists of sensor voltages at one velocity but with the sensor positioned at different angles with respect to the flow. Both data sets were taken at one fluid temperature and the temperature loading factor exponent, b , was set to zero, because the value of k has no dependence on the fluid temperature. The coefficients A , B , and C were calculated from the velocity data for several values of k , and these coefficients were used to compute the sum squared error for the angle data. Sum squared error is defined as

$$SSE = \sum_{i=1}^n \left(Nu_i \left(\frac{T_{r_i}}{T_i} \right)^b - (A + B \sqrt{Re_i} + C Re_i) \right)^2 \quad (61)$$

The value of k that produced the lowest sum squared error for the angle data was selected. In this study $k_1^2 = 0.076$ and $k_2^2 = 0.0625$.

The velocity calibration required velocity data that included a range of fluid temperatures. With k established, the coefficients A , B , and C were calculated for several values of b . The value of b that produced the lowest sum squared error was selected. In this study $b_1 = -0.143$ and $b_2 = -0.117$. The data must include a range of fluid temperatures for this method to find a reasonable value for b . Otherwise, minimizing SSE may result in a large, negative value of b (about -10 or less), a result which simply forces the Nu term to go to zero.

Given the coefficients A , B , C , and b , the sensor voltages, and the fluid temperature, the effective velocity of the fluid across the sensor can be calculated. Given two effective velocities from an x -sensor and the constants k , the fluid velocity and direction can be calculated. The reduction of sensor voltages to fluid velocity and direction is developed in Appendix C.

Appendix C. Hotwire Data Reduction

An x-sensor produces two voltages that can be reduced to the velocity and angle of the flow through the sensor. The voltages are first converted to effective velocities (across the sensors) by the calibration. The effective velocities are related to the flow velocity and direction by

$$V_{1_e} = V \sqrt{\sin^2 \alpha_1 + k_1^2 \cos^2 \alpha_1} \quad (62)$$

$$V_{2_e} = V \sqrt{\sin^2 \alpha_2 + k_2^2 \cos^2 \alpha_2} \quad (63)$$

The angles α_1 and α_2 , the bisector angle b , and the angle of the flow with respect to the bisector, β , are shown in Figure 35.

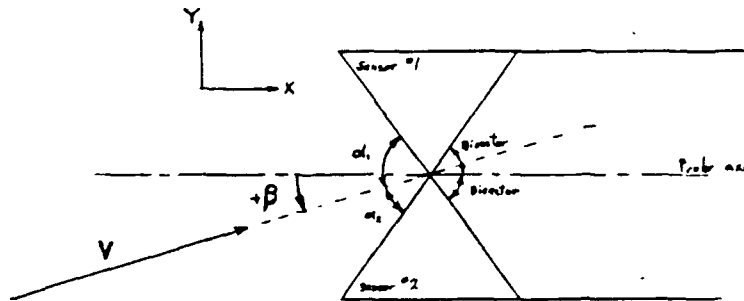


Figure 35. X-wire sensor geometry

The angle β is calculated by $\beta = \alpha_1 - b = b - \alpha_2$. The angles α_1 and α_2 are related by $\alpha_1 + \alpha_2 = 2b$, so equations (62) and (63) contain two unknowns, V and α_1 or α_2 . Combining equations (62) and (63) to eliminating V leaves

$$\frac{V_{1\varphi}}{\sqrt{\sin^2 \alpha_1 + k_1^2 \cos^2 \alpha_1}} = \frac{V_{2\varphi}}{\sqrt{\sin^2 \alpha_2 + k_2^2 \cos^2 \alpha_2}} \quad (64)$$

$$\sin^2 \alpha_1 + k_1^2 \cos^2 \alpha_2 = \left(\frac{V_{1\varphi}}{V_{2\varphi}} \right)^2 (\sin^2 \alpha_2 + k_2^2 \cos^2 \alpha_2) \quad (65)$$

The equation is reduced to one variable by inserting $\alpha_1 = 2b - \alpha_2$.

$$\sin^2(2b - \alpha_2) + k_1^2 \cos^2(2b - \alpha_2) = \left(\frac{V_{1\varphi}}{V_{2\varphi}} \right)^2 (\sin^2 \alpha_2 + k_2^2 \cos^2 \alpha_2) \quad (66)$$

Equation (66) could be solved numerically, but the use of trigonometric identities and algebra yields an expression for α_2 . In the following development

$$VRS = \left(\frac{V_{1\varphi}}{V_{2\varphi}} \right)^2 \quad (67)$$

$$\sin(2b - \alpha_2) = \sin 2b \cos \alpha_2 - \cos 2b \sin \alpha_2 \quad (68)$$

$$\cos(2b - \alpha_2) = \cos 2b \cos \alpha_2 + \sin 2b \sin \alpha_2 \quad (69)$$

Incorporating these terms,

$$(\sin 2b \cos \alpha_2 - \cos 2b \sin \alpha_2)^2 + k_1^2 (\cos 2b \cos \alpha_2 + \sin 2b \sin \alpha_2)^2 = VRS (\sin^2 \alpha_2 + k_2^2 \cos^2 \alpha_2) \quad (70)$$

$$\begin{aligned}
& (\sin^2 2b \cos^2 \alpha_2 - 2 \sin 2b \cos \alpha_2 \cos 2b \sin \alpha_2 + \cos^2 2b \sin^2 \alpha_2) \\
& + k_1^2 (\cos^2 2b \cos^2 \alpha_2 + 2 \cos 2b \cos \alpha_2 \sin 2b \sin \alpha_2 + \sin^2 2b \sin^2 \alpha_2) \quad (71) \\
& = VRS (\sin^2 \alpha_2 + k_2^2 \cos^2 \alpha_2)
\end{aligned}$$

Now divide by $\cos^2 \alpha_2$:

$$\begin{aligned}
& (\sin^2 2b - 2 \sin 2b \cos 2b \tan \alpha_2 + \cos^2 2b \tan^2 \alpha_2) + k_1^2 (\cos^2 2b + 2 \cos 2b \sin 2b \tan \alpha_2 + \sin^2 2b \tan^2 \alpha_2) \quad (72) \\
& = VRS (\tan^2 \alpha_2 + k_2^2)
\end{aligned}$$

Insert the identity $2 \sin(2b) \cos(2b) = \sin(4b)$ and collect the $\tan(\alpha_2)$ terms:

$$\begin{aligned}
& (\sin^2 2b - \sin 4b \tan \alpha_2 + \cos^2 2b \tan^2 \alpha_2) + k_1^2 (\cos^2 2b + \sin 4b \tan \alpha_2 + \sin^2 2b \tan^2 \alpha_2) \quad (73) \\
& = VRS (\tan^2 \alpha_2 + k_2^2)
\end{aligned}$$

$$\begin{aligned}
& \tan^2 \alpha_2 (\cos^2 2b + k_1^2 \sin^2 2b) + \tan \alpha_2 (-\sin 4b + k_1^2 \sin 4b) + (\sin^2 2b + k_1^2 \cos^2 2b) \quad (74) \\
& = \tan^2 \alpha_2 VRS + k_2^2 VRS
\end{aligned}$$

$$\tan^2 \alpha_2 (\cos^2 2b + k_1^2 \sin^2 2b - VRS) + \tan \alpha_2 (\sin 4b (k_1^2 - 1)) + (\sin^2 2b + k_1^2 \cos^2 2b - k_2^2 VRS) = 0 \quad (75)$$

The quadratic equation is used to solve equation (75) for $\tan \alpha_2$, and values for α_1 , β , and V are then calculated directly. The solution requires that $-b < \beta < b$. The cooling ratios, k_1 and k_2 , reduce the range of validity by a small amount (depending on their values). With the k values in this study the adjusted range is about $-0.9b < \beta < 0.9b$. This reduction of sensor voltages to fluid velocity and direction was derived with the assistance of Capt. Dino Ishikura (16).

Appendix D. Turbulence Calculations

An x-sensor may be used to measure the level of turbulence intensity in two dimensions. The x and y directions shown in Figure 35 are used in the following development. Turbulence intensity is calculated by

$$Tu_x = \frac{\bar{v}_x}{V} \quad (76)$$

$$Tu_y = \frac{\bar{v}_y}{V} \quad (77)$$

$$Tu = \frac{\sqrt{(\bar{v}_x^2 + \bar{v}_y^2)/2}}{V} \quad (78)$$

where \bar{v}_x and \bar{v}_y are the root mean squares of the x and y components of the velocity fluctuations. The root mean square (rms) of the velocity fluctuations is calculated by

$$v_{RMS} = \bar{v} = \sqrt{\frac{\sum_{i=0}^N (V_i - \bar{V})^2}{N-1}} \quad (79)$$

Turbulence intensity can be calculated from hotwire voltages by two methods. The first is to compute a set of velocities from the voltages, and then calculate the rms velocity fluctuations directly. This method is computationally intensive because of the number of calculations involved in reducing sensor voltages to velocities. In the second method, the relationship between voltage and velocity given by the calibration equation is used to develop a relationship between voltage fluctuations and velocity fluctuations. The resulting velocity fluctuations are oriented in the direction of the effective velocity across the sensor, so additional calculations are required to transform them to the x and y directions. Calculation of turbulence intensity is much faster with

this second method. The development of its equations is presented below in three parts: the generation of rms velocity fluctuations from sensor voltage fluctuations, the scaling and transformation of velocity fluctuations, and the calculation of turbulence in the x and y directions.

Calculation of Velocity Fluctuation Root Mean Squares

The calculation begins with equation (60), the calibration equation derived in Appendix B. Using equation (51) and the following substitutions, the calibration equation can be written in terms of voltage and velocity:

$$Nu \left(\frac{T_r}{T} \right)^b = A + B \sqrt{Re} + C Re \quad (80)$$

$$Nu = V_b^2 \left(\frac{R_s}{(R_a + R_s + R_{ps} + R_{pw} + R_c)^2} \cdot \frac{1}{k_f \pi l_s (T_s - T_p)} \right) \quad (81)$$

$$Re = \rho V_{eff} d / \mu \quad (82)$$

$$A = A / \left(\frac{R_s}{(R_a + R_s + R_{ps} + R_{pw} + R_c)^2} \cdot \frac{(T_r/T)^b}{k_f \pi l_s (T_s - T_p)} \right) \quad (83)$$

$$B = B \sqrt{\rho d / \mu} / \left(\frac{R_s}{(R_a + R_s + R_{ps} + R_{pw} + R_c)^2} \cdot \frac{(T_r/T)^b}{k_f \pi l_s (T_s - T_p)} \right) \quad (84)$$

$$C = C (\rho d / \mu) / \left(\frac{R_s}{(R_a + R_s + R_{ps} + R_{pw} + R_c)^2} \cdot \frac{(T_r/T)^b}{k_f \pi l_s (T_s - T_p)} \right) \quad (85)$$

$$V_b^2 = A + B \sqrt{V_{eff}} + C V_{eff} \quad (86)$$

Differentiating equation (86),

$$2 V_b dV_b = \left(\frac{\dot{B}}{2\sqrt{V_{eff}}} + \dot{C} \right) dV_{eff} \quad (87)$$

$$dV_{eff} = \left(\frac{2 V_b 2\sqrt{V_{eff}}}{\dot{B} + 2\sqrt{V_{eff}} \dot{C}} \right) dV_b \quad (88)$$

$$dV_{eff} = \left(\frac{4 V_b V_{eff}}{\dot{B} \sqrt{V_{eff}} + 2 \dot{C} V_{eff}} \right) dV_b \quad (89)$$

The constant B and C may be substituted back into the equation

$$dV_{eff} = \left(\frac{4 V_b \left(\frac{R_s}{(R_s + R_s + R_{ps} + R_{ps} + R_c)^2} \cdot \frac{(T_f/T)^b}{k_f \pi l_s (T_s - T_f)} \right) V_{eff}}{B \sqrt{(\rho d / \mu)} \sqrt{V_{eff}} + 2 C (\rho d / \mu) V_{eff}} \right) dV_b \quad (90)$$

$$dV_{eff} = \left(\frac{4 \left(\frac{Nu (T_f/T)^b}{V_b} \right) V_{eff}}{B \sqrt{Re} + 2 C Re} \right) dV_b \quad (91)$$

The Nusselt and Reynolds numbers are reintroduced because they are used in the calibration (in Appendix B) and are readily available in the computer code.

For a given set of voltages (100 points sampled at 10 kHz were acquired for each data point in this study), the mean voltages were used to compute each term in equation (91) except for the differentials, which were represented by differences from the mean. Equation (91) is squared and summed over the sample set to produce rms values, as defined by equation (79):

$$(V_{eff_i} - \bar{V}_{eff})^2 = \left(\frac{4 \left(\frac{Nu (T_f/T)^b}{V_b} \right) V_{eff}}{B \sqrt{Re} + 2 C Re} \right)^2 (V_{b_i} - \bar{V}_b)^2 \quad (92)$$

$$V_{eff_{rms}}^2 = \left(\frac{4 \left(\frac{Nu (T_f/T)^b}{V_b} \right) V_{eff}}{B \sqrt{Re} + 2 C Re} \right)^2 V_{b_{rms}}^2 \quad (93)$$

Scaling and Transformation of Coordinates

The components of velocity perpendicular to the sensors are used to calculate the velocities in the x and y directions (axial and normal to the probe). They are calculated by scaling the effective velocity at each sensor.

$$V_p = V \sin \alpha \quad (94)$$

$$V_p = V_{eff} \left(\frac{\sin \alpha}{\sqrt{\sin^2 \alpha + k^2 \cos^2 \alpha}} \right) \quad (95)$$

Next, the velocities in the x and y directions must be calculated from the velocity components perpendicular to the sensors. The calculation differs from a standard coordinate transformation, because the sensors may not be perpendicular to each other. The x direction is identified by the bisector of the angle between the sensors, and is assumed to be in line with the axis of the probe. The sensors are then fixed at $\pm b$ (the bisector angle) with respect to the x direction. With reference to Figure 35, the transformation is

$$V_{1_p} = V_x \sin b + V_y \cos b \quad (96)$$

$$V_{2_p} = V_x \sin b - V_y \cos b \quad (97)$$

$$V_x = \frac{V_{1p} + V_{2p}}{2 \sin b} \quad (98)$$

$$V_y = \frac{V_{1p} - V_{2p}}{2 \cos b} \quad (99)$$

Calculation of Turbulence

Equations (98) and (99) give x and y velocities in terms of the velocities perpendicular to each of the sensors. Differentiating them yields

$$dV_x = \left(\frac{1}{2 \sin b} \right) (dV_{1p} + dV_{2p}) \quad (100)$$

$$dV_y = \left(\frac{1}{2 \cos b} \right) (dV_{1p} - dV_{2p}) \quad (101)$$

Squaring and summing them over a sample of points produces functions for the rms values of velocity fluctuations in the x and y directions:

$$v_{x_{rms}}^2 = \bar{v}_x^2 = \left(\frac{1}{2 \sin b} \right)^2 \left(v_{1p_{rms}}^2 + 2 \left(\frac{\sum_{i=1}^n dV_{1p} dV_{2p}}{n-1} \right) + v_{2p_{rms}}^2 \right) \quad (102)$$

$$v_{y_{rms}}^2 = \bar{v}_y^2 = \left(\frac{1}{2 \cos b} \right)^2 \left(v_{1p_{rms}}^2 - 2 \left(\frac{\sum_{i=1}^n dV_{1p} dV_{2p}}{n-1} \right) + v_{2p_{rms}}^2 \right) \quad (103)$$

where

$$dV_{1,p} = (V_{1,p})_i - \overline{V}_{1,p} \quad (104)$$

$$dV_{2,p} = (V_{2,p})_i - \overline{V}_{2,p} \quad (105)$$

Given \overline{v}_x and \overline{v}_y , turbulence is calculated by equation (78).

REPORT DOCUMENTATION PAGE			Form Approved GSA GEN. REG. NO. 27	
1. AGENCY USE ONLY (Leave blank)			2. REPORT DATE December 1991	
4. TITLE AND SUBTITLE Experimental Investigation of Trailing Edge Crenulation Effects on Losses in a Compressor Cascade			3. REPORT TYPE AND DATES COVERED Master's Thesis	
6. AUTHOR(S) Steven J. DeCook			5. FUNDING NUMBERS	
7. PERFORMING ORGANIZATION NAME(S) AND ADDRESS(ES) Air Force Institute of Technology, WPAFB OH 45433-6583			8. PERFORMING ORGANIZATION REPORT NUMBER AFIT/GAE/ENY/91D-1	
9. SPONSORING/MONITORING AGENCY NAME(S) AND ADDRESS(ES) Bill Copenhagen WL/POTX Wright-Patterson AFB, OH 45433			10. SPONSORING/MONITORING AGENCY REPORT NUMBER	
11. SUPPLEMENTARY NOTES				
12a. DISTRIBUTION/AVAILABILITY STATEMENT Approved for public release; distribution unlimited			12b. DISTRIBUTION CODE	
13. ABSTRACT (Maximum 200 words) The effects of blade trailing edge crenulations on wake losses in a compressor cascade were investigated at the Air Force Institute of Technology. The cascade used NACA 64-A905 blades with a turning angle of about 30 degrees to model last row stators of an axial flow compressor. Three blade configurations used unmodified blades, blades with large crenulations, and blades with small crenulations. Wake losses and mixing were evaluated in four flow conditions, generated by combinations of increased freestream turbulence and sidewall boundary layer removal. Injection of air perpendicular to the inlet flow increased freestream turbulence from about 0.15% to about 4%. The sidewall boundary layers could be removed by suction through sidewall slots immediately ahead of the cascade. A total pressure rake measured the difference between upstream and downstream total pressure, yielding pressure loss and velocity data, and hot wire anemometry was used downstream from the cascade to measure flow angle, relative turbulence, and velocity. For each test condition, the crenulated blades decreased total pressure loss, the wake velocity deficit, and wake velocity variance by about 10% to 20%, while slightly decreasing turning angle and increasing the turbulence level. The crenulation size had only a small effect on these parameters.				
14. SUBJECT TERMS axial flow compressor blades, cascades, crenulations, trailing edges, airfoil, wake			15. NUMBER OF PAGES 115	
			16. PRICE CODE	
17. SECURITY CLASSIFICATION OF REPORT Unclassified	18. SECURITY CLASSIFICATION OF THIS PAGE Unclassified	19. SECURITY CLASSIFICATION OF ABSTRACT Unclassified	20. LIMITATION OF ABSTRACT UL	

GENERAL INSTRUCTIONS FOR COMPLETING SF 298

The Report Documentation Page (RDP) is used in announcing and cataloging reports. It is important that this information be consistent with the rest of the report, particularly the cover and title page. Instructions for filling in each block of the form follow. It is important to **stay within the lines to meet optical scanning requirements.**

Block 1. Agency Use Only (Leave Blank)

Block 2. Report Date. Full publication date including day, month, and year, if available (e.g. 1 Jan 88). Must cite at least the year.

Block 3. Type of Report and Dates Covered. State whether report is interim, final, etc. If applicable, enter inclusive report dates (e.g. 10 Jun 87 - 30 Jun 88).

Block 4. Title and Subtitle. A title is taken from the part of the report that provides the most meaningful and complete information. When a report is prepared in more than one volume, repeat the primary title, add volume number, and include subtitle for the specific volume. On classified documents enter the title classification in parentheses.

Block 5. Funding Numbers. To include contract and grant numbers; may include program element number(s), project number(s), task number(s), and work unit number(s). Use the following labels:

C - Contract	PR - Project
G - Grant	TA - Task
PE - Program Element	WU - Work Unit Accession No.

Block 6. Author(s). Name(s) of person(s) responsible for writing the report, performing the research, or credited with the content of the report. If editor or compiler, this should follow the name(s).

Block 7. Performing Organization Name(s) and Address(es). Self-explanatory.

Block 8. Performing Organization Report Number. Enter the unique alphanumeric report number(s) assigned by the organization performing the report.

Block 9. Sponsoring/Monitoring Agency Names(s) and Address(es). Self-explanatory.

Block 10. Sponsoring/Monitoring Agency Report Number. (If known)

Block 11. Supplementary Notes. Enter information not included elsewhere such as: Prepared in cooperation with...; Trans. of ..., To be published in When a report is revised, include a statement whether the new report supersedes or supplements the older report.

Block 12a. Distribution/Availability Statement.

Denote public availability or limitation. Cite any availability to the public. Enter additional limitations or special markings in all capitals (e.g. NOFORN, REL, ITAR)

DOD - See DoDD 5230.24, "Distribution Statements on Technical Documents."

DOE - See authorities

NASA - See Handbook NHB 2200.2.

NTIS - Leave blank.

Block 12b. Distribution Code.

DOD - DOD - Leave blank

DOE - DOE - Enter DOE distribution categories from the Standard Distribution for Unclassified Scientific and Technical Reports

NASA - NASA - Leave blank

NTIS - NTIS - Leave blank.

Block 13. Abstract. Include a brief (Maximum 200 words) factual summary of the most significant information contained in the report.

Block 14. Subject Terms. Keywords or phrases identifying major subjects in the report.

Block 15. Number of Pages. Enter the total number of pages.

Block 16. Price Code. Enter appropriate price code (NTIS only).

Blocks 17. - 19. Security Classifications. Self-explanatory. Enter U.S. Security Classification in accordance with U.S. Security Regulations (i.e., UNCLASSIFIED). If form contains classified information, stamp classification on the top and bottom of the page.

Block 20. Limitation of Abstract. This block must be completed to assign a limitation to the abstract. Enter either UL (unlimited) or SAR (same as report). An entry in this block is necessary if the abstract is to be limited. If blank, the abstract is assumed to be unlimited.